A_NDY: Measurement of the Analyzing Power for Large Rapidity Drell-Yan Production

S. Abrahamyan[1], E. C. Aschenauer[2], H. Avakian[3], A. Bazilevsky[2], L. C. Bland[2], E. J. Brash[4,3], H. J. Crawford[5], A. Derevshchikov[6], K. Drees[2], J. Engelage[5], K.O.Eyser[2], C. Folz[2], K. Gnanvo[7], G. Igo[8], E. G. Judd[5], Xuan Li[9], M. X. Liu[10], N. K. Liyanage[7], Y. Makdisi[2], N. Minaev[6], D. Morozov[6], L. V. Nogach[6], A. Ogawa[2], C. F. Perdrisat[11], C. W. Perkins[5,12], P. Pile[2], M. Planinic[13], V. Punjabi[14], G. Schnell[15], A. Shahinyan[1], G. Simatovic[13], T. G. Throwe[2], C.Van Hulse[15], and A. Vossen[16]

[1]Yerevan Physics Institute, Armenia
[2]Brookhaven National Laboratory
[3]Thomas Jefferson National Accelerator Facility
[4]Christopher Newport University
[5]University of California, Berkeley/Space Sciences Laboratory
[6]Institute for High Energy Physics, Protvino
[7]University of Virgina
[8]University of California, Los Angeles
[9]Shandong University, China
[10]Los Alamos National Laboratory
[11]College of William and Mary
[12]Stony Brook University
[13]University of Zagreb, Croatia
[14]Norfolk State University
[15]University of the Basque Country and IKERBASQUE, Spain

[16]Indiana University

January 4, 2012

Contents

List of Figures

1 Introduction

We propose to measure the transverse single spin asymmetry A_N for Drell-Yan virtual photon production at RHIC. If the current understanding of the space/time structure of color flow in hard scattering processes is correct [1], this asymmetry should have opposite sign to that measured in semi-inclusive deep inelastic scattering (SIDIS) at HERMES [3] and at COMPASS [4]. Color flow in these processes is depicted in Fig. 1. The DY virtual photons will be observed through their decay to e^+e^- pairs which are detected in the apparatus we propose to assemble as shown in Fig. 2. Demonstration that dileptons can be extracted from prolific backgrounds from $p+p$ collisions using event selections described in the original proposal [2], is given by analysis of data from RHIC run 11 in Fig. 3, and is further described below. The total cost for the project is \$1.52M, with \$1.19M in FY12 and \$0.32M in FY13. Details of the theory, simulations, apparatus, and management are presented below.

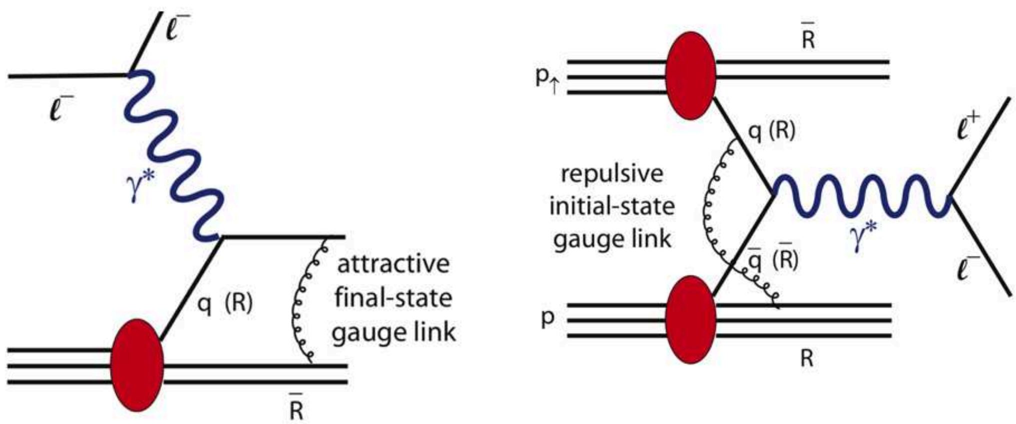

Figure 1: These diagrams show the gauge link in semi-inclusive deep inelastic scattering and Drell-Yan production. Note that color is not annihilated in the SIDIS process, with the interacting quark continuing to feel the attraction of its anti-color partners. In the DY process the forward-going proton sends an anti-color parton to interact with a color-parton from the other proton, with the result that the "spectator" has the same color as the interacting parton from the "target" proton. In both processes, the anisotropy results from orbital motion inside the proton.

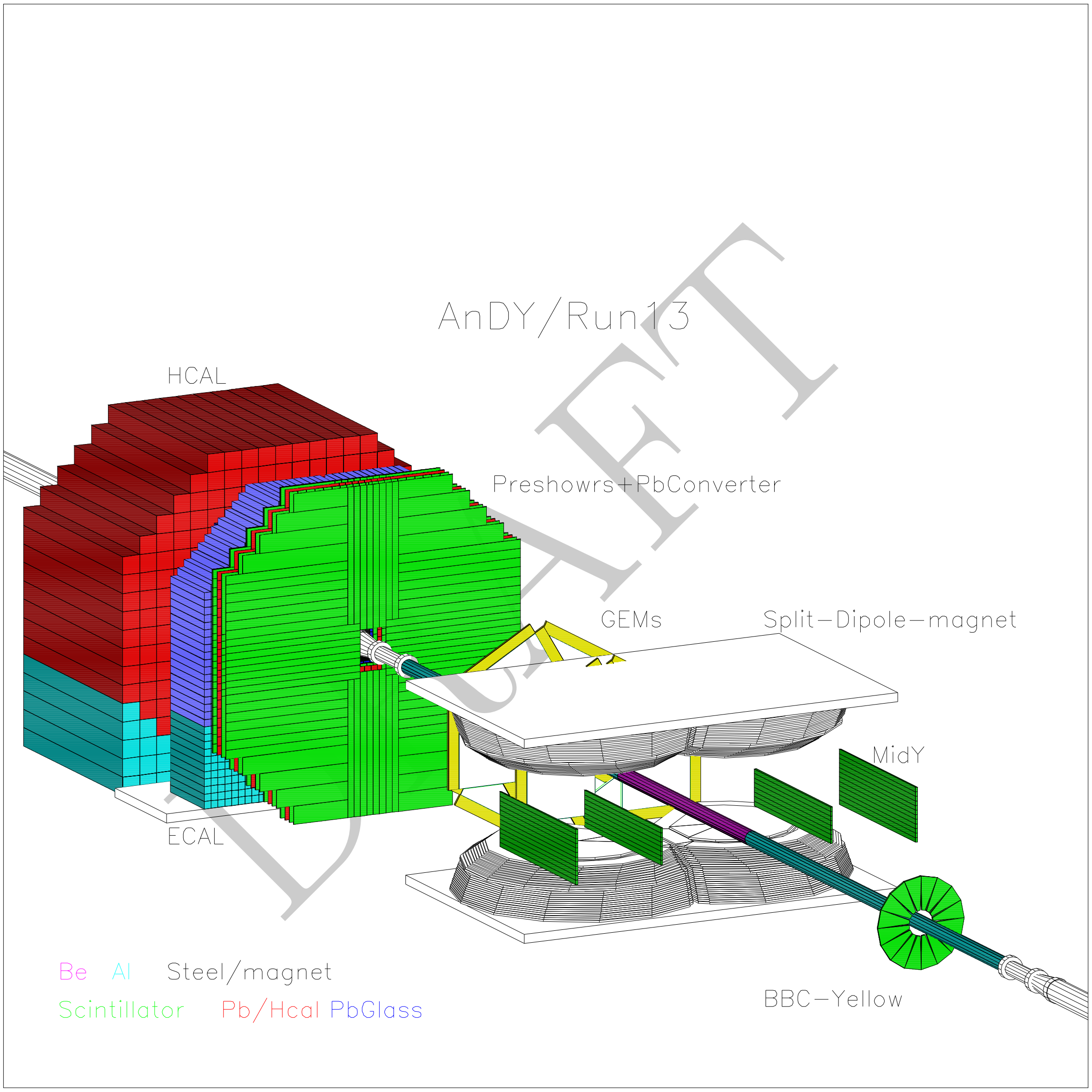

Figure 2: GEANT rendering of the apparatus we propose for observing Drell-Yan production

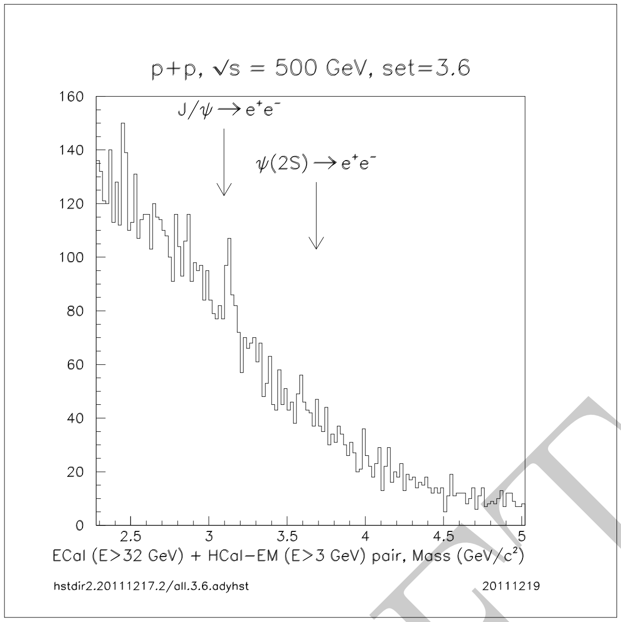

Figure 3: Cluster pair mass distribution including the BBC requirement that clusters have a MIP-like response. Final calibrations are based on individual detector mass distributions. A clear peak from $J/\psi \rightarrow e^+e^-$ is observed, despite the limited statistics provided by the run-11 ECal triggered data set.

A$_N$DY is an experiment to measure the analyzing power for forward di-electrons produced by the Drell-Yan (DY) process in polarized proton collisions at $\sqrt{s}$=500 GeV. The experiment is staged at interaction point 2 (IP2) at the Relativistic Heavy Ion Collider (RHIC) at Brookhaven National Laboratory. The physics motivation for A$_N$DY was described and reviewed by the BNL program advisory committee (PAC) in June 2011, and the complete proposal to the PAC is attached as Appendix 1 to this funding proposal. The committee has endorsed running for A$_N$DY based on tests we performed in run11 (ref html of report), which we summarize here. Measuring DY e^+e^- pairs at RHIC requires multiple simultaneous photon and hadron rejection methods to kill background, the detritus from the spectator, driving the implementation presented here. This document proposes the implementation of A$_N$DY for RHIC runs 13 and run 14, the maximum duration of the project.

Transverse single spin asymmetries (SSA) are expected to be vanishingly small in collinear leading-twist perturbative QCD due to the chiral symmetry nature of the theory. However, large spin effects are measured for $p^{\uparrow} + p \rightarrow \pi^0 + X$ at RHIC energies [5, 6] and at lower $\sqrt{s}$, essentially concurrent with these measurements at RHIC, sizable SSA were also observed for semi-inclusive deep inelastic electron scattering (SIDIS) from transversely polarized proton targets [3]. The large spin effects are not compatible with the collinear leading-twist description of particle production that successfully describes the spin-averaged cross sections and two-particle correlations. Theory can accommodate such large spin effects, however, by going beyond the collinear picture to include transverse momentum dependent (TMD) distribution and fragmentation functions.

Spin-dependent TMD distribution functions describe orbital motion of partons in the proton. A requirement for spin-dependent TMD distribution functions to produce large transverse SSA is that the particle production amplitude has both real and imaginary parts [8]. Without this phase, naive time reversal invariance results in the expectation that spin-dependent TMD distribution functions vanish. The phase arises naturally from gauge invariance and is effectively given by the QCD analog of Coulomb wave functions as the current quark propagates through the color field produced by the spectator partons. For SIDIS, there is an attractive color force between the current quark and the spectators because the virtual photon interacts with an initially color neutral proton. There is a robust theoretical prediction [1] that the attractive color final-state interactions in SIDIS will become a repulsive color initial-state interaction in Drell Yan production, thereby resulting in a change in sign for transverse single spin asymmetries in DY versus those in SIDIS. The goal of A$_N$DY is to measure the analyzing power for DY production to test this prediction. Achieving this goal would satisfy a DOE performance milestone (HP13).

There are two basic requirements that must be met for A$_N$DY to succeed: (1) there must be adequate yield for the DY production of virtual photons to provide sufficient statistical precision to test the sign change prediction; and (2) the kinematics for DY production must overlap the kinematics for SIDIS to allow clean comparison. The first requirement is primarily met by luminosity and beam polarization performance for spin-polarized colliding beam operations at RHIC. Detector acceptance is then dictated by the RHIC performance to ensure adequate precision for the measurement. The second requirement sets the range in p_T and x_F where A$_N$DY must operate. A$_N$DY will initially concentrate on $M_{\gamma^*} > 4$ GeV/c^2, where M_{γ^*} is the DY virtual photon invariant mass, rather than the much lower masses needed to match the Q^2 scale of the SIDIS results, because predicted backgrounds at lower mass appear to preclude measurement of a spin observable. We will, however, push our analysis below the 4 GeV limit to reconstruct the J/Psi and other charm states, as shown in Fig.3, and to determine the limits of our background rejection..

The importance of the second requirement has been clarified by recent theoretical work [9] that seeks a global analysis of measured analyzing power for pion production at RHIC and transverse SSA for SIDIS. A global analysis of the experimental results is particularly challenging to theory since pion production has no proven factorization theorems that use TMD distribution functions extracted from SIDIS, unlike the case for DY production. Instead, the pion production results are analyzed via a twist-3 formalism for which factorization has been proven [10]. The analysis extracts quark-gluon correlators that can be intercompared to moments of the Sivers function extracted from SIDIS. The RHIC pion production results show large analyzing powers for $x_F > 0.3$ [6]. The SIDIS results span $0.05 < x_B < 0.3$ [3]. Consequently, the data have essentially no kinematic overlap. Accounting for the different gauge links that enter, the conclusion from theory [9] is that there is a sign mismatch between the SIDIS results and the RHIC pion production results. This mismatch can be accommodated if the Sivers function has a node near $x_F \simeq 0.3$ [11, 12]. A_NDY must overlap the kinematics of SIDIS experiments to avoid the complications near this node and to provide a robust test of the theoretical prediction for a sign change. This overlap sets requirements on A_NDY acceptance and on signal:background ratio.

Simultaneous with our measurement of A_N for DY, we propose to measure the neutral pion analyzing power at x_F values that overlap our proposed DY measurements and also overlap our prior measurements at large x_F [6]. This will eliminate any ambiguity in the sign of the spin asymmetries measured.

The primary detector in A_NDY is a high-resolution electromagnetic calorimeter (ECal) built from 1596 lead-glass cells that view particles produced in the forward direction by colliding beams. The discrimination of electrons and positrons from the background of photons and hadrons is accomplished by associating the ECal response with the response of a preshower detector (PS) immediately in front of ECal and with the response of a hadron calorimeter (HCal) immediately behind ECal. A tracking system (TRK) consists of three stations of Gas electron multipliers (GEM) to provide high resolution tracking. These make the association between PS detectors and ECal clusters robust, and help discriminate photons from charged particles. We propose one data set be taken with an existing split-dipole magnet. Tracking through the magnet identifies charge sign and further discriminates showers in ECal produced by electrons and positrons from showers produced by photons produced in the collision.

The preshower detector consists of two overlapping planes of 76 scintillation counters each followed by a lead converter and a third plane of scintillators. The preshower plays a crucial role in identifying the particle responsible for creating a cluster in ECal by providing a crude measurement of the longitudinal energy deposition profile. Photons will give no response in the first two scintillator planes and a partial shower response in the third plane. Charged hadrons will most probably give the response of a minimum-ionizing particle (MIP) in all scintillator planes. Electrons and positrons will give a MIP-like response in the first two scintillator planes and a partial shower response in the scintillator that follows the converter.

The hadronic calorimeter consists of 296 lead-scintillating-fiber cells originally developed for AGS experiment E864. The primary purpose of the HCal is also for longitudinal energy profiling. Hadrons that partially shower in ECal will be rejected by matching the clustered ECal response to the clustered HCal response.

The tracking system consists of 24 GEM modules, each 40cm x 50 cm incorporating 2250 strips, with ADC values for each strip allowing interplolation to provide $\leq 100\mu$ position resolution. Stations 1 and 2 (TRK1 and TRK2) each consist of 6 modules in overlapping hexagons, providing efficiency $\geq 98\%$ for charged particles. Station 3 (TRK3) consists of a single plane of 12 modules. The electrons and hadrons produce single MIP response, while the e^+e^- pair from a photon conversion in the beam pipe can be distinguished by its 2-MIP signal in each module of TRK1.

This document is divided into the following sections. Section 2 describes the run-11 tests for A_NDY with a focus on the primary goals of establishing the impact of collisions at IP2 on STAR and PHENIX and of the operation and calibration of the HCal. Section 3 and section 4 describe the proposed configuration of ECal and HCal. Section 5 describes the proposed configuration of the preshower. Section 6 describes a detector to measure vertex location. Section 7 briefly describes the proposed forward pion detector implementation that closes as many theoretical loopholes as possible. Section 8 describes A_NDY tracking detectors. Section 9 describes the split-dipole magnet proposed. Section 10 describes the triggers we will use and the data acquisition system. Section 11 describes the simulations we use to design and understand our experiment. Section 12 describes our computer needs. Section 13 is a summary of budget and our resource loaded timeline. Section

14 is our management plan and Section 15 addresses safety.

2 Run-11 Summary

A preliminary test for A$_N$DY was implemented at IP2 for RHIC run 11 (Fig. 4). The primary goals of RHIC run 11 as described in the 2010 Letter of Intent to the PAC [2] were to

- establish the impact of initiating collisions at IP2 on operations at IP6 and IP8; and
- to demonstrate that the hadron calorimeter modules (HCal) could be calibrated.

This section summarizes the work done prior to RHIC run 11 in which we tested portions of the major detector components we propose to assemble for A$_N$DY, and summarizes the status to date of understanding collision data from the run-11 A$_N$DY configuration.

2.1 Preparations for RHIC run 11

The IP2 area is the former location of the magnetic spectrometers built and operated by the BRAHMS collaboration [17]. In August, 2010 the remnants of the BRAHMS experiment were still in place at IP2. Led by Charles Folz, different teams from the Collider-Accelerator (C-A) department made a major cleanup of the IP2 area in a 3-month period, effectively removing all remnants of the apparatus built by BRAHMS. In addition, these C-A teams installed AC power distribution and cable tray for the run-11 A$_N$DY electronics; designed and implemented supports for reconfigured HCal modules formerly at IP10 and used by the PHOBOS collaboration; designed and implemented support stands for small ECal modules populated by 120 lead-glass detectors borrowed from BigCal [14] at Jefferson laboratory; designed and implemented support stands for two beam-beam counter arrays borrowed from the University of Maryland [15]; aided in the construction of preshower detector supports; installed a beryllium beam pipe with specially designed support stands; surveyed the apparatus that got built at IP2 for the run-11 A$_N$DY configuration; and installed fiber-optic communication lines for clock distribution from RHIC-standard V-124 modules to the A$_N$DY electronics,

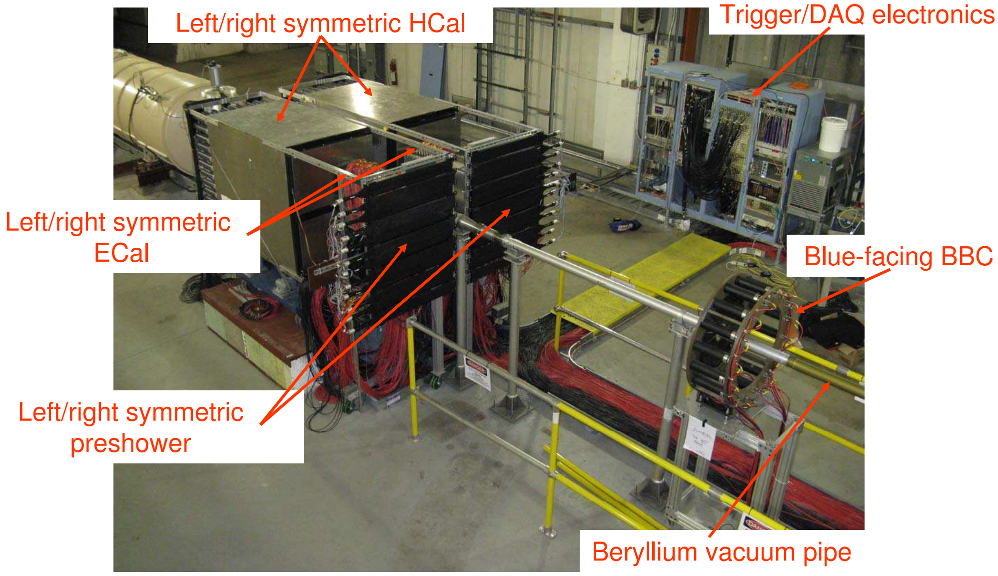

Figure 4: Picture of the A$_N$DY apparatus for RHIC run 11. Not shown in the picture are the Yellow-beam facing beam-beam counter array and the zero-degree calorimeters. The hadron calorimeter (HCal) modules were built from detectors constructed for AGS-E864 [13]. The electromagnetic calorimeters (ECal) were built from lead glass borrowed from Jefferson Laboratory [14]. The beam-beam counters (BBC) were built for PHOBOS [15]. The preshower scintillators were built for the run-11 A$_N$DY implementation.

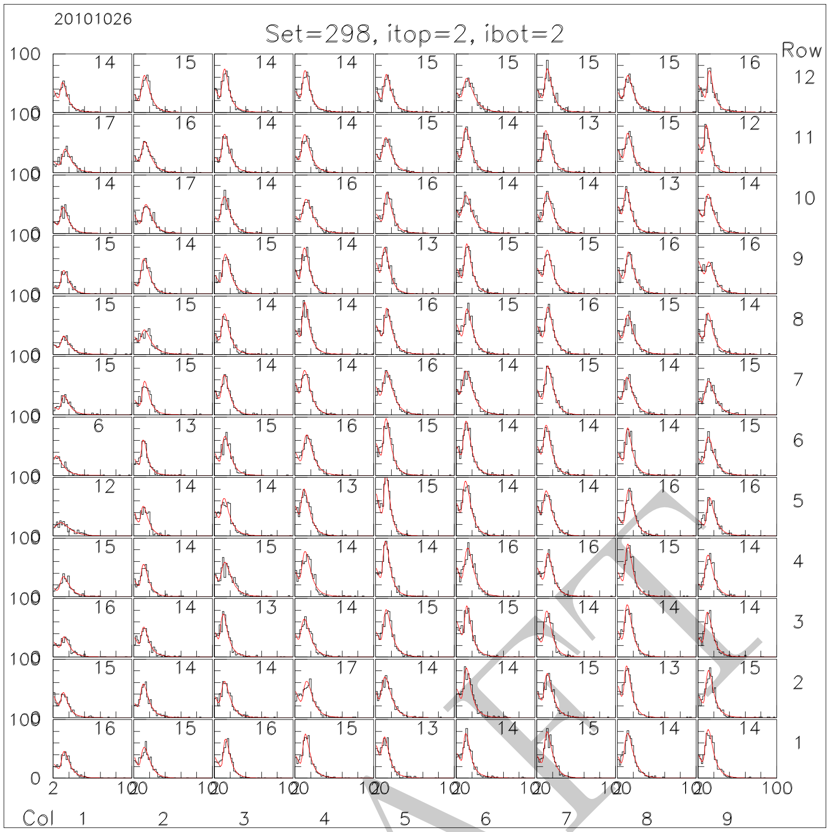

Figure 5: Individual detector ADC spectra from the beam-left HCal module for cosmic-ray triggers taken prior to run 11. The data show clear peaks associated with a minimum-ionizing particle (cosmic-ray muon) passing through the stack. The distributions are fit by an exponential background summed with a Landau distribution. The centroid of the Landau distribution for each detector is shown on the plot.

a fiber-optic network used for data acquisition and to provide monitoring as feedback to the RHIC main control room. The resulting run-11 A_NDY apparatus is shown pictorially in Fig. 4.

Members of A_NDY were busy from August, 2010 through January, 2011 building and testing detector apparatus and the trigger/data acquisition electronics [18]. The HCal modules that had been used at PHOBOS were moved to IP2 in August and the cosmic-ray muon calibration of these detectors began immediately. A key that enabled this effort was that the STAR trigger system [18] had all the ingredients of a configurable trigger and data acquisition system. That step had been taken in 2009 for cosmic-ray muon based calibration of a 5-row $\times$ 10-column hadron calorimeter module originally built for PHOBOS from the AGS-E864 detectors, as reported by a graduate student at a Division of Nuclear Physics meeting [19]. That system was transported to IP2 in August, 2010 and was initially made operational for 64-channel readout and later extended for testing and ultimately for the run-11 A_NDY trigger/DAQ system (see 2.2).

We also had one 32-channel low-voltage distribution board to power the Cockcroft-Walton bases for the first tests of the HCal, of the type fabricated to power all CW bases used for the run-11 A_NDY configuration. The same methods used for relative gain monitoring and testing of lead-glass calorimeters worked very well for HCal (see Section 3.5 for more detail of the fiber-optic distribution of light-emitting diode (LED) flashes). Consequently, a gain curve for each HCal photomultiplier tube was measured. This data proved essential during the RHIC run when first indications of the HCal energy scale for showers from particles produced in collisions became available, and facilitated a gain change of HCal during the run.

The portable trigger/DAQ system was expanded to 128 channels of readout and the rapid fabrication of the low-voltage distribution boards resulted in full 9-column $\times$ 12-row HCal module tests with cosmic-ray muons, with concurrent LED-based gain monitoring, starting in early October. The trigger used for this work ensured complete integration of the cosmic-ray muon signals through the clocked trigger/DAQ system by an effective time-to-amplitude converter on plastic scintillator paddles put above (top) and below (bottom) the HCal stack. Three paddles were put on top of the stack and three below the HCal stack to localize the cosmic-ray muon trajectory along the length of the HCal detector, to confirm that the attenuation length of the scintillating fibers in the detectors was observed. The "beam-left" HCal module calibration was completed in late October with final data as shown in Fig. 5. Similar cosmic-ray calibrations were completed for the "beam-right" HCal module just before the modules were moved onto their support stands for operation in run 11. The portable DAQ system was subsequently dismantled and was reconfigured for the run-11 A_NDY trigger/DAQ system.

A loan agreement between the Yerevan Physics Institute (YerPI) and BNL was signed by BNL, Jefferson Laboratory and YerPI in October, 2010. This agreement enabled the loan of 120 40mm$\times$40mm$\times$40cm lead-glass bars, FEU-84 photomultiplier tubes and resistive bases from a calorimeter that had been constructed, commissioned and used for experiments at JLab (BigCal [14], further discussed in Section 3. The primary purpose of this loan was to assess whether the lead glass was sufficiently annealed of color-trapping centers after use of BigCal in a high-luminosity experiment at JLab. After transport to BNL, transparency measurements and visual inspection showed the glass to be clear, except for ∼8 bars. These bars were annealed at BNL by ultraviolet lamps. A secondary application of these borrowed lead-glass detectors was to make a pair of small-scale electromagnetic calorimeter (ECal) modules by adapting enclosures that were in storage at BNL. The adaptation required an interface between the SHV feedthroughs on the exterior paneling of the enclosures and Hypertronix connectors on the resistive bases built by YerPI and used in BigCal. Optical coupling of FEU-84 to the lead glass was accomplished by using threaded rods screwed into vanadium blocks glued to the glass. The FEU-84 was pushed against the lead glass using a thin pusher plate stamped with the pin pattern of the phototube. Optical grease between the phototube entrance window and the lead glass was used for the coupling. This is the same method we propose for these detectors for the full-scale A_NDY ECal, as described in Section 30. Neutral pion reconstruction from the run-11 A_NDY ECal modules showed expected mass resolution, as discussed below.

Finally, we built a prototype of the preshower counters envisioned for the final A_NDY configuration. BC-408 scintillator was ordered from St. Gobain and delivered by early December, 2010. The scintillator was carefully inspected and then wrapped in aluminized mylar reflectors. Forty Hamamatsu H5010 photomultiplier + resistive base assemblies were borrowed from AGS-E896 and were used for the 2.5-cm wide × 90-cm long × 1.0-cm thick long scintillator strips. A total of 24 Photonis XP2972 photomultipliers with Cockcroft-Walton bases were borrowed from AGS-E864 [13] and used for 10.5-cm wide × 90-cm long × 1.0-cm thick scintillator strips. The wide scintillators were individually wrapped in black tedlar to make the detectors light tight. The construction of the preshower scintillator plane built from 2.5-cm wide strips is described in some detail below, since we propose a similar construction method for the A_NDY preshower proposed for RHIC run 13.

The construction method for the preshower plane built from 2.5-cm wide scintillator strips was as follows. Each strip was individually wrapped with aluminized mylar. After wrapping, the strips were glued to a roughened aluminized mylar substrate on each side to form a uniform and rigid 50-cm wide × 90-cm long plane. This gluing method minimizes cracks between adjacent scintillator strips. The method had been developed for scintillator-stip shower maximum detectors used in electromagnetic calorimeters. Fiber-

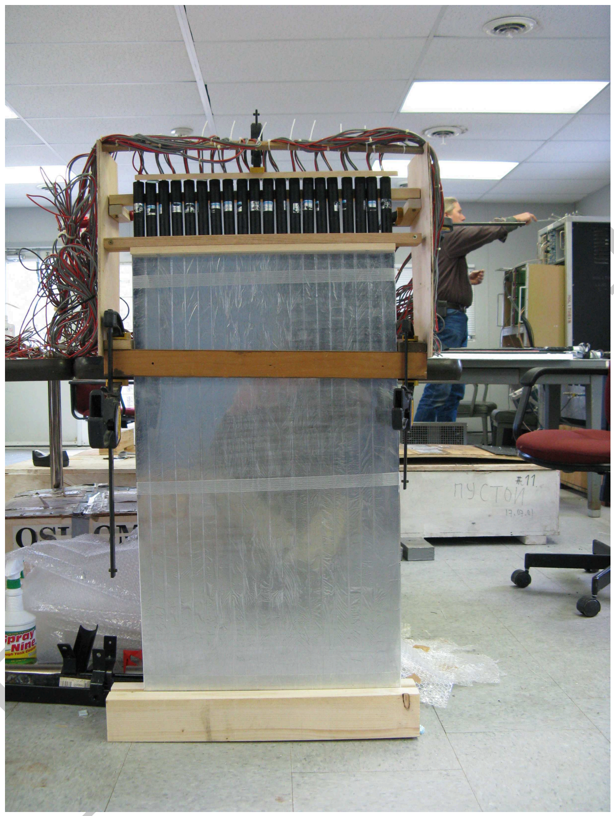

Figure 6: Stand used for gluing Hamamatsu H5010 phototube assemblies to 2.5-cm wide × 90-cm long × 1.0-cm thick BC-408 strips. There are 20 such strips glued to make a rigid plane.

glass reinforced tape was wrapped around the glued assembly to reinforce the glue joints. The planned construction for the preshower will eliminate a tape wrap in the center of the resulting plane.

The array of H5010 phototube assemblies were then glued at one end of the scintillator strips. The difficult part of this assembly was to compensate for the torque on the H5010 from the integral cabling for high-voltage to the resistive divider and co-axial signal cables for the anode output. A jig was constructed for the gluing of the phototube assemblies to the strips. The jig enforced the centering of the phototubes on each strip and enabled downward pressure on the assemblies while the glue was setting. A photograph of one plane in its gluing jig is in Fig. 6. After this step, the entire plane was enclosed in black tedlar to make the detector plane light tight. This step will be avoided for the run-13 preshower construction due to the potential for non-uniformities of material at the preshower. Instead, the unwrapped plane will be mounted within the ECal enclosure, as discussed below. The entire process of preparing the preshower scintillators took four weeks, although the actual time involved was mostly associated with preparing and implementing a gluing, followed by ∼12 hours to allow a complete hardening of the glue.

A final essential component to the run-11 preparations was a GEANT model of the apparatus (Fig. 7). This had initially been prepared to study A_NDY configurations prior to the 2010 letter of intent [2]. That initial model was then extended to include the small ECal modules, the beam-beam counters and the preshower arrays ultimately built and implemented prior to RHIC run 11.

2.2 Description of run-11 trigger/DAQ system

The A_NDY trigger and data acquisition system is based on hardware fabricated for the first generation of the STAR experiment and is described in more detail in Sec.10. A_NDY uses the RHIC standard Zero Degree Calorimeters (ZDC) located at the exit of each final bending magnet (DX magnet) in the beam lines $\sim 8m$ on either side of the IP in setup and triggering. Each ZDC consists of 3 PMTs viewing fibers from a sphagetti calorimeter and a Shower Max Detector (ZDC-SMD) consisting of 8 vertical and 8 horizontal scintillators. The ZDC-SMD is used in local polarimetry, and discriminator outputs from each strip are recorded in a 10 MHz histogramming scaler board for each RHIC crossing. Minimum bias triggers used in run 11 were based on the ZDC and BBC detectors, with high-tower, cluster, and pair triggers

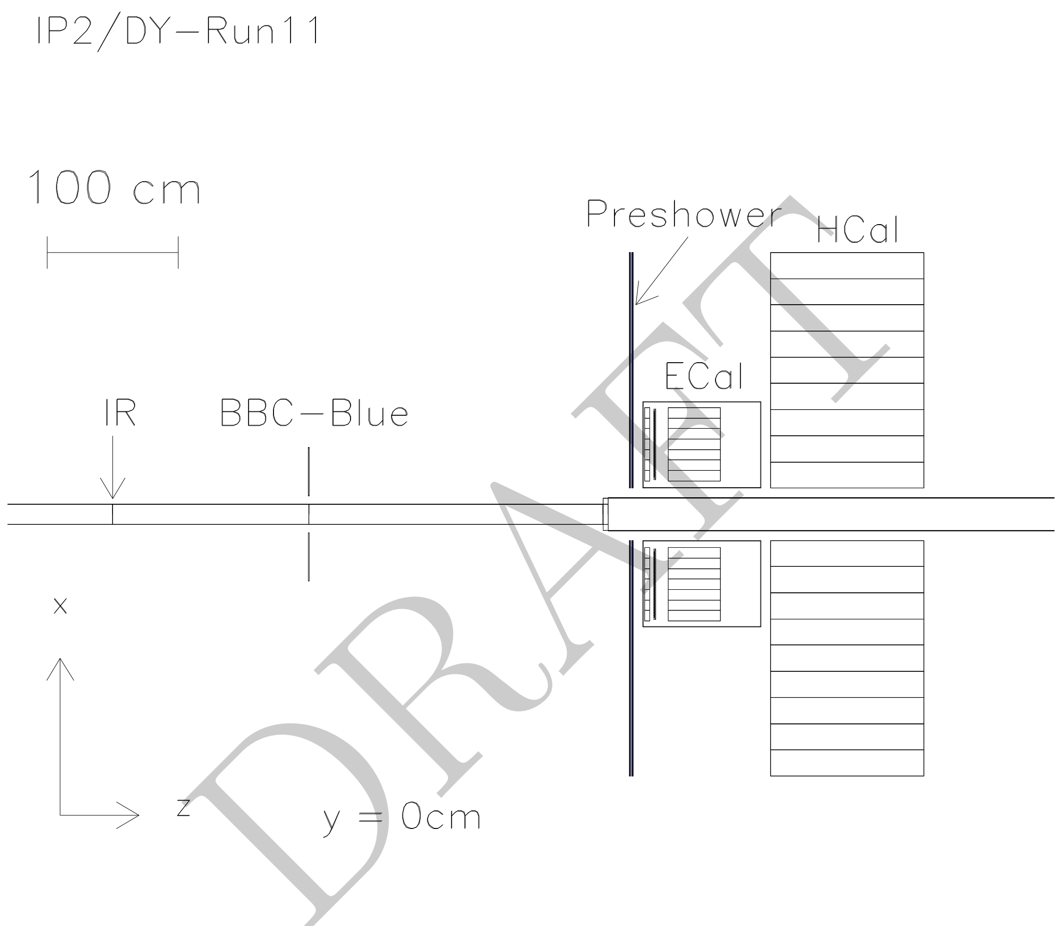

Figure 7: GEANT model of run-11 A_NDY configuration. The Blue beam travels in the positive z direction and the Yellow beam travels in the negative z direction, with the collision diamond centered at z=0, as indicated by IR on the drawing. Simulation samples consist of events generated by PYTHIA 6.222 that are then tracked for each particle through the GEANT model.

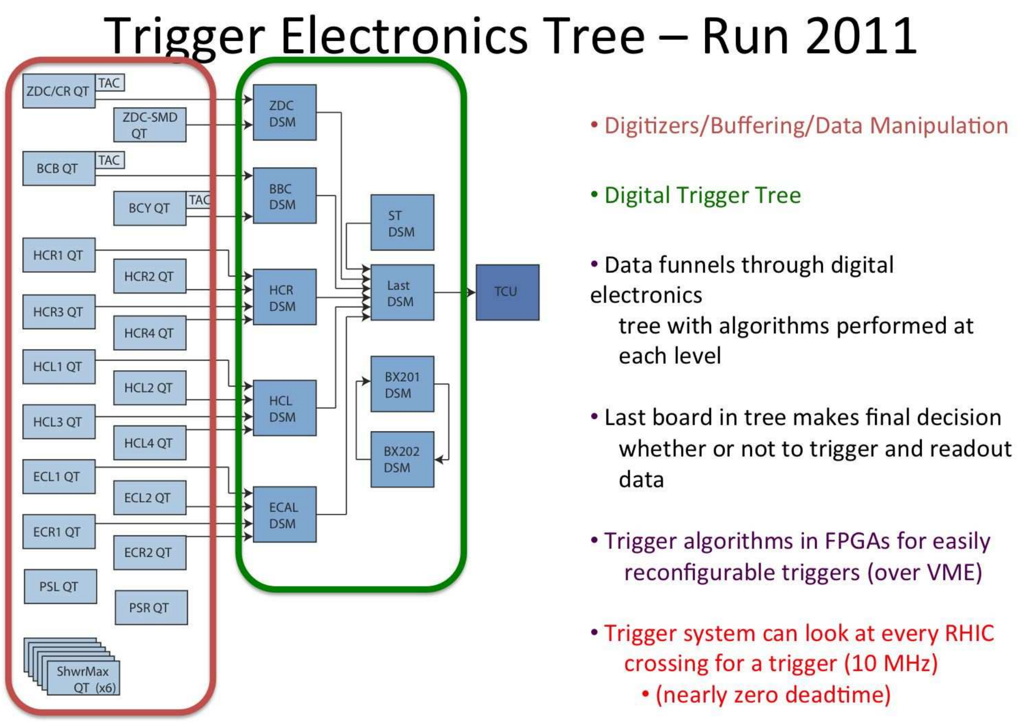

Figure 8: DSM trigger logic tree for run 11.

adding information from ECal and HCal as shown in the logic tree of Fig.8.

2.3 Impact of IP2 collisions and projections for Lint for runs 12,13

Testing the impact of IP2 collisions on operations at IP6 and IP8 was a primary objective of RHIC run 11 [2]. The issue that needed to be addressed is the impact of tune shifts and tune spreads of one beam induced by the other beam (so-called beam-beam tune shifts). In previous years for $\sqrt{s}$=200 GeV polarized proton collisions, bunches from the Blue ring that interacted at more points around the ring with bunches from the Yellow ring showed increased rate of ion loss and emittance growth through the store, leading to lower luminosity. RHIC requires bunch intensities approaching 2×10^{11} protons/bunch to achieve the luminosities required for the RHIC spin program. The betatron oscillation tunes are limited by all the orbit instability resonant conditions. Preserving polarization adds different limitations on the tunes. This additional complexity is not present in other colliders, making RHIC a unique challenge in the world for accelerator physicists. The effects of beam-beam tune shifts increase linearly with the number of ions per bunch, are inversely proportional to the emittance of the bunch and depend on the number of bunch crossing points in the collider. These tune shift effects, however, do not depend on the ion optics, *i.e.* the β^* used at collision points.

The limitations from beam-beam tunes shifts and spreads were fully recognized before RHIC run 11. Documentation of the impact of a third collision point was readily available from prior years when beams collided at three points around RHIC. This documentation was a topic of multiple discussions between A_NDY proponents and accelerator physicists in the Collider-Accelerator department. These earlier experiences were not sufficient to be certain of the impact of collisions at IP2 on operations at IP6 and IP8 since many different working points in the betatron oscillation tune space have been used to satisfy the additional constraint of preserving polarization while also avoiding orbit instability resonances. The question posed by the 2010 program advisory committee was to quantitatively establish the impact of IP2 collisions. The expectation from the prior RHIC runs was that there would be some loss of luminosity at IP6 and IP8. The fundamental question was the magnitude of this loss, since small losses (*e.g.*, <20%) could accommodate running A_NDY in parallel with the W program at STAR and PHENIX while large losses (*e.g.*, >20%) would be best accomodated by doing the experiments serially rather than in parallel. The plan for polarized proton operations at $\sqrt{s}$ = 500 GeV in run 11 was to operate RHIC with fractional betatron oscillation tunes near the 2/3 orbit instability resonance so as to improve the polarization of the beams over what had been achieved in RHIC run 9.

A further complicating factor for IP2 operation was that the DX magnets at IP2 had in the past exhibited less robust quench training behavior than nominally identical magnets at the five other interaction regions in RHIC. This prompted the plan to start polarized proton operations at $\sqrt{s}$=500 GeV in run 11 with a $\sim$2 mr bunch crossing angle at IP2. With typical bunch lengths from prior years of RHIC operation, the non-zero crossing angle corresponded to a factor of three less luminosity relative to head-on collisions. Through the run, training quenches of the DX magnets either side of IP2 were done during times when issues precluded RHIC operation. There was a brief period of $\sim$1.6 mr bunch-crossing angle operation at IP2 and then head-on collisions at IP2 after the last training quench on 18 March. The scripted start of IP2 collisions did require changes when the crossing angle changed, since the required currents in corrector magnets to initiate collisions in one step depended on the crossing angle.

RHIC stores have the sequence of bunch injection, acceleration ramp, spin-rotator ramps to precess the spins to make longitudinal polarization for collisions at IP6 and IP8, cogging of the two beams thereby having bunches from each ring cross the interaction regions at the same time and then removal of transverse separations of the two beams at IP6 and IP8 to initiate collisions there. Early in each RHIC store, 10-mm transverse separation bumps of the two beams remained in place at IP2. Late in the store, separation bumps at IP2 were removed to initiate collisions. The beam-beam tune shifts and spreads initiated by the IP2 bump removal would lead to increased ion loss and potentially impact the luminosity at IP6,IP8. The time dependence of the beam intensity, the loss rate of ions in each ring, and luminosities at IP6 and IP8 were available in real time through the run through an interface to RHIC data in the A_NDY counting house, and at STAR and PHENIX. The real time strip charts were recorded for most bump removals in the A_NDY electronic log. An example of an IP2 bump removal record from the A_NDY e-log entry 1845 for RHIC fill 15436 is shown in Fig. 9

Some fills had quantitatively different behaviors than shown in Fig. 9, although the qualitative features of these plots were present in most fills. The qualitatively common features are:

- there was an initial increase in ion loss rate when collisions were initiated at IP2 that subsequently decayed with increasing time.
- The ion loss rate was almost always bigger in the Yellow ring than in the Blue ring, independent of whether there were more ions in Yellow or more ions in Blue at the time IP2 collisions began.
- Some fills had larger peak loss rates than others. This appeared to be associated with the betatron oscillation tunes for the store and whether there were tune adjustments before or after the IP2 bump removal. Typically worse loss rates, or longer times for the loss rate to damp away, were associated with tune adjustments after the bump removal.

The plan to quantitatively assess the impact of IP2 collisions on IP6 and IP8 was to systematically increase the average bunch intensity when

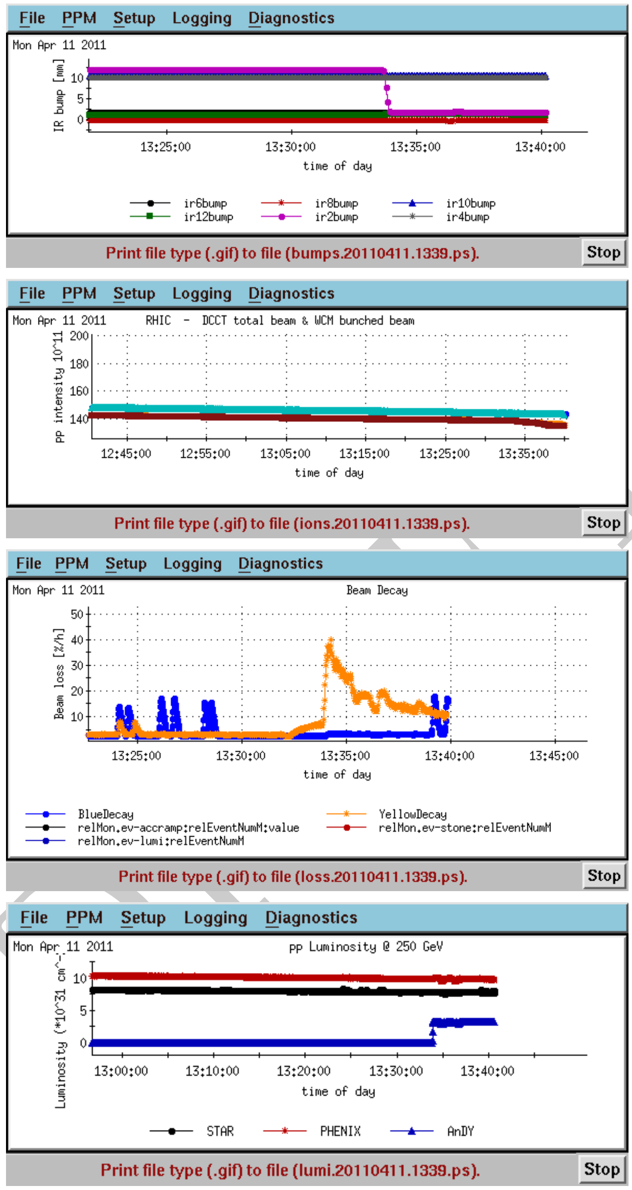

Figure 9: Time dependence strip charts available as real-time feedback that document the start of collisions at IP2 for RHIC store 15436. The four plots from top to bottom are: (1) transverse separation bumps at the six interaction regions around RHIC. At 13:34, corresponding to 197 minutes after the declaration of the start of physics for this store, the separation bump at IP2 is removed; (2) number of ions in the Blue and Yellow ring. A small change in slope is observed for the Yellow ring at 13:34 when IP2 collisions are initated; (3) the ion loss rate (D) versus time for the Blue and Yellow rings. The peaks are associated with insertions of the carbon ribbon used for Coulomb-nuclear interference (CNI) polarimemters. There is an increase in D in Yellow when collisions are initiated at IP2 that damps away with increasing time; and (4) the luminosity at IP6, IP8 and IP2 as measured by the rate of coincidences observed in zero degree calorimeters common to all interaction regions. The change in instantaneous luminosity at IP6 and IP8 is not evident for this store.

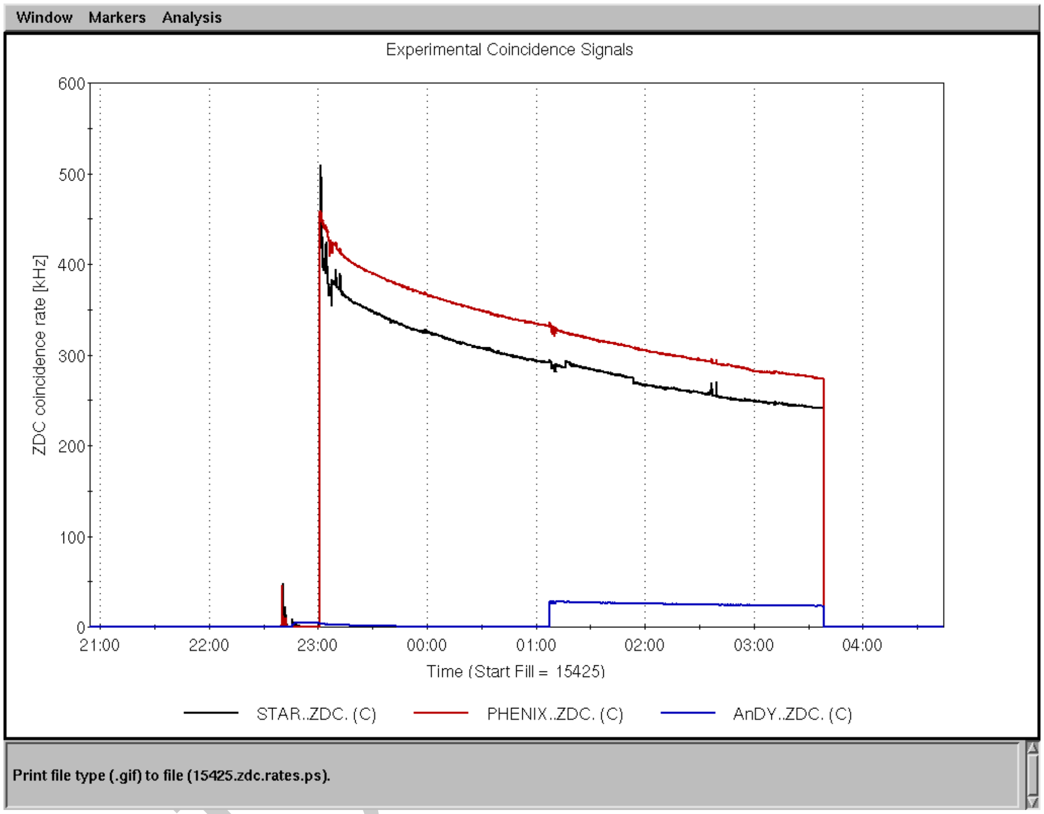

Figure 10: ZDC coincidence rate at STAR, PHENIX and IP2 versus time for RHIC store 15425. IP2 collisions were begun when the bunch intensity had decreased to 1.50×10^{11} ions per bunch. Narrow peaks in the STAR ZDC coincidence rate are associated with backgrounds accompanying CNI polarimeter measurements. The maximum rate of ZDC coincidences at the different interaction points reflects differences in ion optics at the three collision points (β^{*}=3m at IP2. Smaller values are used for IP6 and IP8, resulting in larger luminosity.) and differences in ZDC operating voltages and thresholds. Both effects are corrected for by vernier scans.

the IP2 transverse separation bumps were removed. The starting point was 0.95×10^{11} ions per bunch. The increment in this threshold was 0.05×10^{11} ions per bunch. This increment sometimes was automatically implemented for successive stores and sometimes was not implemented, depending on the real-time feedback. While this study was underway, there was a separate program to increase the number of ions injected into RHIC to increase the luminosity for $\sqrt{s} = 500$ GeV polarized proton collisions. The program to increase the bunch intensity meant that the time when IP2 collisions began got successively later in store, or meant that the store was dumped before IP2 collisions began. When the luminosity increase program reached its plateau, the time when IP2 collisions began became progressively earlier. The last point studied was the start of IP2 collisions at the average of 1.50×10^{11} ions per bunch. The luminosity at STAR, PHENIX and IP2 for RHIC fill 15425 is shown in Fig. 10. Collisions began at IP2 when the intensity had fallen below the 1.50×10^{11} ions per bunch threshold.

The impact of IP2 collisions on operation at IP6 and IP8 was continually watched and discussed with accelerator physicists and members of STAR and PHENIX during the polarized proton run. Discussions were possible by participation of A$_N$DY at each daily RHIC operation meeting focused on status and planning; at each weekly Time meeting, used to report A$_N$DY progress and plans and to hear reports from the accelerator subsystems and the other experiments; at each weekly accelerator/experiment planning meeting; and at special meetings, as needed. Discussions and reports are documented on public web sites. These discussions led to refinements in the general procedure for starting collisions at IP2. For example, one important refinement was to synchronize the transverse separation bump removal at IP2 with scheduled CNI polarimeter measurements, as requested by the PHENIX collaboration since they reduced operating voltages on their muon arm detectors for both activities due to the potential for increased background.

A summary of the integrated luminosity recorded at IP2 is shown in Fig. 11. The vertical axis on this plot is proportional to the number of coincidences from the IP2 beam-beam counters that face the Yellow and Blue beams. Also shown is the integrated luminosity deduced from the number of coincidences from the IP2 ZDC that face the Yellow and Blue beams. The proportionality constant represents an effective cross section. For this plot, the effective cross section for the IP2 BBC is from analysis of a complete PYTHIA/GEANT simulation, discussed in more detail below. The simulation generates non-elastic, non-single diffractive p+p collision events at $\sqrt{s}$

= 500 GeV using PYTHIA 6.222 with default settings. The PYTHIA events are then run through the IP2 GEANT simulation. Energy deposition in the BBC detectors modeled in this simulation is then digitized to simulate the ADC response, accounting for photostatistics and photomultiplier resolution. An online analysis of the vernier scan at IP2 for RHIC store 15457 resulted in the effective cross section of 0.98 mb for ZDC coincidences. This is within 7% of the effective cross section for the ZDC deduced from the simulations. The systematic error estimates associated with the integrated luminosity measurement still must be completed. As discussed below, it is expected that the $\sim$6.5 pb^{-1} of integrated luminosity delivered to IP2 for polarized proton collisions will result in the first measurement of the analyzing power for forward jet production. Unbiased jet triggers and reconstruction is possible with this data obtained with the HCal modules in place at IP2.

With a primary motivation of calibrating the IP2 ZDCs using the prolific 100-GeV neutron flux, there were two stores where full-energy Au ions collided at IP2. This is further discussed in section 3.4. Beam-beam tune shifts and spreads are not a limiting factor for heavy ion operations at RHIC.

A conclusion that had been reached and agreed upon by the experiments and the accelerator physicists was that IP2 collisions could begin at average bunch intensities corresponding to $\sim$3 hours after physics was declared for the store, with minimal impact on operations at IP6 and IP8. This conclusion resulted in accelerator physicists estimating that 10 pb^{-1}/week of integrated luminosity could be delivered to IP2 during $\sqrt{s}$ = 500 GeV polarized proton operation [20]. To achieve this luminosity, IP2 would need to be operated at β^*=1.5m in runs 13,14. Even smaller values may be possible.

2.4 Run-11 A$_N$DY performance

The commissioning of the run-11 A$_N$DY apparatus involved eliminating single-channel issues (mostly associated with bad cables, bad connectors at patch panels, or loose connections), timing adjustments, photomultiplier tube voltage adjustments to optimize gain uniformity, trigger development and checks, and confirmation of expected physics correlations within the data. Some of these items were addressed before collisions began and some required colliding beams to finalize. The strategy employed was to first optimize a minimum-bias trigger, since this provided the most important checks of the performance of HCal and ECal. After optimizing the minimum-bias trigger and recording large data samples, the development of more sophisticated triggers

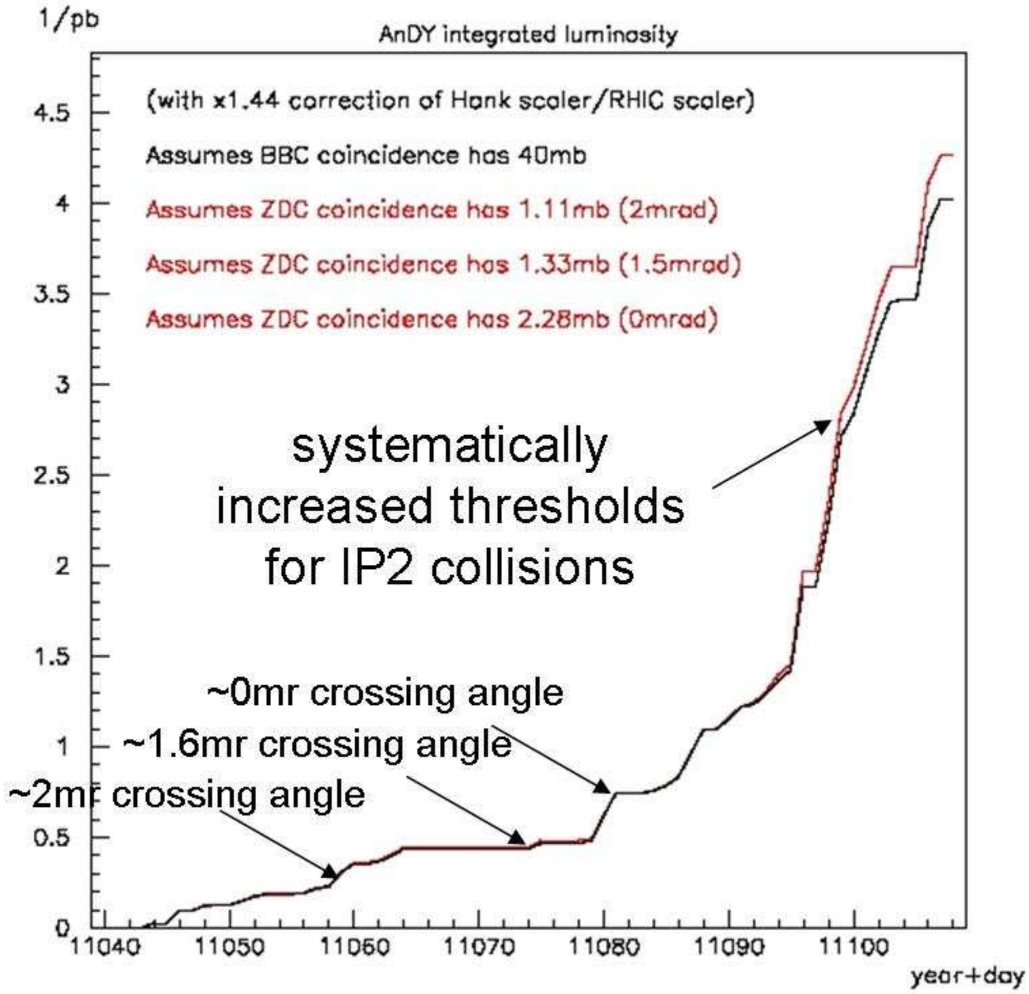

Figure 11: Integrated luminosity at IP2 versus time, as deduced from the number of coincidences from the IP2 beam-beam counters and the zero-degree calorimeters. The effective cross sections used to scale the coincidence count to integrated luminosity are from simulation, as described in the text. The effective cross section from a vernier scan at IP2 during RHIC fill 15457 is 7% smaller than deduced from the simulation, based on online analysis. Systematic errors in the integrated luminosity measurement must still be estimated, but are likely associated with backgrounds in the detectors and RHIC parameters for the store in which the vernier scan was completed.

proceeded.

The minimum bias trigger optimization involved gain adjustments for the BBC detectors, timing adjustments at the QT boards (see Fig.44), optimization of the time-to-amplitude signals for the BBC and ZDC detectors from which the collision vertex z position is determined by time differences, and fixing the parameters for the minimum-bias trigger. The primary focus for more sophisticated triggers was on a jet trigger, corresponding to a threshold on a masked sum of HCal detectors from a single module. Its development required optimizing the timing of pulses of the QT integration gate with respect to the pulses from particles produced by collisions, setting masks to select jets whose thrust axis was centered within a module, and then setting thresholds. Other triggers used frequently through the run were a module-summed ECal trigger that preferentially selects events that have energetic forward neutral pion production, LED monitoring triggers to monitor the gains of ECal and HCal, a zero-degree calorimeter trigger used for verifying that the A_NDY apparatus could measure a known analyzing power, and a zero-bias trigger used to configure the pedestal corrections made on the QT boards to have robust zero suppression of the data.

Fig. 12 shows individual detector ADC distributions for the Blue-facing BBC from minimum-bias triggers. The large peak in each distribution corresponds to a single minimum-ionizing particle passing through the detector. The MIP centroid was used to measure gain curves for each phototube and a single iteration in the high-voltage adjustments was made for gain matching the detectors. MIP peak resolutions are comparable for most detectors. The width is primarily associated with photostatistics and phototube resolution, as established by offline comparison to full PYTHIA/GEANT simulations. Evident for most detectors are peaks corresponding to two MIPs passing through one detector in the same event.

Fig. 13 shows a vertex-z distribution with and without trigger level cuts. The vertex-z position is proportional to the time difference of the earliest hits on the Blue-facing and Yellow-facing BBC annuli. Hit timing is measured by integrating a current produced by a time-to-amplitude converter (TAC), started when a BBC detector crosses a preset threshold and stopped by the RHIC clock, meaning that large TAC values are early hits and small TAC values are late hits. Time difference is computed by the trigger FPGA coding by first identifying the earliest hit detector on a QT board that has both analog inputs and TAC inputs from each detector in the same 70-ns gate (so-called “max-TAC algorithm”). The vertex z position is proportional to

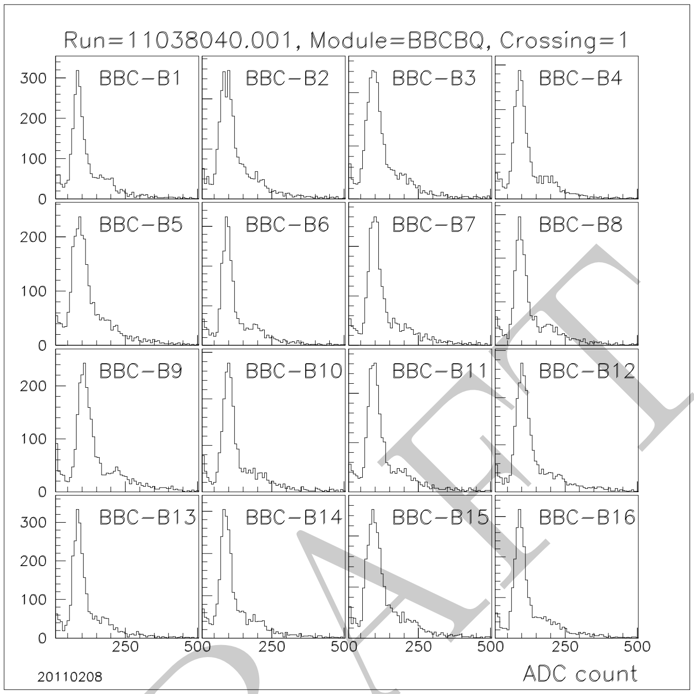

Figure 12: Charge distributions for Blue-beam-facing BBC for minimum-bias events that include a timing cut on the collision z distribution. Detector numbers increase in the clockwise direction around the annulus, when looking towards the interaction point. Gain matching was complete for this run, as were all final timing adjustments. The minimum bias trigger required the summed charge for both the Blue-beam and Yellow-beam facing BBC arrays to exceed 60 ADC counts, and required that the difference between the time-to-amplitude converter channels (see Fig. 13) for the first hits in Blue and Yellow arrays be smaller than ± 400 counts. The large peaks in each detector correspond to a minimum-ionizing particle passing through the detector. Most detectors also show a well defined peak from events where two minimum-ionizing particles pass through that detector.

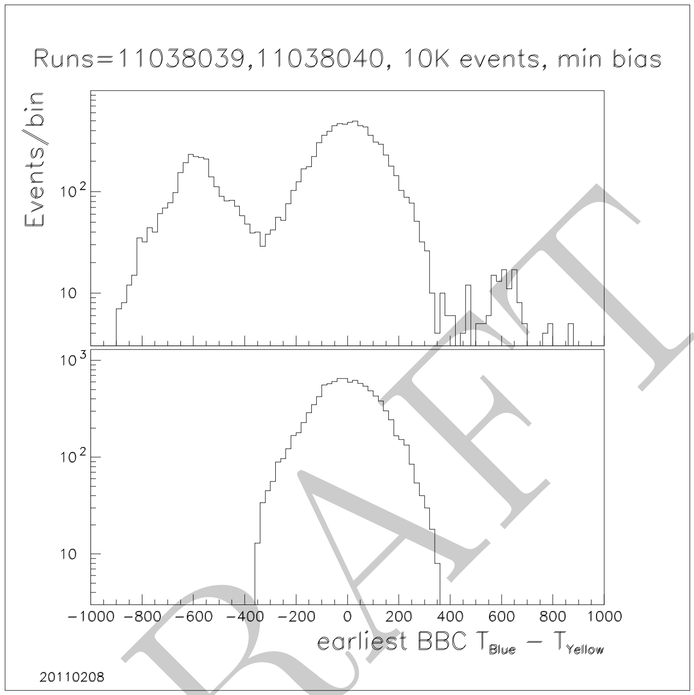

Figure 13: Distributions of the difference of earliest-hit time-to-amplitude (TAC) converter values from the Blue-facing and Yellow-facing BBC annuli. The top distributions do not include a cut on the TAC difference. The central peak is from collisions and is narrow for this run due to the ∼2mr bunch-crossing angle at IP2. The peak at negative values is for single-beam backgrounds induced by the Yellow beam. The small peak at large positive values is for single-beam backgrounds induced by the Blue beam. Single-beam background contributions varied from fill-to-fill, as monitored by event data without the TAC difference cut.

the difference between the Blue-facing and Yellow-facing BBC, as confirmed in offline analysis that uses this vertex for neutral pion reconstruction. This TAC difference cut is computed in an FPGA on the vertex DSM after valid data is transferred from the Blue-facing and Yellow-facing QT boards. The TAC difference discriminates collision events from single-beam background events. For collision events, the TAC difference is proportional to the vertex-z position.

During commissioning and to test data integrity, the DAQ was set up to record dedicated minimum-bias collision triggers at a rate of $\sim$2.4 kHz with essentially 100% dead time, with the rate limited by recording data from three clock ticks. For each event, data was acquired from the BBC, the ECal, the HCal, the preshower and the ZDC for the RHIC clock tick for which the trigger conditions were satisfied, the RHIC clock tick before the bunch crossing with the trigger (so-called "pre" crossing) and the RHIC clock tick after the bunch crossing with the trigger (so-called "post" crossing). Having the triggered, pre- and post-crossing data for each detector is a powerful means of identifying detector effects (*e.g.*, bad ground connections can produce pulse reflections or oscillations that persist beyond the 70-ns gate) and beam-induced backgrounds.

When the commissioning of A_NDY was complete, post-crossings typically had very small charge coming primarily from afterpulsing in the photomultiplier tube and pre-crossings were generally consistent with pedestal values. This is illustrated in Fig. 14 for the HCal modules. Systematic effects were studied for most fills by collecting data with and without the minimum-bias collision condition imposed in addition to the jet trigger. The resulting patterns of hit cells illustrates that the events are manifestly jet like. Comic-ray events (taken when there was no beam by requiring the HCal module sum to satisfy a 30-count threshold) showed clear tracks through the detectors (Fig. 15), confirming that all mappings in HCal were correct and establishing that the "jet-like" patterns for colliding beam events were associated with physics.

The same method of forming module sums and setting a threshold on the resulting sum was used to make a trigger on the ECal modules and a trigger on the ZDC. This is illustrated in a slightly different fashion in Fig. 16. The ECal module-sum trigger that we dubbed as the "π^0" trigger is common to all distributions. Shown in the figure are the BBC sums and the HCal sums, subject to this trigger. The biases are evident: relative to minimum bias events where BBC sums are symmetric, the Blue-facing BBC sees additional

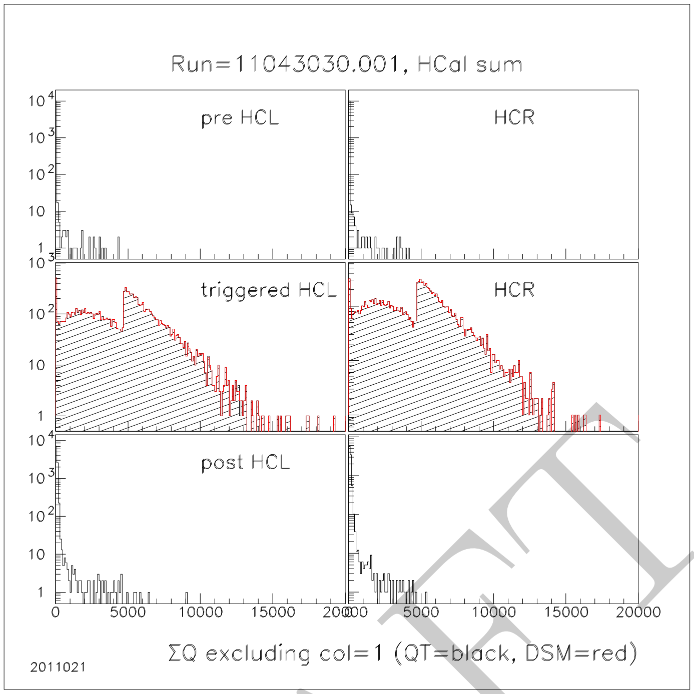

Figure 14: Charge distributions from the HCal jet-trigger. The jet trigger requires a threshold on the masked sum of ADC values from the 108 detectors in each module. For this data, the first column of detectors was masked from the sum, since the most interesting events have the thrust axis of the jet centered in the module. The black-shaded distributions are formed by summing the individual detector ADC values, subject to the same masking as used for the trigger. The red histogram is from the input to a DSM and contains the masked sum computed by the FPGAs. A valid event for the jet trigger has the DSM sum for either the beam-left (HCL) or beam-right (HCR) HCal module crossing a preset threshold. The top row of plots is for bunch crossings that precede the triggered bunch crossing by 107 ns and the bottom row of plots is for bunch crossings that follow the triggered crossing by 107 ns. The "pre" crossing distribution is mostly the 96-channel pedestal sum, with <1% of the events having charge (likely from room backgrounds). The "post" crossing distributions are again dominated by the pedestal, with a small probability of afterpulsing from the phototubes on HCal. The jet trigger was commissioned on day 46 of the run and was used to record data from essentially all of the luminosity delivered to IP2 (see Fig. 11). When the instantaneous luminosity was increased at IP2, the live time of the jet trigger was kept high by first changing the masking to exclude the outer two perimeters of detectors in a module, and then by raising the threshold.

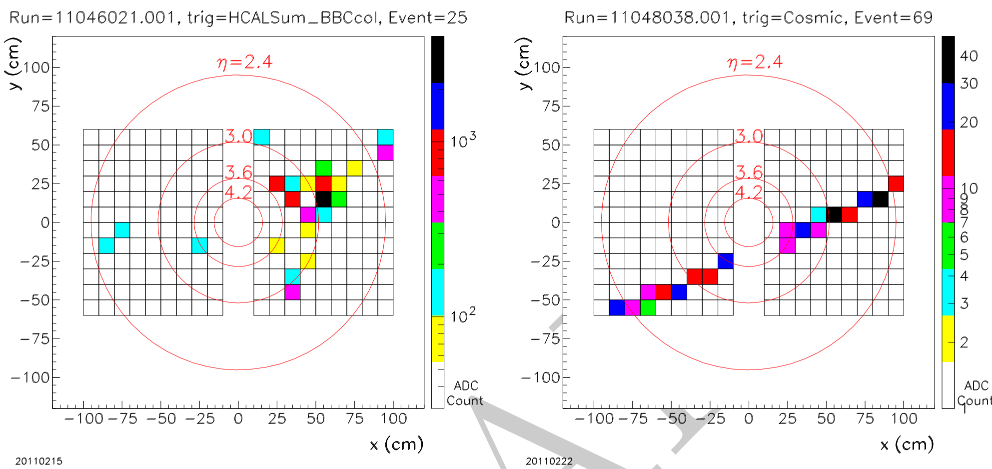

Figure 15: Event displays for the HCal arrays. This display represents the HCal modules as arrays as observed from the interaction point. The red circles show pseudorapidity for events with vertex-z=0. Colored boxes have hits in the corresponding detectors, with the color scale set by the ADC value recorded for that detector. (Left) an event from collision data acquired with the jet trigger, showing clear "jetty" structure. (Right) an event acquired two days later without beam with an analogous module-summing algorithm and a low threshold on the sum. This event clearly shows a cosmic-ray muon passing through both modules. An ensemble of cosmic-ray events demonstrates that the mapping of detectors is robustly understood. In total $> 7.5 \times 10^8$ jet events were recorded from the $\sim$6.5 pb^{-1} of integrated luminosity delivered to IP2. That data will provide first determination of the forward jet production analyzing power.

charge reinforcing the notion that forward neutral pion production at this pseudorapidity are fragments of forward jets. As well, the HCal module sums differ from minimum bias events, having a slower falloff in the event yield as the charge sum increases. This is expected if the neutral pion is accompanied by additional particles associated with a forward jet.

Triggering on the ZDC charge sum is of particular interest, since it is known that far forward neutron production has a non-zero analyzing power [21]. Far-forward neutron production is used for local polarimetry at STAR and PHENIX for $\sqrt{s} = 500$ GeV polarized proton collisions as a means of tuning the spin rotator magnets. Local polarimetry is of interest to many when the beams have vertical polarization. Fig. 17 shows the ZDC charge sum for events where either the Blue-facing or the Yellow-facing ZDC is above a preset threshold. A scintillator-strip shower maximum detector was built for the IP2 ZDCs, from an existing glued plane of scintillator strips recycled from an earlier forward calorimeter project. Scintillation light is collected by a wave-length shifting optical fiber inserted into a centered hole that is made during the extrusion of the triangular cross section strip. The fibers are then mapped onto pixels of a 16 channel Hamamatsu multi-anode photomultiplier tube. The charge from each of the 16 anodes is encoded for event readout. The ZDC shower maximum detector is installed in between the second and third modules of the ZDC. The purpose of the strips is to measure a θ, ϕ for the neutron in the event. The ϕ dependence of the spin asymmetries then provides information. The amplitude of the ϕ dependence is the analyzing power. The phasing of the harmonic dependence of the spin asymmetry on ϕ can provide information about both vertical and radial polarization components.

Fig. 17 shows the module sum distribution for the ZDC and the resulting analysis of spin effects from event data. The event analysis amounts to forming distributions of the number of events in a given ϕ bin for each bunch crossing. The distributions are incremented subject to requirements on the ZDC module sum, the threshold of relatively gain-matched charge in the ZDC SMD strip, and a large enough θ for the event. The polarization pattern is retrieved from a database archived in essentially real time from information broadcast by RHIC. This analysis methodolgy was then easily extended to bunch-crossing scalers. With suitable bit input to such scalers, the relevant distributions are accumulated at a maximum event rate of 9.38 MHz, with zero deadtime. Offline analysis provides azimuthal dependence of spin asymmetries. The plan is to perform real time analysis of such asym-

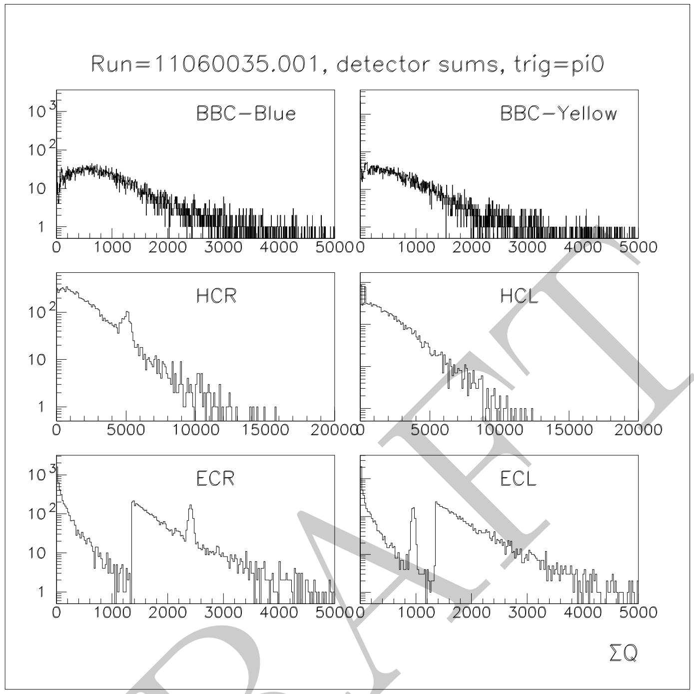

Figure 16: Module sums from the BBC (top), the HCal (middle) and the ECal (bottom) subjected to the neutral pion trigger (threshold on ECal module sum, as evident in the bottom row of plots). No additional conditions are on the data. The narrow peaks in ECL, ECR and HCR are from the light-emitting diode that also satisfies this trigger. The bias from the neutral pion trigger is evident in both the BBC and the HCal. For the BBC, more charge is observed in the Blue-facing BBC than for minimum-bias events, as expected if the neutral pion is accompanied by additional particles. The HCal sum distributions fall off less rapidly with increasing charge sum than for minimum bias, reflecting the additional particles that accompany the neutral pion.

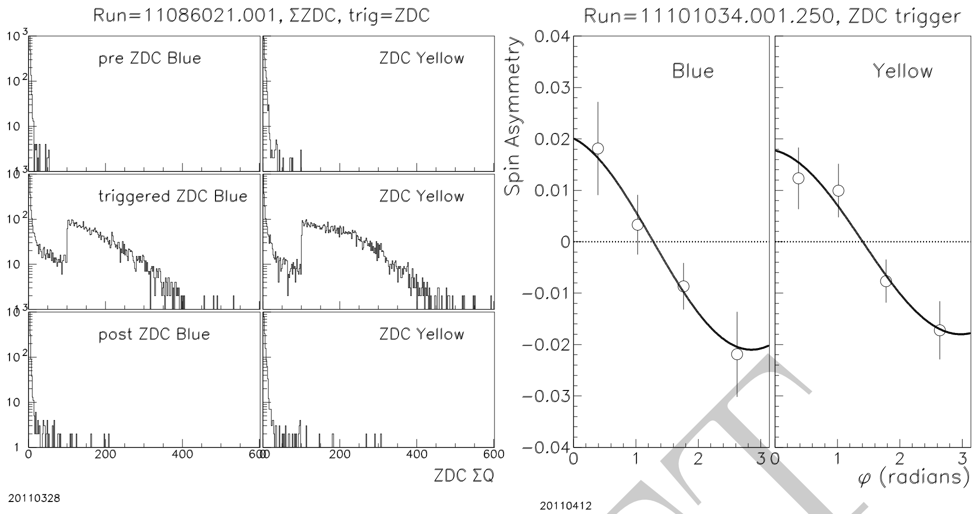

Figure 17: (Left) Module summed distributions from the ZDC subject to a trigger that either the Blue-facing or the Yellow-facing ZDC module sum is above threshold. Calibrations of the ZDC module relative gains were not possible until $\sqrt{s_{NN}}$=200 GeV Au+Au collisions were made at IP2. As for Fig. 14, distributions of the ZDC module sum response for 107-ns before the triggered crossing and 107-ns after the triggered are useful to assess backgrounds. (Right) Spin asymmetry from the Blue- and Yellow-facing ZDC, as analyzed from event data.

metries during RHIC run 13?

The ZDC modules were new to IP2 and were not absolutely calibrated prior to run 11. Consequently, A$_N$DY requested $\sqrt{s_{NN}}$=200 GeV Au+Au collisions so that the ~100 GeV neutron flux produced at 0° could be used to calibrate the ZDCs. IP2 was brought into collisions for two stores, after STAR and PHENIX had accomplished their goals. Fig. 18 shows the neutron peaks obtained after high-voltage adjustments were made to the IP2 ZDCs to calibrate the detectors. It will be necessary to look back at the ZDC event data from the polarized proton run to establish the impact of gain mismatching on the spin asymmetries.

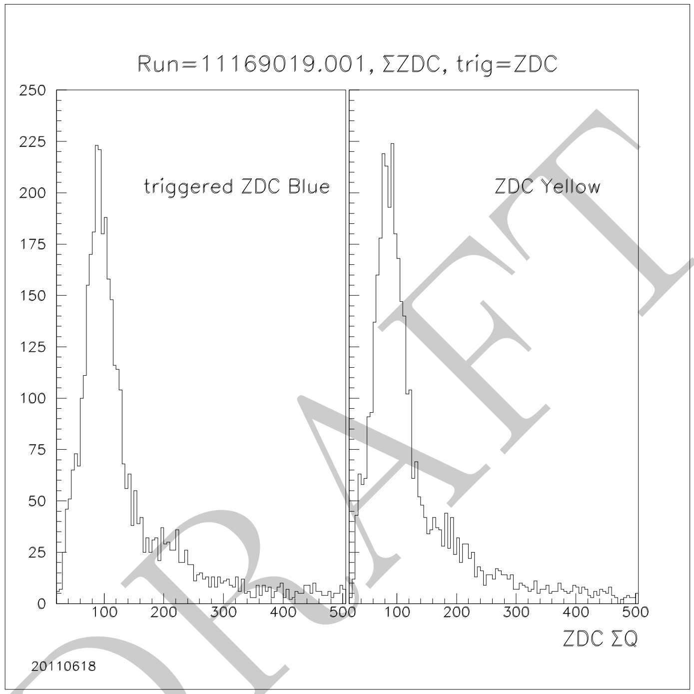

Figure 18: ZDC summed charge distributions obtained during $\sqrt{s_{NN}}$=200 GeV Au+Au collisions at IP2. These collisions were used to calibrate the three separate modules of the Blue-facing and Yellow-facing ZDC at IP2. Such calibrations are difficult in the absence of the peaked response from the $\sim$100 GeV neutron beam made at 0° by ultraperipheral Au+Au collisions.

2.5 Offline analysis

Offline analysis of the run-11 data was begun during the polarized proton run and has continued since. The analysis coding is an adaptation of coding developed for other forward calorimetry projects. Changes to this coding specific to A_NDY include an interface to the overall data structure and the specifics of the mapping of the raw data to the detector channels. The latter was greatly simplified by straight mappings of the connections to the readout electronics. At an early stage in developing this analysis coding, mapping of the PYTHIA/GEANT simulation output to become pseudodata was done so that the simulated pseudodata could be analyzed by the same coding as used for the real data. This method greatly facilitates comparisons of real data to simulation. Such comparisons are essential for a calorimeter based experiment to ensure that detector responses are understood and to assure that features in mass distributions are real rather than created from sculplted combinatoric backgrounds.

Association analyses can establish whether features in mass distributions are real. Once the basic data structures and mappings are in place, algorithms that have been well developed over the past ten years [22] can be applied to form energy clusters for the events and to analyze these clusters to attribute an x, y position to the cluster and to reconstruct the relativistic energy of the particle that initiated the calorimeter response from the energy of the cluster. Given that there is no magnet in the run-11 A_NDY configuration, particles produced in the collision follow straight-line trajectories from the event vertex to the x, y impact point at the calorimeter. It is necessary to attribute the z location of where the x, y measurements are made. The z position of the event vertex is reconstructed for each event from the time difference measurement (Fig. 13) , and the x, y location of the event vertex is assumed to be zero. With this line and the total relativistic energy, the four momentum is known up to identifying the type of particle that initiates the calorimeter response. The transverse attributes of the cluster are useful for discriminating incident photons, electrons or positrons from incident hadrons. A long-term goal of A_NDY is to robustly discriminate electrons or positrons from hadrons and photons by cross correlating multiple attributes of matched ECal and HCal clusters that are then also matched to the preshower response.

The calibration of the calorimeters is based on reconstruction of particles produced in the collision by identifying peaks in relevant mass distributions.

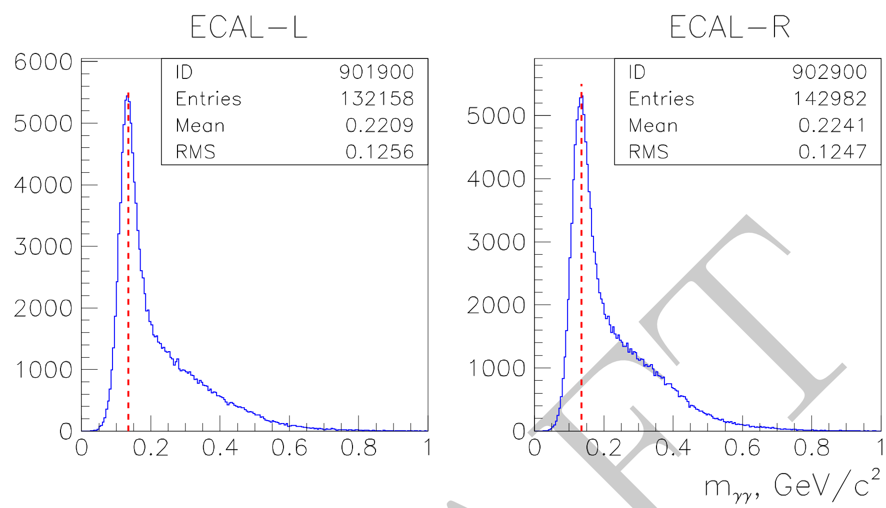

Figure 19: Cluster pair invariant mass from the run-11 A_NDY ECal modules after seven iterations of adjustments to the individual detector gains. A clear peak is observed from $\pi^0 \to \gamma\gamma$, whose identification is based on prior experience with similar calorimeters where extensive intercomparisons to simulations had been made. Such comparisons for A_NDY have been limited so far to energy spectra from the individual detectors. When comparisons are more complete, it is expected that the tail beyond the neutral pion peak will be identified as the ECal response to incident jet-like multiplicity. Online mass reconstructions allowed adjustments of detector high voltages based on offline gain corrections and measured gain curves for each ECal detector. Two such iterations were completed. More are required for hardware-level gain calibration.

This can correspond to cluster pairs, 3-cluster combinations, or more complex configurations. Association of the reconstructed mass for the event with a detector identified by the position of the leading cluster enables a means of establishing both relative and absolute gains for the calorimeter. This approach does require an iterative solution, especially when the cluster energy is spread among several detectors. Nonetheless, experience has shown this is a robust calibration method. For ECal, one step is taken after the clustering. This step involves fitting the parameters of shower shape functions whose basic form is determined from test beam data [23]. The fit results are then used in place of moments of the clusters. The result for the ECal stacks in place for the run-11 A$_N$DY configuration is shown in Fig. 19.

A primary goal of run-11 as noted in the introduction was to establish a robust calibration procedure for HCal, for which A$_N$DY proponents had no prior experience. A basic clustering algorithm (identifying groups of HCal towers with energy deposition above a threshold, bounded by towers at or below this threshold) was applied to the data (Fig. 20), albeit with many studies that varied the threshold of the cluster boundary, since the HCal matrix is formed from transversely large cells (10cm $\times$ 10cm) thereby resulting in greater chance for cluster merging. Furthermore, the transverse size of hadronic clusters is intrinsically larger than those made by incident photons, electrons or positrons. A complete association analysis of pseudodata from PYTHIA/GEANT simulations was an essential tool in the studies that culminated in determination of the HCal energy scale.

The association analysis amounts to using the primary particle four momentum from the PYTHIA event generation and the simulated vertex position for the event to reconstruct masses. Straight-line propagation of all particles from the vertex is done to determine their possible impact point at the HCal. This impact point is then compared to impact points deduced from the clustering analysis of the full pseudodata. If the impact points are within proximity, a match is declared and the identity of the cluster is then known. Fig. 21 shows the results from the proximity-based association analysis for special conditions on the clusters. Namely, the clusters required in this analysis had only a single tower, bounded by other towers that were below an energy deposition threshold of 0.08 GeV, and the towers had to be beyond the shadow cast by ECal. This event selection emphasizes incident photons. The cluster position requirement is imposed since ECal is built from 16 radiation length lead glass bars, meaning that most of the incident photon energy is converted into electromagnetic showers in ECal. The association

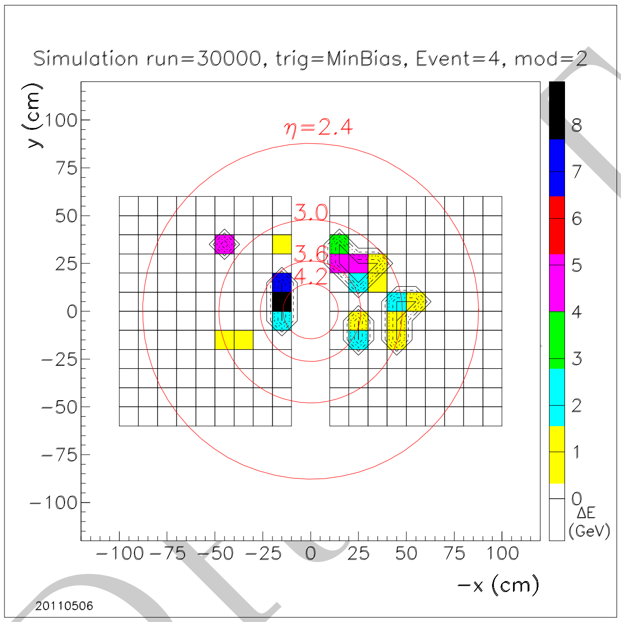

Figure 20: Single event display of pseudodata for HCal from PYTHIA/GEANT simulations and the contours representing the threshold-bounded clusters identified in the event. There are many examples where clusters are merged due to the coarse cell sizes that require careful tuning of the threshold for the cluster boundary

results for the position have the expected form. The matching of the cluster centroid (taken to be the center of the detector cell, since these clusters have no energetic neighbors to enable a position interpolation) to the impact point from the PYTHIA primary is essentially a truncated uniform distribution. The truncation is at ±5 cm as set by the Moliere radius of electromagnetic showers in HCal detectors and the requirement for single-tower clusters. Also shown in Fig. 21 is the pair mass distribution from PYTHIA/GEANT simulations, where the association analysis allows identification of the incident particle that deposited the energy. It is clear from this analysis that neutral pions are reconstructed in the cluster pair mass distribution. This is not so surprising, since neutral pions are by far the dominant source of photons produced in p+p collisions at $\sqrt{s} = 500$ GeV. What may be somewhat surprising is that the photon showers are well measured in both position and energy. Most hadron calorimeters are shadowed from collision vertices by electromagnetic calorimeters, so cannot see photons produced by collisions. The fiber density in the HCal detectors is large (47×47 matrix of 1-mm diameter scintillating fiber [13]), therefore allowing a good measurement of electromagnetic showers produced by incident photons.

The same analysis method as used for the simulation is then applied to 20 million minimum-bias triggered events, that include a vertex cut, acquired from three different RHIC fills. The resulting mass distributions are then overlayed with analogous distributions reconstructed from 20M non-elastic, non-singly diffractive events generated by PYTHIA 6.222 that are run through GEANT. No scaling factors are applied to any of the distributions for the overlay shown in Fig. 22. There is excellent agreement between data and simulation. The mass peaks in data are then quantitatively analyzed to establish that the absolute energy scale of HCal is determined, at present, to ∼5%.

A summary of the run-11 effort is that the primary goals set in the 2010 letter of intent [2] have been accomplished.

- Collisions of the intense polarized proton beams can occur at IP2 without significant impact on operations at IP6,IP8. The integrated luminosity projected for runs 13,14 at IP2 while IP6 and IP8 are acquiring events for their measurements of parity violation for W production is sufficient for the first transverse spin Drell-Yan production experiment, using the apparatus we propose to build as described later in this document.

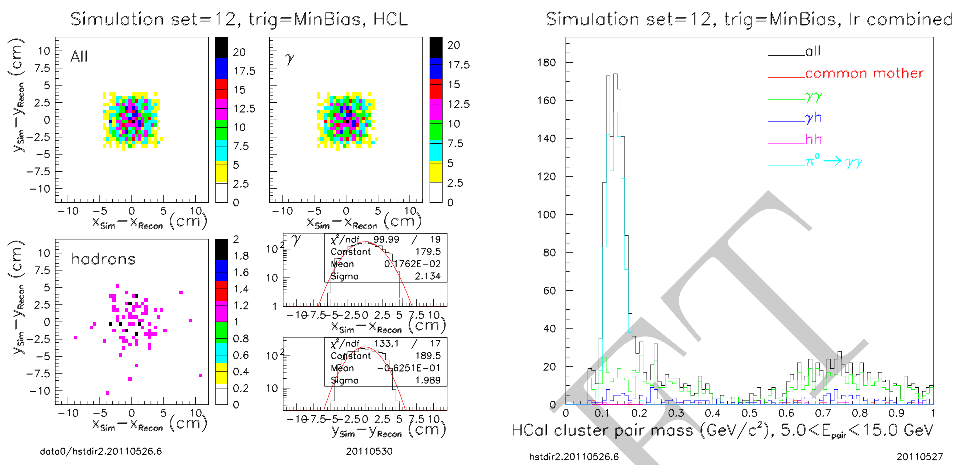

Figure 21: (left) Results from the proximity-based association analysis of full PYTHIA/GEANT simulations showing the position differences between projections of particles generated by PYTHIA to reconstructions of PYTHIA/GEANT simulations. This step is preceded by an intercomparison of data and simulation that establishes that the PYTHIA/GEANT model gives a good description of the data, as expected from such comparisons made with other forward calorimeter projects done at RHIC. The reconstructed clusters are subjected to event selections that significantly suppress the hadronic response: single-tower clusters bounded by towers with $\Delta E < 0.06$ GeV with an addition requirement that the x, y location of the cluster is outside of the shadow cast by ECal. (right) The selected clusters are then converted into four momenta of incident particles, assuming they are produced at the event vertex and that they are photons, using a scaling factor to convert cluster energy into incident total relativistic energy. Invariant mass is then computed from inclusively pairing all such clusters for the event. The association tag then allows a decomposition of the pair mass spectrum to show that the peak at 0.135 GeV/c^2 is due to $\pi^0 \to \gamma\gamma$ decay.

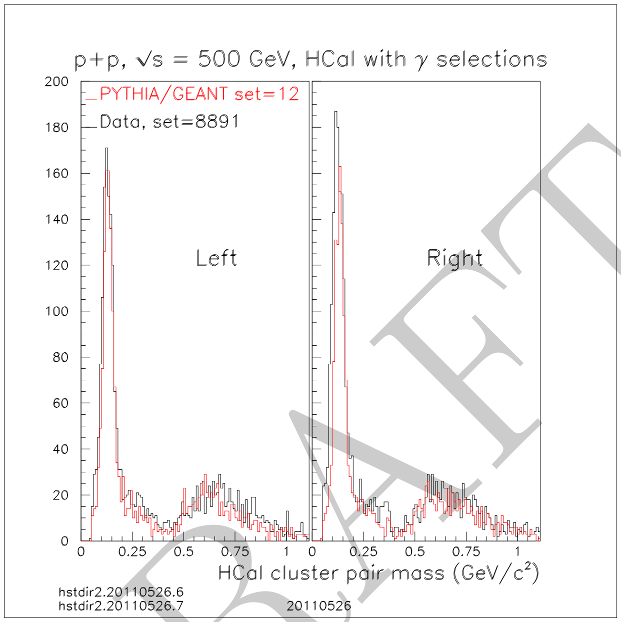

Figure 22: Comparison of pair-mass distributions reconstructed from data with those reconstructed from simulation for clusters subjected to photon-like requirements described in the text and in the Fig. 21 caption. The peak near 0.135 GeV/c^2 is from $\pi^0 \to \gamma\gamma$ events and establishes that the energy scale of HCal is known to $\sim$5%, as confirmed by an association analysis of the simulations (Fig. 21). The near quantitative agreement between data and simulation is a strong indication that the PYTHIA/GEANT model gives a good description of the data. The peak near 0.6 GeV/c^2 is from sculpted combinatoric backgrounds as shown by the association analysis.

- The HCal modules configured for run-11 have been calibrated to ∼5%. Further work on calibration is required to establish that the hadronic showering model in GEANT properly accounts for the deviations from a perfectly compensated calorimeter.

When that work is complete, jet clustering algorithms can be applied to the data and a jet-energy scale will be established. The first measurement of the analyzing power for jet production will then be possible.

The first comparisons of PYTHIA 6.222/GEANT simulations to the data show good agreement. This supports that the QCD background estimates made for the A_NDY proposal (Appendix 1) are valid. Further work is required here to benchmark the simulations. The run-11 data set can provide some indication of the spin-dependence of the QCD background to the Drell-Yan production signal that later runs will identify. The matching of clusters between ECal and HCal for the run-11 data is an important step for the benchmarking.

Any concerns about significant differences in single-beam backgrounds being worse at IP2 than at IP6 have been laid to rest by the run-11 data. The background environment in this forward region is well controlled at RHIC by the cryostats containing the ring magnets and by the collimation system. This provides RHIC a unique opportunity to make the first transverse spin DY production measurement. Although backgrounds were not found to be large, attention will be required in future runs to optimize single-beam backgrounds at IP2. The focus on run-11 was simply to establish collisions and precluded significant attention to single-beam background optimization.

The run-11 A_NDY experience has also established that the analysis tools developed over the past ten years are flexible and can be readily morphed into different calorimetric configurations. We propose to construct such a different configuration in run-13. Care and effort will be required to assure that the calorimeter detectors are well constructed and properly mapped to the electronics. The experienced group that has been formed for A_NDY is fully cognizant of the quality requirements and is capable of achieving them. Reconstruction coding will be an essential component of commissioning, so the flexibility demonstrated from run 11 bodes well for the future. With all of this said, the A_NDY goals for run-13 of clear observation of the $J/\psi \rightarrow e^+e^-$ and $\Upsilon \rightarrow e^+e^-$ decays and the intervening di-electron mass distribution from a newly constructed experiment are indeed ambitious. The A_NDY proponents believe the implementation described below for run-13 is robust and can be completed, although we are fully cognizant of the significant effort that will be required. The project risks are understood by the proponents through the best possible design tool: namely model building. The run-11 implementation can be viewed as the model that demonstrates the viability of the proposed configuration for run-13.

2.6 Dilepton Reconstruction from Run-11 Data

The robust reconstruction of $\pi^0 \to \gamma\gamma$ in both the ECal and HCal invites the question of whether A$_N$DY methods can be applied to run-11 data to extract a di-lepton signal; *i.e.*, $J/\psi \to e^+e^-$. Such a signal can provide confidence that the proposed A$_N$DY apparatus will be capable of measuring Drell-Yan production.

It must be kept in mind that the run-11 apparatus has limitations compared to what we propose here:

- The preshower that we propose has substantially more granularity than what was in place for run 11. Consequently, background suppressions in run11 will not match expectations from GEANT studies in the A$_N$DY proposal (see Section 5). Indeed, the Blue-facing beam-beam counter turns out to provide the most critical background suppression, as described below. The proposed preshower for A$_N$DY is ten times more granular.

- The acceptance for dileptons in the run-11 apparatus is predominantly from the HCal. Electromagnetic showers are preferentially selected from HCal by considering single-tower clusters, bounded by towers with small energy deposition. The position resolution for HCal clusters is at least 10× worse than for ECal, due to the coarse granularity. This poor position resolution impacts the ability to identify which preshower detector to query for the photon/electron discrimination.

Even with these caveats, it is instructive to proceed, given the prospects of understanding better how the proposed apparatus will perform. As described below, we observe ∼120 $J/\psi \to e^+e^-$ events (Fig. 3) from a data sample consisting of $3.5{\times}10^7$ triggers. The factor of 3×10^5 event suppression represents a major part of what is required to access DY events.

Data obtained with the ECal trigger (Fig. 16) are the natural source for attempts to extract a di-lepton signal from the run-11 data. Only a limited data sample was acquired with this trigger, since the focus for run-11 had been on the jet trigger (Fig. 14). To accompany this data, the run-11 GEANT model was used to simulate detector responses from 0.5 pb^{-1} of integrated luminosity from non-elastic, non-singly-diffractive PYTHIA 6.222 events. These events were first filtered by requiring that the summed total relativistic energy of particles projected into the ECal acceptance exceed 10 GeV. Prior experience has shown that such filters are crucial to generating simulation samples that can be compared to data. Computer resources (CPU and disk space) are minimized by filtering events before they are run through GEANT.

The first step towards this goal is to compare data and simulation for the HCal response. Such comparisons were made for the jet-triggered events [24]. In general, simulation is found to explain data distributions. The events are dominated by QCD jets, as expected. The data/simulation comparison shows that the neutral pion based calibration of the HCal provides a good starting point, although ∼20% corrections for hadron initiated showers are still required.

The next step is to extend the association analysis discussed in Sec. 2.5 to the ECal+HCal pair mass distribution, so as to understand the composition of the background. The clusters considered from the HCal for this pair mass distribution are described above. HCal clusters are excluded from consideration if they can be paired with a second HCal cluster to yield an invariant mass $M < 0.2$ GeV/c^2. The simulation is used to determine the primary particles that give rise to the large-mass cluster-pair background (Fig. 23), using proximity association described above. It is found that the background is dominantly from photons. This is not so surprising given that imposition of a minimum x_F in this rapidity interval kinematically suppresses jet pairs. The two-photon decay of the neutral pion is a way to generate pairs at large mass through the opening-angle distribution for this decay.

Given the photon dominance of the background, the beam-beam counter provides the primary means of distinguishing electrons and positrons from photons, since this array is the first active element particles see upon exiting the beam pipe. Photon conversions and electron/positron brehmsstrahlung in the BBC means that the preshower detectors see partial showers, so are unable to make the necessary discrimination. The requisite discrimination is established by requiring the BBC element matched to the projected position of the cluster from either ECal or HCal to have a charge corresponding to a minimum-ionizing particle (*i.e.* the large peaks in Fig. 12). The

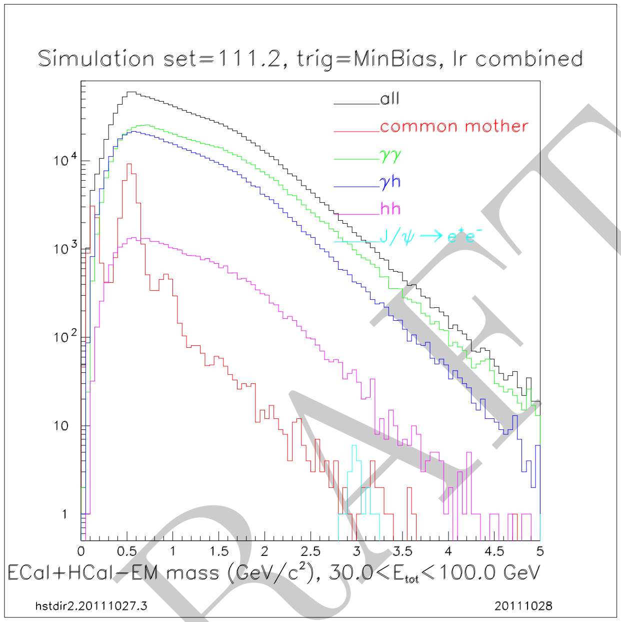

Figure 23: Association analysis of the mass distribution when an ECal cluster is paired with an HCal cluster. Filtered PYTHIA 6.222 simulations require summed total relativistic energy $>$ 15 GeV for primaries projected from a vertex distribution into the acceptance of ECal. GEANT simulations provide the detector response for PYTHIA events meeting the filtering criteria. Reconstruction proceeds on these simulated events, followed by a proximity association of reconstructed clusters with projected primaries. The large-mass background is primarily from photons.

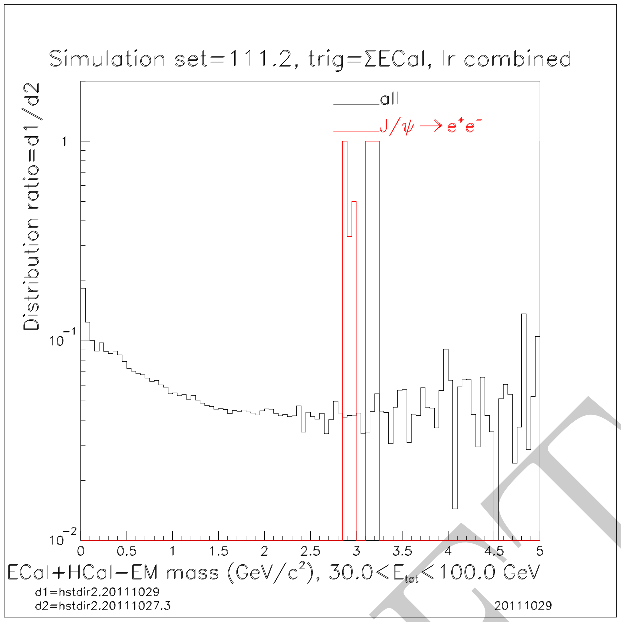

Figure 24: Ratio of the pair-mass distribution including the BBC requirement that clusters have a MIP-like response to the distribution without this requirement. The BBC requirement supresses the background by a factor of 25, and mostly preserves the di-lepton signal from *Jpsi* decays.

PYTHIA/GEANT simulations show (Fig. 24) that the background is suppressed by a factor of 25 after imposing the BBC requirement. It is also evident in this figure that dileptons from J/ψ decay are mostly unaffected by this requirement, although PYTHIA 6.222 grossly underpredicts the J/ψ yield in this rapidity range, so the simulations have limited statistics for J/ψ production relative to the data. The NRQCD model in PYTHIA 6.425 includes both color-singlet and color-octet matrix elements for onia production, and has been found by the ATLAS collaboration to give a good description of onia yields at the LHC [25]. Naively, we expect 100× more photon suppression then what is achieved in Fig. 24, based on single-particle studies presented in the A_NDY proposal. The position resolution from the HCal and the occupancy in the BBC both serve to reduce the effectiveness of the discrimination by multi-particle effects: *e.g.*, a single BBC tile can have both a charged hadron and a photon pass through it, thereby mimicking the response expected for an electron or positron. The proposed A_NDY apparatus remedies both position resolution and granularity issues.

The final step is to refine the calibrations, including the critical reconstruction of the z-component of the vertex and the relationship between deposited and incident particle energy for the HCal. For the z_{vertex} reconstruction, single-beam background particles provide one calibration of the TAC difference between Blue-facing and Yellow-facing BBC, assuming these particles have $\beta \to 1$ and using the measured positions of the arrays. The single-beam background measurement provides a ∼15% larger calibration constant than provided for by optimizing neutral pion masses, for cluster pairs in both ECal and HCal. The source of this discrepancy is still unresolved. The z_{vertex} reconstruction plays a much more important role for J/ψ reconstruction, since $\delta M/m \propto \delta z/z$. The HCal calibration was refined by association of the mass distribution for each event with the leading cluster of the pair. In that manner, peaks from $\pi^0 \to \gamma\gamma$ are observed for individual HCal detector, except for those shadowed by the ECal module. Iteratively adjusting calibration factors to assure that the peaks are at the physical neutral pion mass was used for fine tuning the HCal calibration.

After these steps were taken, the cluster pair mass distribution observed in the run-11 data obtained with the ECal trigger are shown in Fig. 3. A clear peak from $J/\psi \to e^+e^-$ is observed in the data. A strong indication for $\psi(2S) \to e^+e^-$ is also observed, as expected from earlier di-lepton studies.

The reconstructed $J/\psi \to e^+e^-$ yield provides ∼120 events in the peak. Accounting only for geometric acceptance of ECal and HCal and the energy thresholds, 420 events are expected from the NRQCD model in PYTHIA 6.425 in a 0.5 pb^{-1} data sample. Although a full evaluation of the reconstruction efficiency is not available at this time, inefficiencies from the geometrical acceptance of the BBC array and the clustering parameters used for HCal are crudely estimated to provide 25% efficiency. The NRQCD model does not include possible contributions from intrinsic charm components of the proton wave function. The yield observed for $J/\psi \to e^+e^-$ is reasonable.

The NRQCD implementation in PYTHIA 6.425 can then be used to address the ratio of $J/\psi \to e^+e^-$ production events to Drell-Yan production events, subjected to the geometric and energy conditions used in Fig. 3. With the further requirement that the virtual photon mass is larger than 4 GeV/c^2, PYTHIA 6.425 predicts this ratio is 170. Consequently, further background reductions of at least this magnitude are required from the proposed A$_N$DY apparatus. There are two primary sources that can provide this requisite reduction.

- The granularity of the proposed preshower detector and the elimination of the position uncertainties in the association of calorimeter clusters with specific preshower detectors will enable us to approach the single-particle limit of 98% rejection of photons, from the current level of ∼80% rejection. This is a further suppression of a factor of ∼10 per cluster, or a factor of ∼100 suppression of the pair mass background.

- When photons are sufficiently suppressed, hadron backgrounds will be the dominant background source. Estimates from the original A_NDY proposal are that $\geq$ 97% of hadrons can be rejected from analysis of the longitudinal shower profile available from the HCal and preshower detectors. Given that the lepton daughters will provide independent rejection capability from this shower analysis, another factor of >1000 suppression of the pair mass background is possible.

The ratio of $J/\psi \to e^+e^-$ to Drell-Yan events for the ECal+HCal electromagnetic cluster pairs used in Fig. 3 also enables an assessment of how many DY pairs will reconstruct in the full A_NDY apparatus. The estimate is that the dileptons in Fig. 3 represent ∼10% of what will be achieved with the full A_NDY apparatus. The acceptance limitations of ECal are the primary factor that will be addressed in going from the run-11 apparatus to the proposed A_NDY configuration. Another key is to lower the energy thresholds for the electron/positron observation. Extracting signal above background at lower energies is a key factor, beyond just the acceptance, to realize the 9400 DY events in a 100 pb^{-1} data sample.

Demonstration that $J/\psi \to e^+e^-$ can be extracted from QCD backgrounds in the run-11 data provides confidence that Drell-Yan can be extracted with the full A_NDY apparatus.

3 Electromagnetic Calorimeter (ECal)

The heart of the A_NDY apparatus is the BigCal electromagnetic calorimeter we have borrowed from JLab. Groups from Jefferson Laboratory (JLab) who had previously measured the electric form factor of the proton to high Q^2 using BigCal have joined the A_NDY project (see Fig. 25). The terms of the loan agreement are to return the calorimeter to JLab by 31 July 2014 for its planned use in experiments with the 12-GeV electron beam. This return date is non-negotiable and sets the timescale for A_NDY.

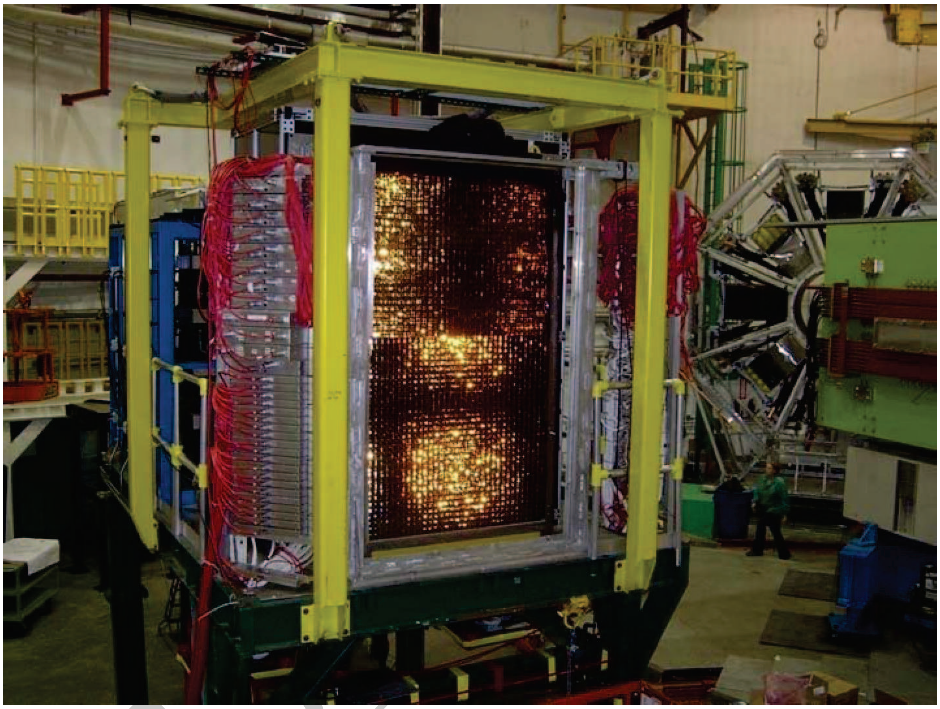

Figure 25: Photograph of BigCal at Jefferson Laboratory. The lead-glass calorimeter was constructed for measuring the electric form factor of the proton. It consists of a 24-row×30-column submatrix of $(40\ \mathrm{mm})^2 \times 40$ cm lead-glass detectors atop a 32-row×32-column submatrix of $(38\ \mathrm{mm})^2 \times 45$ cm lead-glass detectors. Each detector is viewed by an FEU-84 photomultiplier tube. In total, there are 1744 lead-glass detectors in BigCal. BigCal is on loan for the A_NDY project until 31 July 2014.

The primary conclusion from our run 11 tests is that beams can collide at IP2 with minimal impact on operations at STAR or PHENIX. The run-11 experience has also allowed the Collider-Accelerator physicists to project that 10 pb^{-1} / week of luminosity can be delivered to IP2 for A_NDY during $\sqrt{s}$=500 GeV polarized proton operation. For a 10-week run, this is a smaller data sample than initially assumed in the Letter of Intent [2]. Imposing a requirement $x_F < 0.3$, as required to test the predicted sign change, also results in fewer DY events. Consequently, an optimization of the A_NDY acceptance has been done.

Multiple geometries for ECal have been considered in the optimization of the A_NDY acceptance. The best choice proves to be an azimuthally complete ECal implemented by two stacks of lead-glass detectors, each on a base plate supported by bearings sliding on Thomson rails. The motion of each stack is transverse to the beams. The azimuthally complete ECal is realized when the two stacks are moved together. Each stack has an embedded insert that forms a hole for the vacuum pipe for the beams when the ECal is in its closed position. Motion of the stacks away from the beam is required to allow a close packing of ECal and HCal and the servicing of ECal. The stacks are also moved away from the beam to limit the formation of radiation-induced color-trapping centers in the glass during heavy ion running.

The inner and outer calorimeters have cells with a size mismatch. The central 30-row $\times$ 30-column hole of the outer calorimeter is too small using nominal transverse cell sizes for the 32row $\times$ 32-column matrix of $(38\ \text{mm})^2\times$ 45 cm lead-glass bars. The size mismatch can be accommodated by strategic placement of 0.79 mm thick FR4 shim pieces that are readily available from commercial suppliers. We have used this method in earlier calorimeters. The shim can be included in the GEANT model of the calorimeter. Exact accounting of shim pieces awaits transverse cell size measurements for the $(40\ \text{mm})^2\times$ 40 cm lead-glass bars. Nominal sizes are used for Fig. 26, and 0.79 mm thick shims are assumed to be placed between every row. The mismatch in the columns is accounted for by a gap at $x = 0$. Such a gap is present in any case to allow for the enclosure.

The modular design of A_NDY (model=2 in the LOI) was our initial plan in the Letter of Intent [2]. There was a 3-year plan for A_NDY specified in that document. The first year was the run-11 configuration, with its modular left/right symmetric HCal. The second year, covered by this proposal, was to have left/right symmetric ECal constructed in front of the existing HCal. We were forced to abandon this option to ensure sufficient statis-

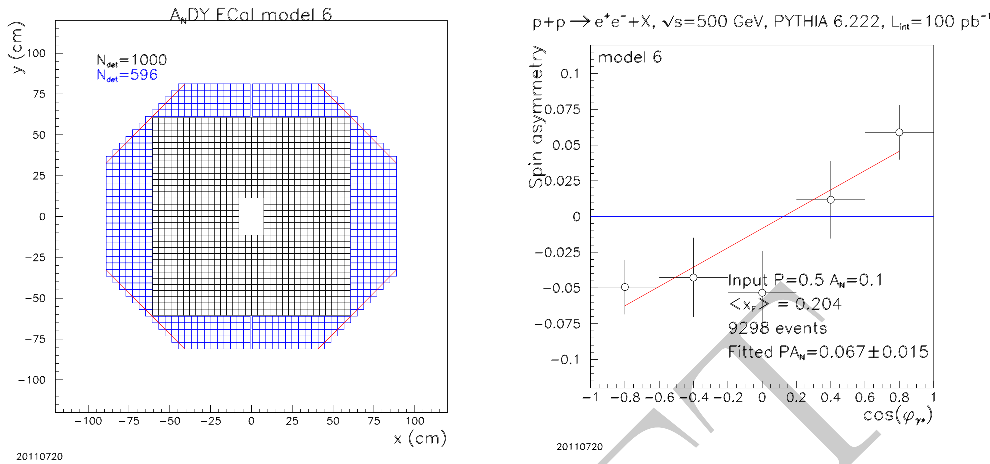

Figure 26: (left) Proposed configuration of the A$_N$DY ECal as seen from IP2. The inner calorimeter is a 32-row × 32-column matrix of (38 mm)^2× 45 cm lead-glass detectors with a central 6-row × 4-column hole for the vacuum pipe for the beams. The calorimeter is surrounded by (40 mm)^2× 40 cm lead-glass detectors from BigCal, with corners clipped to match the channel count. The full symmetry is broken by the $|y|$ extent of the outer calorimeter being smaller than the $|x|$ extent, as set by mechanical constraints. This outer calorimeter has a central 30-row × 30-column hole into which the inner calorimeter fits. The row/column matching of the two detector types is identical to that used in BigCal. This view shows the calorimeter in its closed position. The calorimeter separates into two halves that can be translated to larger $|x|$. (right) Simulated sensitivity to the spin asymmetry for Drell-Yan production assuming the acceptance of ECal as given by the ECal configuration and 100 pb$^-$1 of polarized proton collisions at $\sqrt{s}$=500 GeV. This simulation assumes 100 pb^{-1} of integrated luminosity for polarized proton collisions at $\sqrt{s} = 500$ GeV with 50% beam polarization. It further assumes an A$_N$=0.1 for DY production. The product $\epsilon = P_{beam}A_N$ is what determines the slope of the linear dependence on cosϕ_{γ^*}. Kinematic restrictions on the virtual photon are $M > 4$ GeV/c^2, $p_T < 2$ GeV/c and $x_F < 0.3$ as required to test the theoretical prediction of a sign change for the analyzing power for DY production relative to that measured for semi-inclusive deep inelastic scattering.

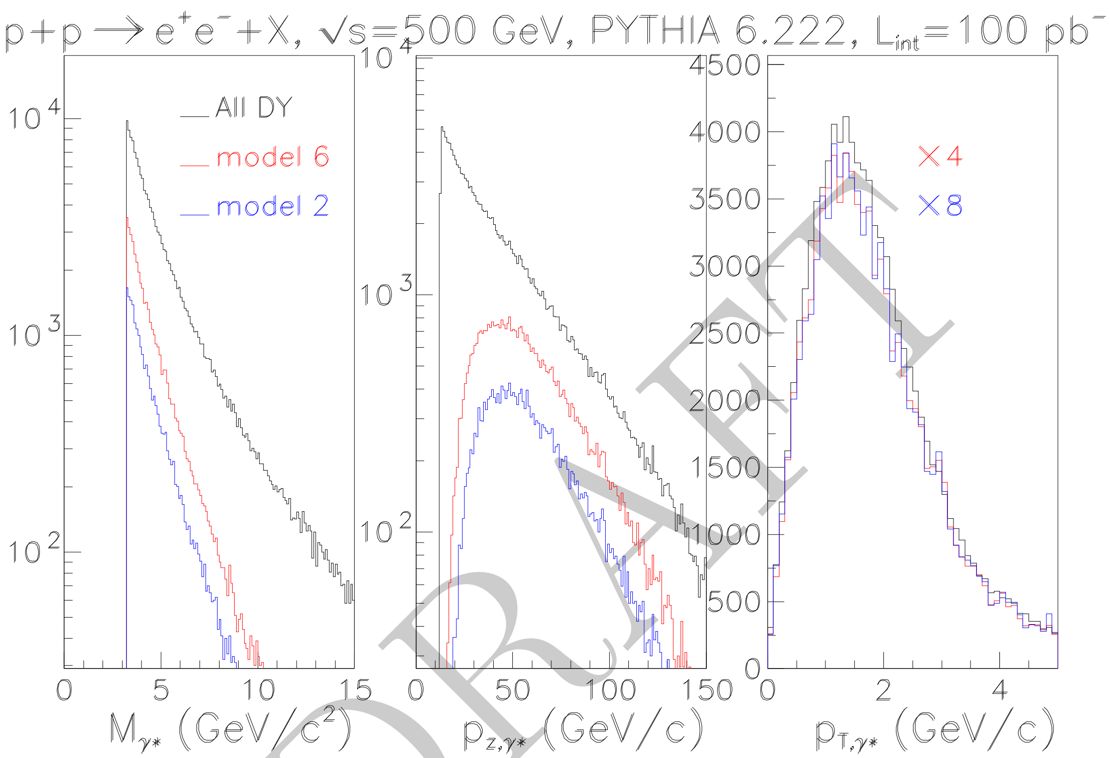

Figure 27: Distributions of virtual photon kinematic variables subjected to acceptance of different models of the A$_N$DY apparatus. Model=6 includes the A$_N$DY acceptance described in this document. Model=2 is the original modular design. The increased acceptance of model=6 offsets the difference between initial expectations for integrated luminosity and projections based on the run-11 experience.

tical precision for the sign change measurement. The basic requirements of ECal for A_NDY consist of overall acceptance, hermiticity, resolution, gain adjustability, gain stability, and serviceability. Acceptance is discussed below. Hermiticity ensures minimal transverse shower leakage. This requirement is met by close-packing the glass in the calorimeter. The inner calorimeter will not require any shim pieces. Prior experience indicates that the transverse dimensions of the Protvino glass have a narrow distribution. Close-packing can be facilitated by suitable selection of the detectors in stacking ECal. The resolution requirement can be intrinsically met by lead glass (typically providing 1000 photoelectrons in response to 1 GeV electron-energy equivalent of incident energy), so long as individual detectors share a common ground only at the HV power supply and at the readout electronics, and the noise levels of the readout electronics are small. Gain adjustability and stability sets requirements on the HV system, discussed in section 3.4. The gain stability will be measured by a monitoring system described in section 3.5.

The acceptance requirement is set by estimates of DY event totals assuming delivered luminosity of 10 pb^{-1}/week and 10 week runs. The objective is to measure the analyzing power for DY production to sufficient precision to test the theoretical prediction of a sign change, relative to SIDIS. This test requires restricting $x_{F,\gamma^*} < 0.3$ to match the kinematics of SIDIS. Acceptance simulations demonstrate that the acceptance is adequate to test the sign change with the optimized design. Comparisons are made between the optimal acceptance and the original modular concept (model=2).

3.1 ECal major mechanical design

Each ECal stack will be supported on a strong base plate, attached to bearings that are mounted on Thomson rails to provide motion of each half perpendicular to the beams. ECal will be elevated to beam height using vertical lift tables obtained from AGS-E949. Finite element analysis (FEA) calculations have been completed to establish that deflections of the vertical lift tables and the base plates are minimal. A technique that has worked in the past to make an azimuthally complete calorimetric coverage is to construct an insert that gets included with the lead-glass detector stack. This insert is designed to handle the load of the glass stacked on top of it. FEA calculations have established that sufficient strength for the insert, including a safety margin.

A light-tight enclosure will be built around each calorimeter half on a

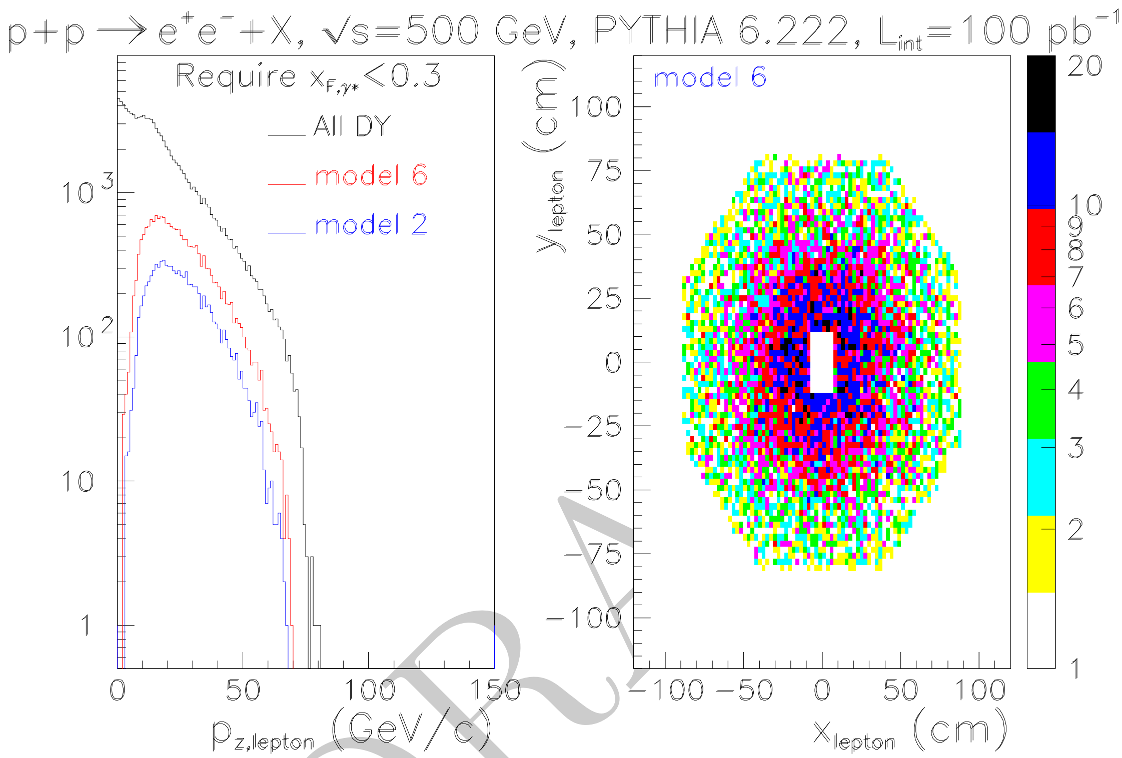

Figure 28: Electron and positron energy distribution (left) and ECal impact position correlation (right), subjected to requirements on virtual photon $M > 4$ GeV/c^2, $p_T < 2$ GeV/c and $x_F < 0.3$. The p_T cut on the virtual photon assures sensitivity to spin- and transverse-momentum dependent distribution functions. Model=6 includes the A$_N$DY acceptance described in this document. Model=2 is the original modular design. The increased acceptance of model=6 offsets the difference between initial expectations for integrated luminosity and projections based on the run-11 experience.

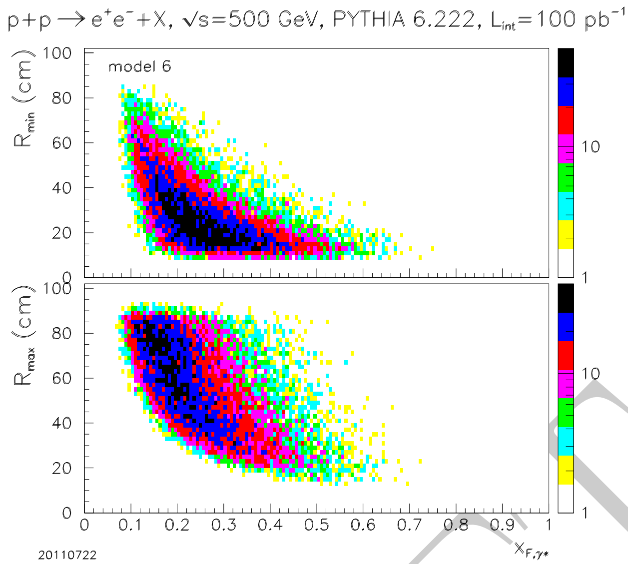

Figure 29: The distance R of the lepton from the beam when projected to ECal is correlated with the Feynman x. The challenge for the acceptance is to ensure large enough areal coverage and still provide acceptance close to the beams.

framework attached to the base plate. The enclosure will include patch panels to feed through the current pulses from each photomultiplier tube and control signals for the proposed Cockcroft-Walton bases. Feedthroughs will be on the large $|x|$ side of the enclosures so that the separation between ECal and HCal can be minimized, as required to ensure robust matching of ECal and HCal clusters. The mean transverse momentum of particles produced in hadronic showers will negatively impact the cluster matching if the z separation is too large. As discussed in Section 3.5, a rack of ECal readout electronics will be in proximity to each ECal half to minimize the cost for cabling.

3.2 ECal construction plan

Experience with the small-scale ECal implemented for RHIC run 11 indicates that the annealing done after the high-luminosity experiment at JLab was quite effective. As per agreement with our JLab colleagues, a fixed light source will be used to characterize the transparency of each lead-glass bar. In these measurements, the basic operation of FEU-84 coupled to that detector

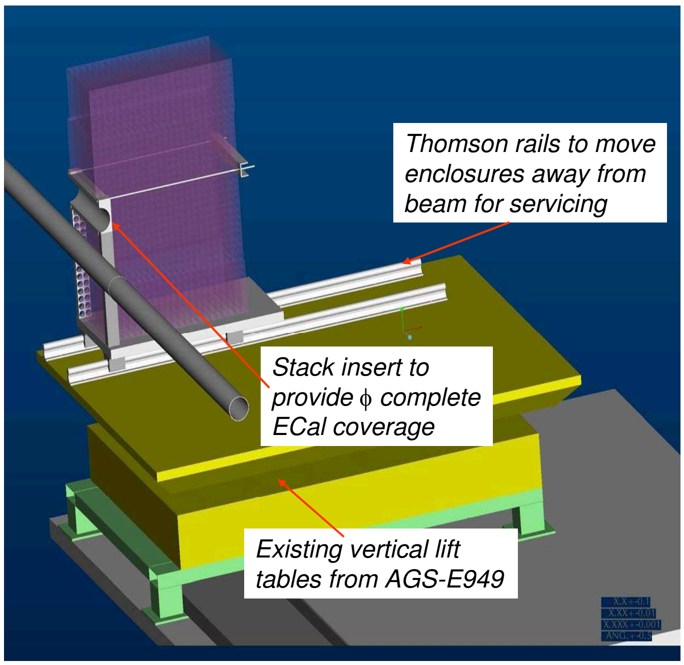

Figure 30: Engineering design of one A$_N$DY ECal half showing the platform to elevate ECal to beam height, the stack insert to enable the two halves to close around the beam pipe and the Thomson rails used for translating the calorimeter halves perpendicular to the beam pipe.

will get verified and the effective gain of the FEU-84+lead-glass bar will get measured. In addition, six measurements of transverse glass sizes will get made so as to optimize the hermiticity of the glass stack.

The FEU-84 will get optically coupled to the lead glass in one of two methods. The (40 mm)^2 have substantial vanadium blocks glued to the glass to serve as phototube holders. Threaded rods will be screwed into pre-existing tapped holes (insert picture). A phototube holder prestamped with the pin pattern of the FEU-84 is then captured by two threaded rods and pushes the phototube against the glass. A thin film of optical grease between the FEU-84 entrance window and the lead glass will then complete the optical coupling. The (38 mm)$^2\times$ 45 cm lead-glass bars will employ a phototube holder matrix constructed for BigCal at JLab. This matrix is a substantial aluminum plate with holes precisely drilled for a matrix of FEU-84. Each hole is accompanied by threaded holes for threaded rods and result in a comparable method of achieving the optical coupling as for the other detectors. The fixed matrix of holes for the FEU-84 will require a matching of the physical dimensions of the glass in the stack, so that accumulated deviations of the actual glass dimensions does not lead to a mismatch between the precision hole spacing of the phototube holder over the 32 columns that the phototube holder covers. One difference of the A$_N$DY configuration over BigCal is that the central rows of the detector have an insert. We plan on building special phototube holders for these central rows that double as structural support for the insert. Finally, the bottom rows of (40mm)$^2\times$ 40 cm lead-glass bars will have analogous phototube holders fabricated, so as to support the existing phototube holders for the upper rows.

After shipment to BNL, the glass was staged in the climate controlled 1002B building. The plan is to do the transparency measurements, phototube coupling, effective gain measurements and lead-glass size measurements after moving portions of BigCal into 1002D. From there, the plan is to immediately begin stacking ECal. It is estimated that the individual detector measurements and stacking can be completed in ~50 days, by sustaining a throughput of 32 cells per day.

3.3 ECal high voltage (HV) system

The JLab BigCal detector provides 660 cells (Yerevan) whose bases use standard LeCroy High Voltage (HV) distributed on SHV cables for each FEU-84 PMT channel and 1100 cells (Protvino) that use LeCroy HV augmented by Hewlett-Packard (HP) low-voltage (LV) booster supplies for the last 4 dynodes. The high voltage connections to the existing Yerevan bases use hypertronix connectors. This system requires a total of 7 LeCroy 1440 systems and 4 HP high-current LV supplies. While we can borrow the LeCroy and HP units (we believe, although we have not yet identified sources), the cost for cables and patch panels to implement this at RHIC will be nearly the same as the cost for replacing all the bases with Cocroft-Walton (CW) bases with computer-control. If we have to purchase LeCroy mainframes the cost will exceed the CW costs. The CW solution would be used at JLab when we return the detector, representing an overall savings for DOE.

These considerations have resulted in our plan to construct Cockcroft-Walton bases for the FEU-84.

The requirements on the CW system include:

- provide 1300-1800 V for 1700 FEU-84 PMTs having 12 dynodes each
- remote setting of HV values with 2 V sensitivity to match PMT gains in situ
- remote readout of set voltage value
- provide HV with better than 2
- less than 100 mW power consumption per base
- provide gain stability over operating range of 1 to 10^5 Hz or up to 100μA
- switching noise of < 0.25 pC in 100 ns gate
- fit into the ECal enclosure with room to allow cable access for HV and control
- total length for each base of < 15 cm
- provide 4' pigtails from each base for signal and control lines
- allow signal connection to BNC patch panel

Many version of CW bases have been designed for small photomultiplier tubes like the FEU84, including solutions at JLab [26] and at BNL. We have

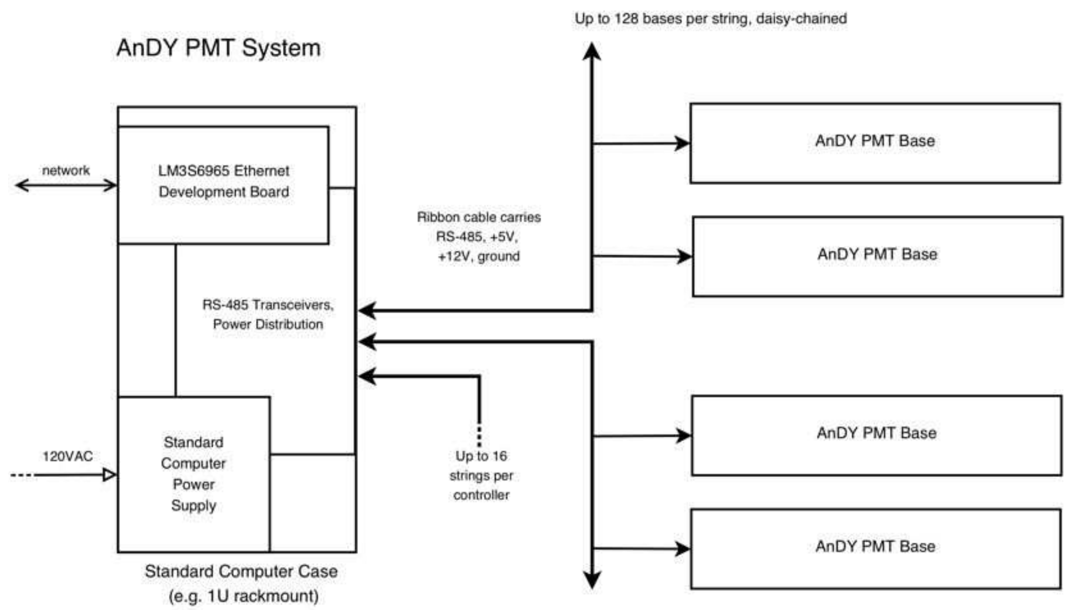

Figure 31: ECal PMT system diagram

borrowed heavily from these but intend to implement our solution with currently available much simplified computer control of the driving voltages. We do not need any elaborate electronics or control to check variation in PMT gain because our detectors all have individual LED fibers to provide continuous monitoring of PMT gain. We have used this LED-flasher system designed and fabricated by UCB/SSL for many years and have already produced the basic elements of the system.

Input power will come from a single standard computer power supply, 5V for electronics and 12 V to drive the diode pump. The ECal PMT HV system is shown schematically in Fig.31.

For ECal, a typical cell produces $\sim$500 kHz of 4 pC signals or 2A in minimum bias operation. A single pe at gain of 2×10^5 typical for an FEU84 operated at 1500 V produces 0.03 pC. Our calorimeter cells produce typically 1000 photoelectrons for 1 GeV of electron-equivalent energy loss, or 30pC/GeV. Operating at 1500V then our typical base will draw 3mW average power. A single bin can thus provide power for all of our PMTs.

Each base will accept input power and diode pump voltage from a 32 channel control board. The pump voltage will be controlled for each channel on the control board using a simple DAC. Communication with this board will be over RS-485 from a dedicated computer. We expect to produce 80 of these boards, using 54 for the ECal, 11 for PS, and 10 for HCal, although only the ECal will use our CW bases. The PS and HCAL use XP2972 PMTs with Nunnemaker bases and will use our control board only for controlling the driving voltage.

The CW base has been designed by Mike Ng at UCB/SSL. He will be responsible for both the CW base and the control system for it. We will produce 1800 of the bases, including sockets, 12-dynode HV supply, and 4' signal and control pigtails using commercial fabrication houses once we have shown that our prototype is acceptable.

3.4 ECal readout and triggering

The forward calorimeter projects we have been involved in over the past ten years at RHIC have employed a variety of readout electronics. First prototypes have used commercial gated analog-to-digital converters (ADC) and CAMAC readout (LeCroy 4300B) that remain readily available. These ADC cannot be gated at the RHIC clock frequency (9.38 MHz) due to the slow speed of the ADC. They require a fast trigger to open the ADC gates and delay lines for the individual phototube current pulses. This is not a good solution for A_NDY. The first flash ADC solution used for forward calorimeter projects was a 16-channel 8-bit ADC 9U VME board developed at Lawrence Berkeley Laboratory for fast triggering detectors at STAR. This is also not a good solution for A_NDY, since the 8-bit granularity is too coarse and this flash ADC board was notorious for high-frequency electronic noise. The issues with this flash ADC board were addressed in the QT design created at Berkeley/Space Sciences Laboratory. The QT board (see Fig.44) has proven to be a nearly ideal solution for calorimetry. It is a 32-channel 70 MHz flash ADC with 0.25 pC/count granularity housed on a 9U VME board. The noise levels are < 0.25 pC. Each 9U board consists of a mother board and four 8-channel daughter board. Signals are input to the device through 8-channel Positronix cable assemblies. Each daughter board has a field-programmable gate array (FPGA) to provide the first level of a digital trigger. The mother board also has an on-board FPGA to drive 32-bits of data on the backplane of the VME crate.

The proposed layout for ECal will require 50 total QT boards housed in four 9U VME crates (see Fig.48). Each left/right half of ECal will be readout by a rack containing two 9U VME crates that hold in total 25 QT boards within the two crates of each rack. A total of 25 twisted-pair ribbon cables will carry data from each rack from the on-board FPGA to the trigger crate for trigger decisions by the DSM. Separately, cat-5 cabling and optical fiber will be required for communication with the MVME 2306 processor in each crate. A twisted-pair clock line is required for each crate. Clock signals are distributed to the individual QT boards on the backplane of the 9U VME crate. 208 VAC lines will provide the estimated 20 kW of power to each rack. A chiller/radiator system is needed for each rack to provide cooling to the electronics. Care must be taken with this system, since the IP2 area is not climate controlled. Elevated dewpoints when the area heaters are off can cause condensation with potentially disasterous impact on the electronics.

A pair trigger on ECal is critical so that the 4kHz bandwidth of the DAQ system is not saturated by the 500 kHz interaction rate from colliding beams. The factor >100 reduction from interaction rate to DAQ rate can be easily accomplished with a pair trigger. The essential hardware for the trigger is a tree structure of field-programmable gate arrays, see Fig.47, although the full flexibility is limited by the availability of hardware. Each DSM board (Fig.45) has 128 bit input and either 16 or 32 bit output. A total of four DSM boards will allow 8 bits from each QT board to make a pair trigger. A natural mapping of the four DSM boards is then quadrants of ECal. Dilepton pairs of interest will have an average separation at ECal of 100 cm with 99% of the events where the electron and positron are in different quadrants. It will be necessary to check that the distance from the quadrant boundary is sufficiently large to ensure that the pair trigger is not flooded by lower mass events.

3.5 ECal monitoring

Online monitoring of all detector elements is done during all runs. The individual detector spectra can identify issues and monitoring software allows for rapid response to such issues. A precise determination of each detectors relative gain is provided by a light-emitting diode distribution system. A method that has worked very well for relative monitoring in the past is to employ a fast current pulse generator that drives a blue Nichia B500S light emitting diode (LED). Each LED is coupled to a light mixer and then to a bundle of 30 1-mm optical fibers. The optical fibers are then glued into a plexiglass panel that has a matrix of holes to match the matrix of the glass. Since this monitoring system is intended for relative gains, requirements on light uniformity and alignment of the fiber panel relative to the glass stack are not severe. Instead, the primary requirement is mechanical stability, so that once in place the light injection into the glass changes minimally with time.

We propose a similar monitoring system for the A_NDY ECal. This will require 50 current pulser boards, LED and light mixers. Each fiber mounting panel will inject light into a quadrant of ECal through 399 optical fibers bundled at one end and glued into the panel at the other end. Electronics to drive the TTL trigger for the current pulser boards is also required, as is a power distribution for the current pulse. The trigger to the current pulser boards needs to be synchronized with the clock to the QT boards, to assure that the current pulses from each PMT of ECal are phase locked to the QT gate. An earlier design for this trigger board exists and would need to be duplicated for the A_NDY ECal monitoring system. The trigger board is built around a commercially available FPGA board, packaged with standard TCP/IP communications. The FPGA distributes a prescaled clock pulse through buffer chips to the individual current pulser boards.

4 Hadron calorimeter (HCal)

A primary means of discriminating electrons from hadrons in A_NDY is the matching of clustered energy deposition in ECal with clustered energy deposition in HCal, positioned immediately behind ECal. There is a ∼50% probability that a hadron incident on ECal will begin its shower, as described in detail in Appendix 1. To facilitate cluster matching, it is a requirement that the transverse cluster size in HCal is kept as small as possible. This requirement is met by minimizing the longitudinal separation of ECal and HCal. The optimization of ECal to provide adequate acceptance for electron+positron pairs from Drell-Yan production necessitates an optimization of HCal, so that background rejection is preserved.

As described in Section 2, two 9-column × 12-row matrices of HCal detectors, originally built for AGS-E864, were staged at IP2. The optimization of the run-13 HCal requires modifications to HCal already staged at IP2. The basic scale of the optimized HCal is determined by the acceptance of ECal, as shown in Fig. 32.

A resulting $x - y$ view of the proposed HCal is shown in Fig. 33.

The integration of the 80 additional HCal detectors with the existing

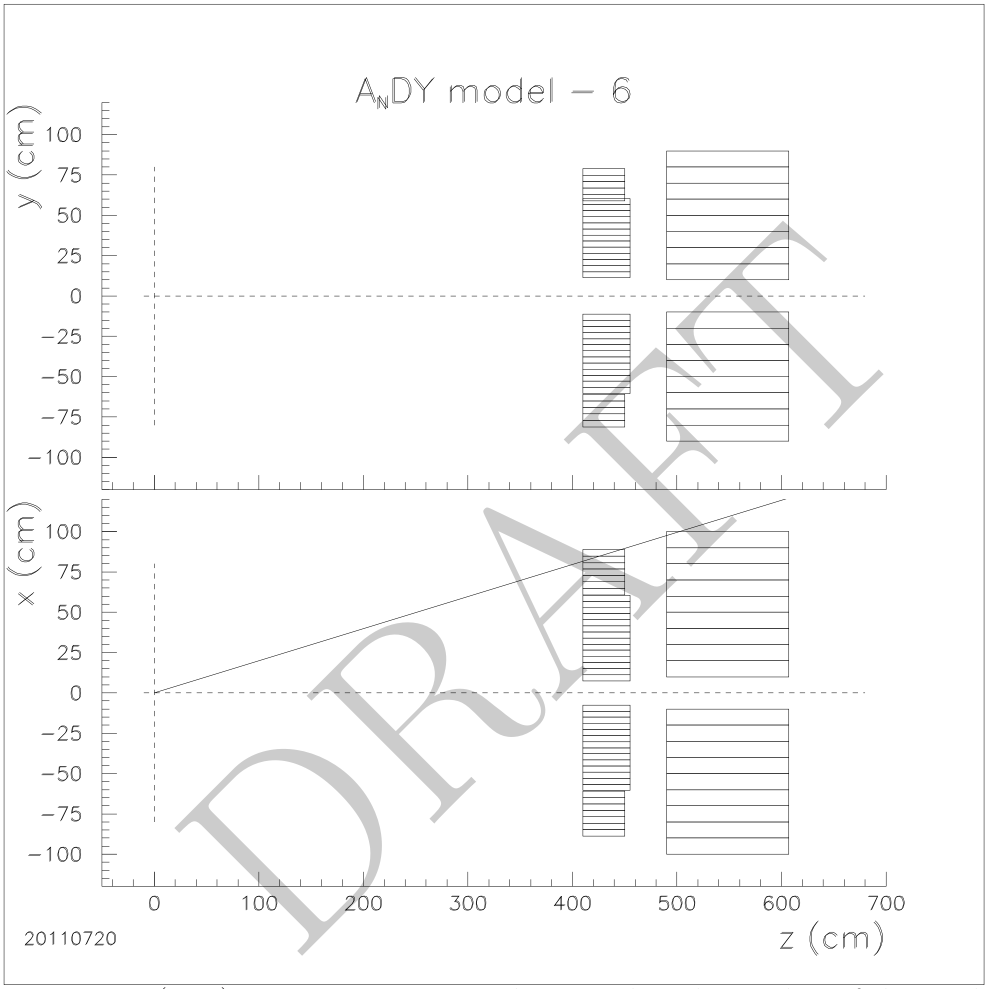

Figure 32: (Top) $y-z$ view at $x = 0$ showing the relationship of the model=6 ECal and HCal, reconfigured from its run-11 implementation. (Bottom) $x-z$ view at $y = 0$ showing the relationship of ECal and Hcal. These schematic views show only the lead-glass of ECal and the active portion of HCal.

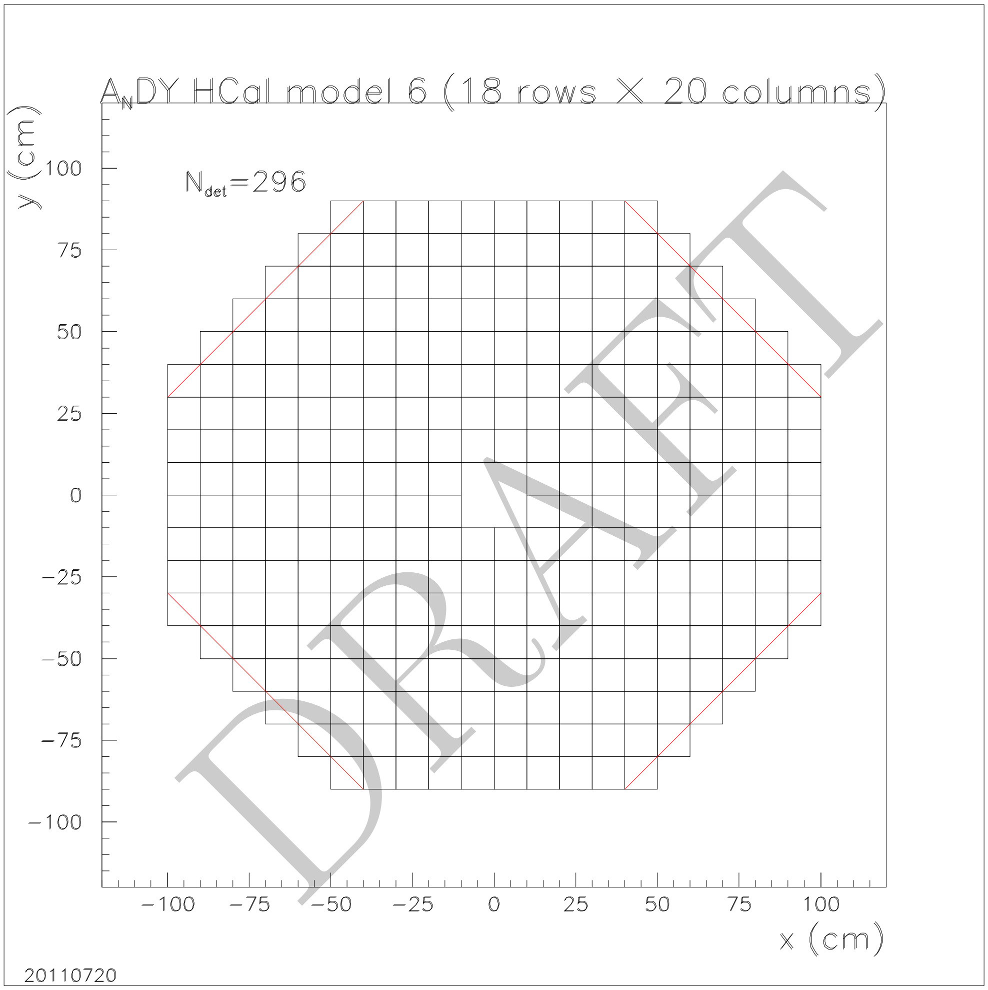

Figure 33: Schematic view of the proposed HCal as seen from the IP.

HCal modules can be done by:

- A rigging operation in which each HCal module is lifted off its support blocks and the support blocks are removed. The blocks are to be replaced by tracks used for the original design of the HCal modules. Replacement of the blocks by tracks will lower the existing HCal modules by 30 cm, corresponding to three rows of detectors.
- Six additional rows of detectors will get mounted onto the existing base plate, resulting in the 18-row HCal schematically shown in Fig. 33.
- A 2-column $\times$ 8-row submatrix of HCal detectors will be built between the two modules.
- An aluminum U channel will be supported from the bottom 2-column $\times$ 8-row submatrix. A 2-column$\times$ 8-row submatrix will be built atop this U channel support. FEA calculations show that the U channel provides sufficient strength to support this submatrix above the beam pipe, including a safety margin.
- A 20-column $\times$ 6-row backplate addition will get attached to the pair of existing 9-column $\times$ 12-row backplates. These backplates are required for mounting the photomultiplier tubes to the HCal detectors, and also form the light-tight enclosure for the HCal.

5 Preshower detector (PS)

The essential function of the A_NDY detector systems is to discriminate di-electron pairs from background. Particle identification is accomplished by characterizing the longitudinal and transverse shower profiles in each element of the apparatus. The first step in this characterization is to match clustered energy in HCal and ECal, and to match these clustered responses to the preshower response. The preshower refers to a system comprising two arrays of scintillator detectors (hereafter referred to as $PS_{1,i}$ and $PS_{2,i}$ where i refers to the segment number of the plane) that view the interactions with minimal intervening material, a planar converter of known thickness and uniformity and a final array of scintillator detectors ($PS_{3,i}$) after the converter. The two planes before the converter satisfy a hermiticity requirement, discussed

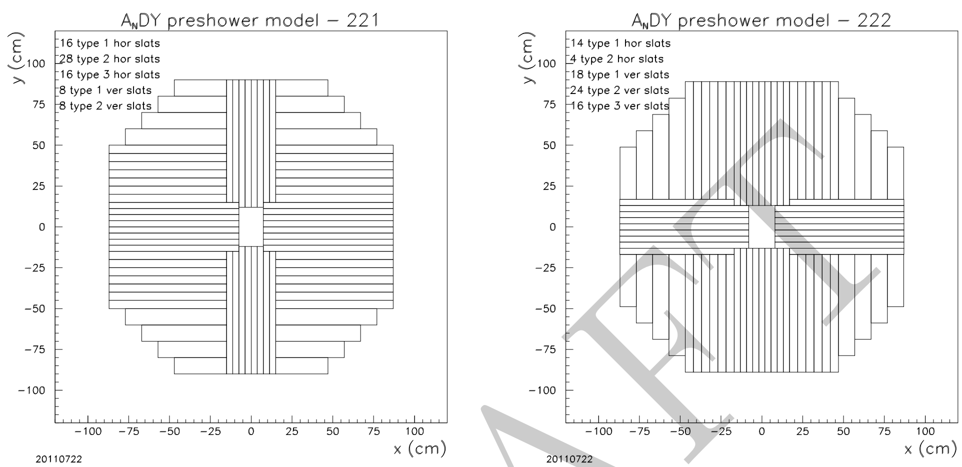

Figure 34: Proposed arrangement of preshower planes 1 (PS_1, left) and 2 (PS_2, right). Each plane consists of 76 total detectors each having thickness 0.5 cm of BC-408 (primary component anthracene). There are three different slat widths used to tile the full acceptance of ECal: 3.75 cm; 5.0 cm and 10.0 cm. The PS_1 and PS_2 planes are located at smaller z values then a lead converter plate. Two planes are required for hermiticity. Parallel strips in each plane are staggered by half a strip width to ensure that cracks between adjacent strips are not holes in the combined action of the two planes. Quadrant sections at larger distance from the beam overlap to form pixels between the two planes (see Fig. 35). A third plane of the same layout as PS_1 is located at larger z than a 0.5-cm converter plate. The hermiticity requirement is not as severe for the PS_3 plane since the converter most probably has initiated showers for electrons and positrons.

below. The design assumes that a valid hit in either or both of the first two planes of the preshower will suffice for particle identification.

A critical step in the particle identification is the matching between matched ECal and HCal clusters with the response of the preshower detectors that lie along the line between the clusters and the interaction point. An identified electron or positron will most likely have a single minimum ionizing particle (MIP) in $PS_{1,i}$ ($PS_{2,i}$) and a $PS_{3,i}$ response as given by multiple MIPs, an energetic cluster in ECal and little to no response in HCal. An identified photon will most likely have little to no $PS_{1,i}$ ($PS_{2,i}$) response and $PS_{3,i}$ response as given by multiple MIPs, an energetic cluster in ECal and little to no response in HCal. An identified charged hadron will most likely have a $PS_{1,i}$ ($PS_{2,i}$) and $PS_{3,i}$ response as given by a MIP, an energetic cluster in ECal and an energetic cluster in HCal. An identified neutral hadron will most likely have little to no $PS_{1,i}$ ($PS_{2,i}$) and $PS_{3,i}$ response, sometimes no response in ECal and sometimes an energetic cluster in ECal and an energetic cluster in HCal.

We have considered multiple geometries for the preshower. A robust construction method is a requirement. This sets constraints on geometries that can be realized. It is also a requirement that photostatistics do not limit the resolution of the detector. We look for > 50 photoelectrons for a minimum-ionizing particle (MIP) passing through the detector. Consequently, wave-length shifting fiber readout of pixilated preshower is not an option. The preshower is also required to be as uniform as possible so that robust modeling of it can be completed in simulation codes. The uniformity requirement rules out configurations where photomultiplier tubes are used within the preshower acceptance to, for example, collect light from segments at large pseudorapidity. The preshower, especially the plane(s) before the converter, must be highly efficient to ensure robust γ/electron/hadron discrimination. Inefficiencies are mostly related to gaps between adjacent detectors. Our design first minimizes gaps by the construction methodology and secondly involves two scintillator planes before the converter to allow staggering of gaps. A valid hit in a detector from either plane will work for identifying electrons and positrons from DY production. We do not plan to include the preshower in the trigger, so requirements on gain uniformity are not critical. Hardware level gain uniformity to within a factor of two will suffice. Gain spread larger than that would then face limitations from the 12-bit granularity of the analog-to-digital converters. Software corrections can be done offline to achieve the gain uniformity needed in the analysis, using well

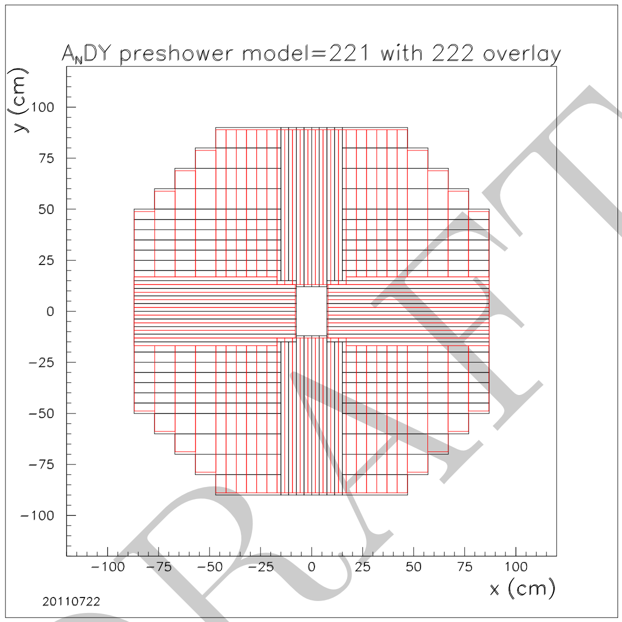

Figure 35: Overlay of the PS_1 and PS_2 scintillator preshower planes. Horizontal (vertical) strips near $y = 0$ ($x = 0$) are offset by one half strip width between the two planes. At larger $|x|$ and $|y|$ values the PS_1 and PS_2 strips are orthogonal to each other, effectively making pixels. It is assumed that good di-electron events will have hits from a single particle in either (or both) the PS_1 and PS_2 planes. This good hit requirement sets the requirement on detector granularity.

defined MIP peaks for calibration. In general, the preshower requirements are best met by a strip solution.

The matching of preshower, ECal and HCal response is complicated by the multiplicity of produced particles. When two particles interact with the same detector element the response of that element is confused. For example, there are two straight lines from the primary vertex to two ECal clusters with measured values (x_i, y_i, E_i). These two lines may intercept the same preshower detector $PS_{1,j}$. This preshower detector will provide the summed energy deposition of the two particles that produce the ECal clusters. A method of dealing with this complexity is to reject events when critical detector elements have multiple hits. The question then is impact of this rejection method on observing DY di-electrons.

Simulations have addressed the impact of multiple occupancy in the preshower strips on DY detection efficiency. These multiple occupancy estimates eliminate contributions from inner bremsstrahlung by merging closely spaced clusters in ECal, and account for the photon hits from inner bremsstrahlung that are nearby to the electron or positron as a single particle. Approximately 8% of DY events are lost when one or both lepton daughters intercept preshower detectors in both PS_1 and PS_2 that already have energy deposition from other particles. Approximately 89% of DY events will have singly-occupied PS_1 and PS_2 detectors for both the electron and positron thereby adding information to the particle identification.

The geometry proposed for the PS_1 and PS_2 planes of the preshower is shown in Fig. 34. These planes consist of vertical and horizontal slats. The scintillator thickness is assumed to be 0.5 cm of BC-408. A total of 152 strips from the two planes will be read out by 5 32-channel QT boards, leaving 8 spare channels. The detectors are readout by XP-2972 photomultiplier tubes at their ends distant from the beam. Each XP-2972 is powered by a Cockcroft-Walton base. The XP-2972 tubes and CW bases were purchased for AGS/E-864 and 400 sets have been loaned to A$_N$DY. Tests of these phototubes and bases are underway.

The PS_1 and PS_2 planes of the preshower will be followed by a sealed lead converter plate of thickness 0.5 cm (approximately 1 radiation length). Sealing of the lead will be accomplished by encasing it in adhesive-backed carbon fiber sheets. This encasing will then provide a robust means of mounting the converter in the preshower enclosure. We will work with a vendor to ensure their delivered product matches our flatness criteria and that the material composition will be quantified. Given the softness of lead, even when hardened by making an alloy with antimony, it is possible to flatten it upon receipt from a vendor. One radiation length is a tradeoff between initiating showers for incident electrons, positrons and photons versus not initiating hadronic showers for incident hadrons.

The sealed lead converter plates will be followed by a third plane of scintillator. The object of this plane is to detect particles from showers initiated in the lead. Finite shower sizes make this plane less prone to cracks compared to scintillator before the lead. Consequently, we will rely on construction methodology to minimize cracks between PS_3 detector elements. A glued construction will minimize cracks in any case. The geometry of PS_1 will be chosen for PS_3 (see Fig. 34). In total, the preshower will have 228 strip detectors and require 8 32-channel QT boards for readout. Connections between the preshower detectors and the QT boards will require 32 Positronix cable assemblies. The CW base has a K-lock connector for the co-axial signal. Short lengths of RG108 cabling with K-lock connectors at each end will connect the preshower detectors to a patch panel, built from K-lock/BNC bulkhead feedthroughs. K-lock/BNC bulkhead feedthroughs are also required for the H5010 photomultiplier tube assemblies. This will allow most of the cabling to use the much less expensive BNC connectors. A total of 8 low-voltage distribution boards will be required to power the 228 CW bases. Two low-voltage boards from the run-11 implementation will also be used.

Each distribution board serves 32 PMTs and has 2 - 16 channel control boards. The design of these boards is verey similar to the design of the ECal CW base controllers described above and shown in Fig.31.

We propose the construction of the preshower planes will be done in quadrants, since this corresponds to a manageable size. The construction method will involve wrapping individual strips by aluminized mylar reflectors and then gluing the wrapped strips to a mylar substrate. Two quadrants will be mounted inside a preshower enclosure boxes compactly positioned at smaller z than the ECal enclosure. An enclosure for the preshower will eliminate the need for wrapping the glued assembly with black tedlar that quite likely will make the materials in front of the scintillators non-uniform, thereby violating a requirement for the preshower. The preshower enclosure is separate from the ECal enclosure to ease the mechanical design requirements and to allow ECal to be moved away from the beam, thereby enabling HCal to view collisions through the preshower for at least calibration via $\pi^0 \to \gamma\gamma$, as per the method used in run 11 (Fig. 22). Mounting the preshower inside an enclosure will limit, but not preclude, access. The substrate will be painted black to limit the chance that photons from room lights would inject noise into the readout. We do require that noise levels are ∼0.25 pC (RMS) so that robust modeling of the detector can be done. The plan is to glue photomultiplier tubes to the scintillator strips for strips < 10 cm wide, or onto light guides for strips of 10-cm width. The glue joints would be reinforced by gluing aluminum L-brackets onto the scintillator near the optical couplings of the phototubes.

We estimate that the preshower assembly and testing can be completed in 6 weeks by two people, after the scintillator is delivered by the vendor. Experience from the run-11 A_NDY implementation is that 14 weeks elapsed from when a requisition was initiated to when the scintillator was delivered. Two weeks are estimated for wrapping and gluing strips into quadrant planes. Two weeks are estimated for gluing photomultiplier tubes onto the scintillators. Finally, two weeks are estimated for tests and installation.

6 Vertex detector (Midη)

An outstanding issue with the run-11 analysis that still needs to be resolved is a discrepancy between the calibration of the timing difference measurement and vertex-z. One method calibrates this by using single-beam backgrounds and the measured z-separation of the Yellow- and Blue-facing BBC. The other method uses the reconstructed z-vertex in the neutral pion mass reconstruction. These two methods disagree by ∼50%. Vertex-z plays a critical role for background suppression to access DY production through the matching of ECal and HCal clusters that require a line from the primary vertex and the matching to the preshower.

In addition, this detector is useful in identifying the type of interaction that produces the signals in the other detectors.

To assure a robust vertex-z calibration we propose to convert the 20-strip preshower detectors built for the run-11 A_NDY configuration into Midη detectors. These detectors would be arranged in two planes to form one module. There would be two such modules mirror symmetrically arrayed left and right of the beam to assess systematic errors in the vertex-z measurement. In total, 80 existing XP2972 and Cockcroft-Walton bases would be coupled to both ends of the existing 40 narrow strips from the run-11 preshower. There would be 80 channels of QT readout required for our proposed Midη

detector and cabling to connect from PMT to QT.

7 Forward Pion Detector (FPDY)

As mentioned in the introduction, theoretical understanding of our prior measurements and other world data is still evolving, although the theory community remains consistent regarding their prediction of a sign change for the analyzing power of Drell Yan production relative to measurements of transverse single spin asymmetries for semi-inclusive deep inelastic scattering. The A_NDY proponents believe it essential to close all possible theoretical loopholes. One such loophole is whether a completed A_NDY experiment robustly understands the sign of the analyzing power measured for DY production. To close this loophole, we propose to concurrently measure the sign of the analyzing power for neutral pion production at x_F values that overlap both the DY production measurement we will do and prior neutral pion analyzing power measurements we have completed [6]. That measurement will be done by a forward pion detector (FPD) identical to the run-11 A_NDY ECal implementation. The only difference is that we will mirror the left/right symmetric devices about the interaction point. This mirroring operation allows the run-13 A_NDY FPD to be positioned as far from the interaction point as possible (8.5m), thereby enabling a robust reconstruction of the neutral pion so as to measure its analyzing power to $x_F \sim 0.4$ (100 GeV neutral pions) without solely relying on identifying them through a deconvolution of highly overlapping showers in the lead glass.

The run-13 A_NDY FPD enclosures include a shower maximum detector that allows robust separation of single photon clusters from di-photon clusters produced by neutral pions when the electromagnetic showers from the latter are overlapping within lead glass detectors, based on prior experience [5]. A picture of one such A_NDY FPD module is shown in Fig. 36. All equipment used in the run-11 A_NDY ECal implementation will be reused for the run-13 A_NDY FPD. Unlike the transverse spin DY measurement, this really is an engineering measurement given our prior experience.

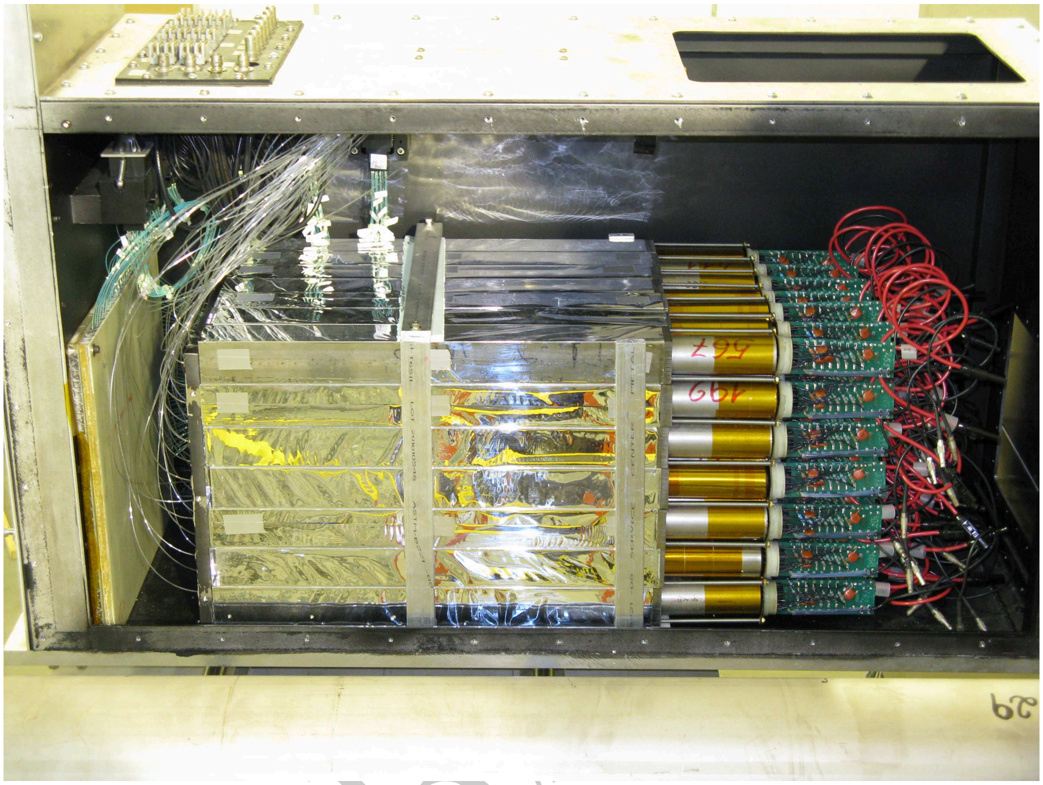

Figure 36: A picture of the run-11 A_NDY ECal before completion of its construction. This will become one module of the run-13 A_NDY FPD. The aluminum box at the far left houses a 7-element lead-glass preshower detector. Next to this box, within the primary calorimeter enclosure, are two planes of a scintillator-strip shower maximum detector. The wave-length shifting fibers are seen as green in this picture because the ambient light contains blue and ultraviolet wavelength photons. The next item seen are clear optical fibers that distribute light-emitting diode flashes to the lead glass for monitoring. A 7×7 stack of $40\text{mm}^2\times$ 40cm lead glass detectors is the primary element of the FPD. Its operation in run-11 produced the invariant mass distributions in Fig. 19. The combined analysis of the lead glass response and di-photon finding based on the shower maximum detector will permit robust neutral pion identification to 100 GeV, where the electromagnetic showers in the lead glass are highly overlapping and the matrix response alone cannot be used for robust neutral pion identification.

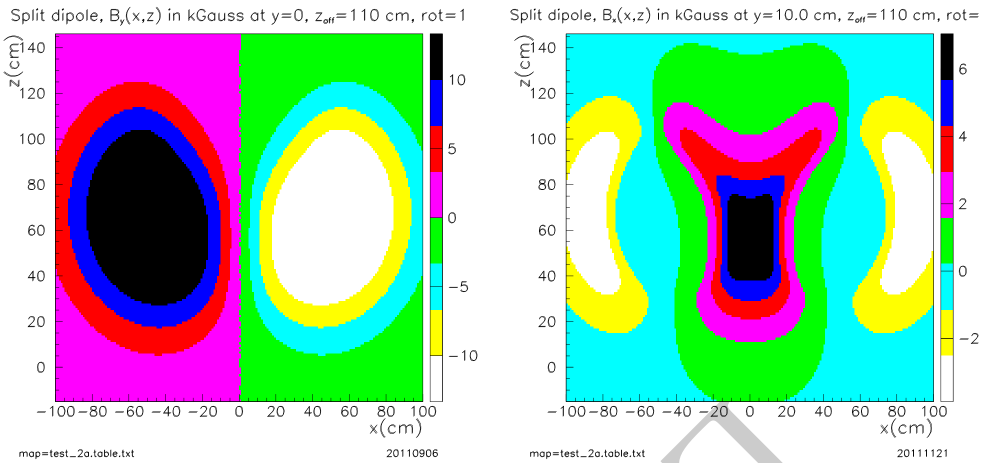

Figure 37: Calculated field map for the modified split-dipole magnet. The modification increases the gap between the poles from 15.7 to 31.4 cm.

8 Gas Electron Multiplier Tracking (TRK)

9 Run-14 magnet implementation

Our initial plan [2] was to install a split-dipole magnet, designed by the PHOBOS collaboration [15], and tracking chambers as the means of determining the sign of charged particles produced in the collision. Given the optimization to the ECal and HCal acceptance, the gap between the poletips for the split-dipole must get opened from 15.7 cm to 31.4 cm. As described in Sec. 8, there is an exciting development to instrument A$_N$DY with high resolution GEM tracking stations. Consequently, the section of the PAC proposal related to the magnet has been superceded by this section.

A new magnetic field calculation with this larger gap has been completed. The central field strength decreases as expected and there is a small increase in the fringe field. Figure 37 shows a map of $B_y(x, z)$ at $y = 0$ and $B_x(x, z)$ at $y = 10$ cm from a calculation with the poletip gap at 31.4 cm. As noted below, charged particles produced by collisions that are within the ECal acceptance are analyzed by both the x, y components of the magnetic field from the split dipole.

Tracking studies through the calculated field map have been completed similar to those done for the PAC proposal. These studies establish the $x - y$ loci of events from DY production at the z location of each of three tracking

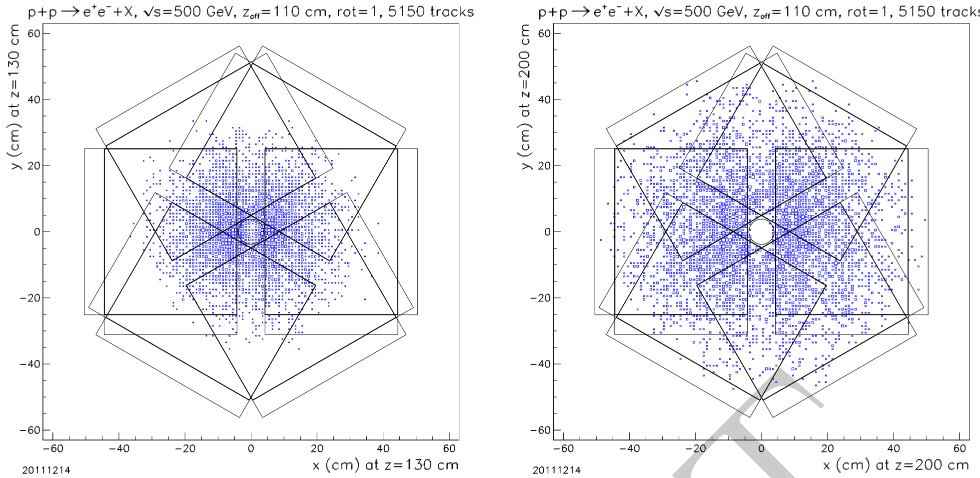

Figure 38: $x - y$ loci of points from DY production at the first two tracking stations. The GEM detectors are represented by the hexagonal tiling of a basic GEM module. Each GEM module is assumed to have two-sided electronics readout that is parallel to the active area of the detector.

stations. These loci impose the requirements on the transverse acceptance of the tracking stations at each z location. Figs. 38,39 show the $x - y$ loci for the proposed layout with the magnet at z_{off}=110 cm, the first tracking station at z_1=130 cm, the second tracking station at z_2=200 cm and the third tracking station at z_3=390 cm. The tracking studies are completed for e^+e^- pairs from Drell-Yan production that are within the acceptance of the ECal. In these studies, the vertex z location for each event is drawn at random from a Gaussian distribution with σ=30 cm. This diamond size has been projected by the Collider-Accelerator department for run 12 [16], and corresponds to optimizing the 9 MHz RF system used for accelerating the proton beams.

For completeness, the distribution of the z location that particles cross the beam pipe is shown in Fig. 40. This distribution is governed by the diamond size, with little impact from the magnetic field since the deflections due to the magnet are small.

Tracking studies through the split-dipole magnet gap opened to 31.4 cm have established deflections at each tracking station (Fig. 41). Deflection is the distance in the $x - y$ plane at the tracking station from the intercept of a straight line trajectory (zero field) to the intercept of the computed trajectory. Deflection crudely establishes the resolution requirements for each

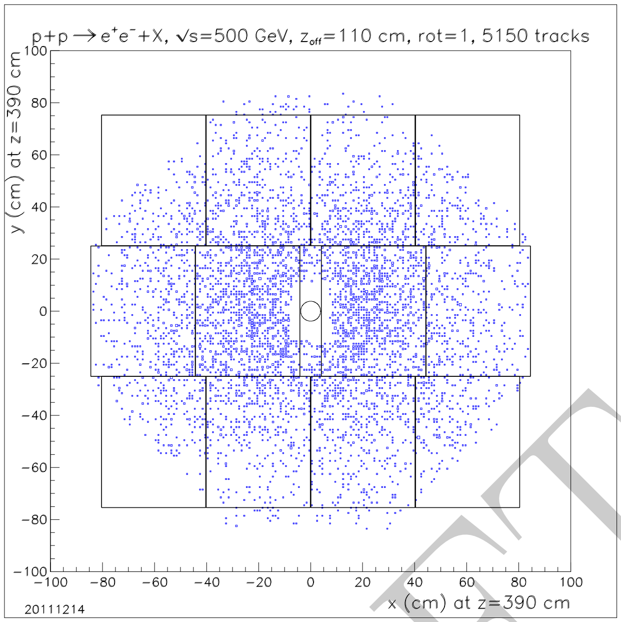

Figure 39: $x - y$ locus of points from DY production at the third tracking station. The GEM detectors are represented by a rectangular tiling of a basic GEM module. Each GEM module is assumed to have electronic readout boards that are perpendicular to the active area of the detector to enable close packing of the modules.

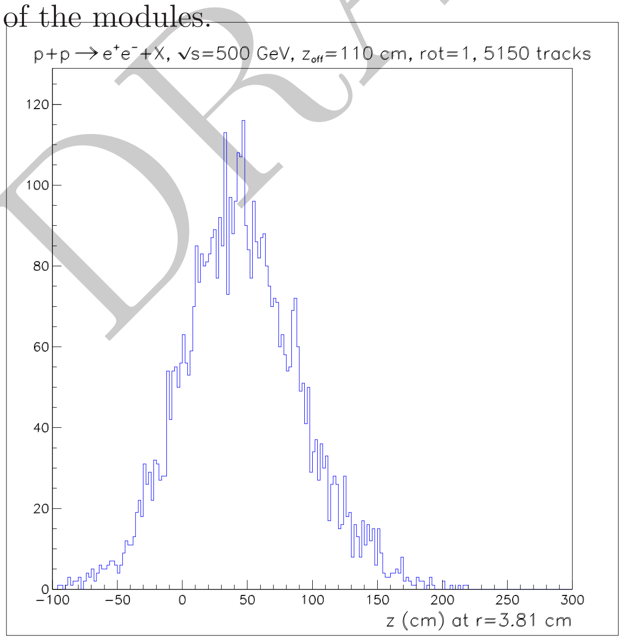

Figure 40: Distribution of the z location where DY daughters cross the beam pipe.

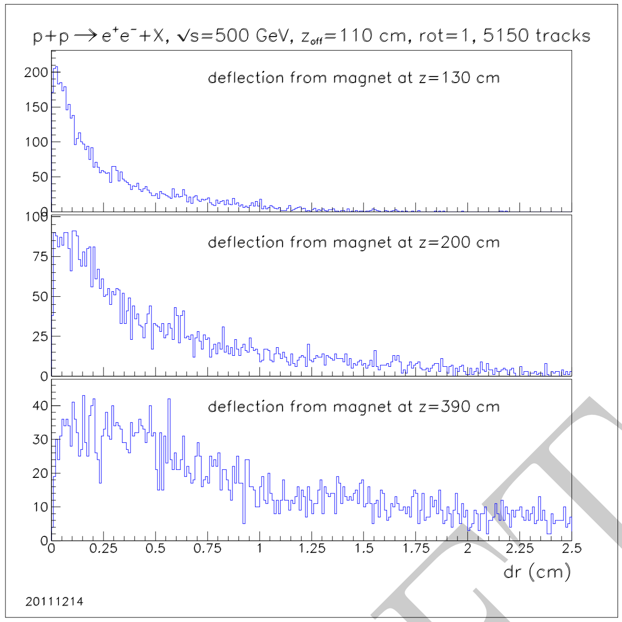

Figure 41: Distribution of deflections at each tracking station. Deflection is the distance in the $x - y$ plane of the tracking station between the field-free intercept and the full trajectory through the split-dipole.

tracking station. The distributions hide the correlations that provide the keys to track reconstruction. These correlations are described below. Suffice it to say that the deflection distributions are little changed by the increased gap between the poles of the split dipole.

The deflection distributions (Fig. 41) have been analyzed to understand how well the inclusion of the magnet will determine charge sign. This analysis has established that to a very good approximation, the deflections are radial, meaning there are both x and y components. This can be understood from the magnetic field map (Fig. 37), since the magnet effectively imposes an impulse (momentum change) with x, y components $\Delta p_y \sim p_z B_x(y)$ and $\Delta p_x \sim p_z B_y(x)$. Furthermore, the impulse is imparted in a spatial region between the interaction point and the tracking stations. A radial impulse is the intuitive expectation for a focussing element. Using the forward region of the split-dipole for momentum analysis results in the magnet acting primarily as a focussing element.

Given that the impulse is radial and the impulse is imparted between the origin of the particle production and the tracking station, it is then clear that charge sign discrimination is equivalent to the displacement between the

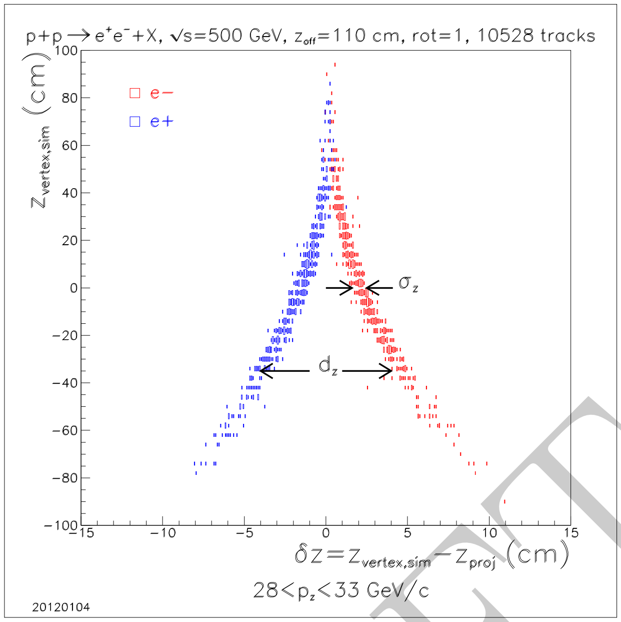

Figure 42: Correlation between the difference between z_{vertex} and the intercept of the fitted track with the beam line and z_{vertex}. Correlations for electrons and positrons are shown separately, to illustrate charge sign discrimination. The loci for each particle type results from the z_{vertex} dependence of radial impulses imparted by the split-dipole magnet.

true z position of the vertex and the point that results from extrapolation of a straight-line fit to the track back to the $x = 0, y = 0$ line (*i.e*, the z axis). To illustrate this, the x, y coordinates at each tracking station are determined from the tracking through the split-dipole field. Afterwards, these x, y coordinates are then smeared by Gaussian random numbers representing the finite resolution of the GEMs. The resulting x, y points are then fit by a linear least squares procedure, and the intercept with the z axis is found. The resulting analysis for a bin in longitudinal momentum for the electrons and positrons from DY production is shown in Fig. 42.

These tracking studies presently include multiple scattering through the beryllium and aluminum sections of the beam pipe, with the relevant material determined by the z position where the tracked particle reaches r=3.81 cm. Studies that include multiple scattering through the GEMs are underway. Full GEANT simulations have established that multiple scattering effects are dominated by crossing the beam pipe, in any case.

The impulses that give rise to the z displacement in Fig. 42 depend on

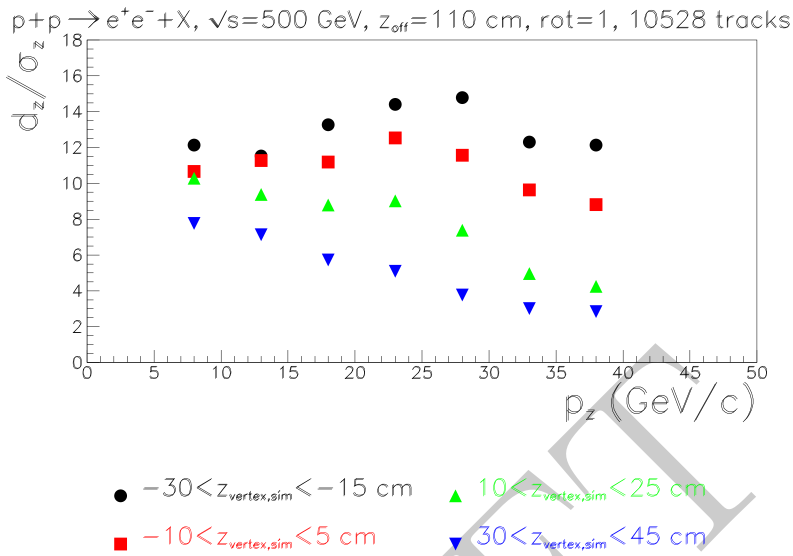

Figure 43: Analysis of Fig. 42 as a function of z_{vertex} and longitudinal momentum. The vertical axis of this plot is the significance of the charge sign discrimination, corresponding to the ratio of the separation for positive and negative charges (d_z) to the width (σ_z) of the distribution at fixed z_{vertex} and fixed momentum. The GEM tracking resolution provides signficant charge sign discrimination for all source points over the momentum range spanned by DY production.

longitudinal momentum and on the z_{vertex} for the event. The latter dependence should be expected from the field maps (Fig. 37), since the split dipole has essential zero field ($B_x \sim 0$ and $B_y \sim 0$) near $x = 0$ and $y = 0$. When the event vertex is far from the magnet, the dilepton opening angle allows the electrons and positrons to sample high field regions of the split dipole. When the event vertex is close to the magnet, the electrons and positrons see smaller field strenghts thereby resulting in smaller impulses.

A summary of the longitudinal momentum and z_{vertex} dependence of charge sign discrimination is given in Fig. 43. The vertical axis in this plot determines the *signficance* of the z separation between positive and negative charges. The significance is a ratio between the physical separation in z (at fixed p_z and the true event origin), scaled by the width of the distribution for electrons (positrons). For source points most distant from the magnet, the beam pipe crossing is most grazing. Consequently, multiple scattering effects in the beam pipe are the primary limitation in determining the significance (d_z/σ_z). Of course, these distant source points result in charged particles seeing the largest magnetic field strengths, so the significance of the charge sign measurement is large, but is found to be relatively independent of momentum. For source points closex to the magnet, the beam pipe crossing is less grazing. Consequently, space point resolution is the primary limitation in determining charge sign. This analysis demonstrates that significance $> 2\sigma_z$ can be achieved for the entire momentum range relevant for Drell Yan production, even for source points close to the magnet, when GEM resolution is available.

The role of the magnet is to go beyond inference to measurement. The importance of charge sign measurement, rather than inference, for DY may be critical to the success of A$_N$DY. The replacement of inference by measurement is believed to be of critical importance for required ancilliary measurements. For example, the heavy quark background to the dilepton production is presently understood within the context of a model (*i.e.*, PYTHIA). Potentially, intrinsic heavy quark components in the proton wave function will have very large impact on heavy quark production in the forward direction. Such contributions are not quantitatively modeled, so have not been assessed at this time. Measurements are required to distinguish DY production from dileptons from intrinsic heavy flavor components. Such measurements are possible in the b quark section by reconstruction of $B \to J/\psi K$ and by reconstruction of $\Lambda_b \to J/\psi\Lambda$. Known branching ratios can then be used to determine the background in the dilepton continuum from leptonic decays of heavy flavor. These ancilliary measurements will greatly benefit from charge sign discrimination.

10 Triggers and Data Acquisition

The A$_N$DY trigger and data acquisition systems are based on hardware and software developed for STAR [18]. The STAR trigger electronics was designed to be flexible and has morphed seamlessly into both a portable test system for board and detector testing and into the A$_N$DY trigger/DAQ system. The trigger uses a hardware decision tree based on QT boards (Fig.44), DSM boards (Fig.45), a Trigger Control Unit (TCU), and an internal control and data network using a copy of the STAR STP system (acronyms defined in Sec.10.1). The DSM and TCU at A$_N$DY consist of first generation STAR

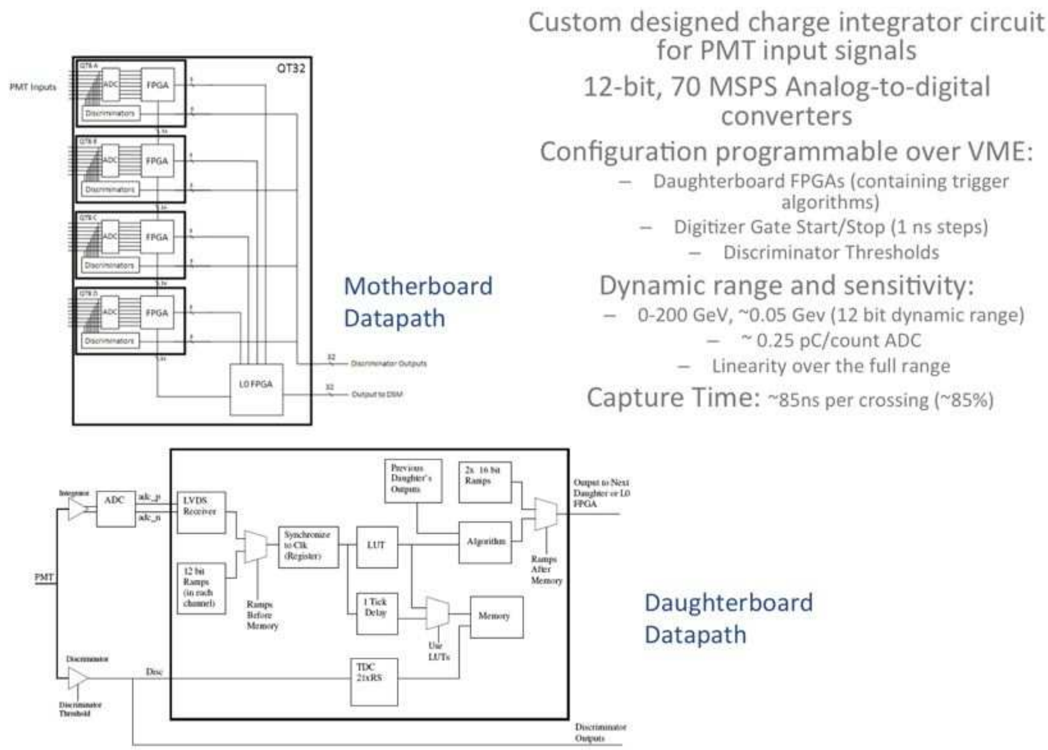

Figure 44: QT board details

hardware that has been superseded at STAR by newer versions that incorporate more powerful logic engines (FPGAs). The trigger needs for A_NDY are far simpler than the complex topological triggers used at STAR primarily because of the tightly focused physics goals of A_NDY.

A_NDY DAQ is a simple token-based readout scheme that is a natural extension of the hardware test routines used in STAR trigger development. Its operation is shown schematically in Fig.46. The A_NDY trigger/DAQ operates at rates exceeding 4 kHz and can take data at any time regardless of instantaneous luminosity. The upgrades from the run 11 to the run 13 configurations involve addition of more than 2k channels and 5 VME crates but involve only a few minor changes in software configuration files.

The A_NDY trigger uses minimum bias conditions based on the zero degree calorimeters and beam-beam counters as well as high-tower and cluster triggers combining various A_NDY FPDY, ECal and HCal modules. The A_NDY

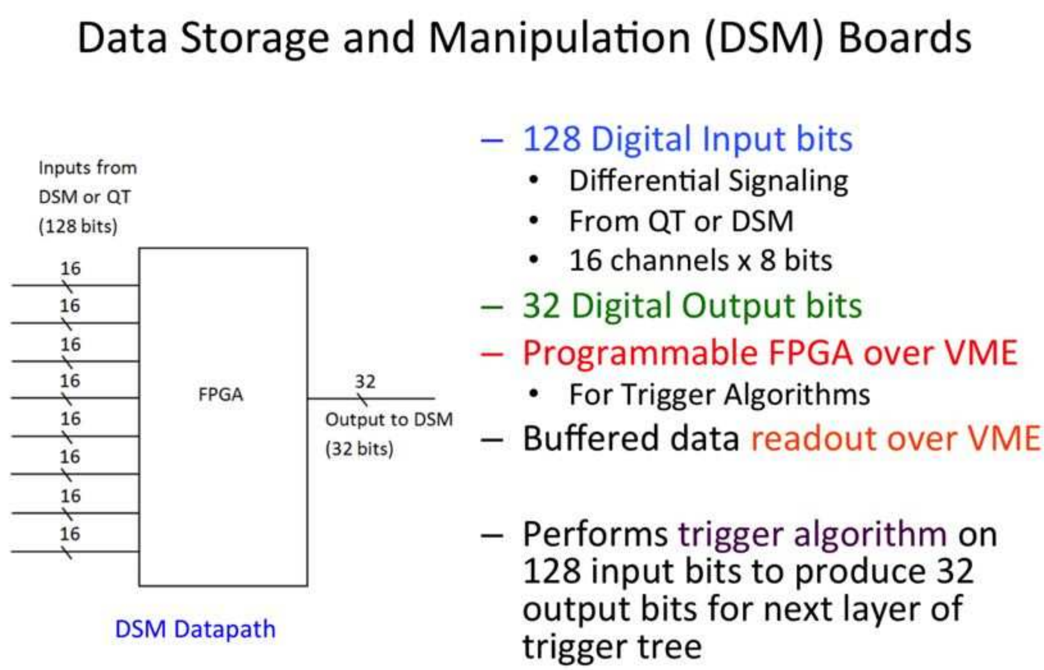

Figure 45: DSM board details

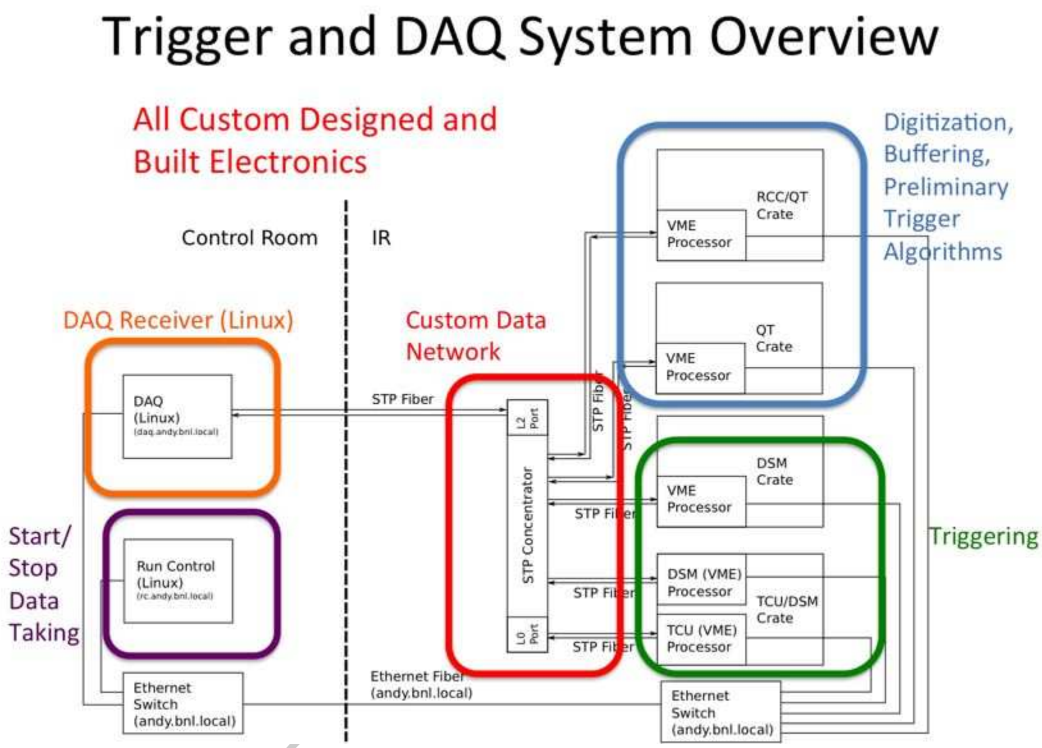

Figure 46: Schematic diagram of the trigger-daq system.

mid-rapidity array and preshower detectors are not involved in the trigger decision and are not connected to the decision tree. All detector systems use QT boards as their basic data input path; these board store 8B of data for each channel for 64k crossings in a cyclic memory. The QT boards also perform layer-0 logic manipulations as needed, such as finding the highest of the 32 channels of input ADC value (*e.g.* high tower), or summing input ADC values (*e.g.* cluster energy) and comparing to thresholds.

Up to 16 QT boards occupy a single 9U VME Crate as shown in Fig.48. QT boards for ZDC, BBC, FPD, ECal and HCal all have direct connections to send between 8 to 32 bits to a layer 1 DSM in the Level 1 crate. Each DSM board has connection to higher layer DSM boards in the L1 crate. For each RHIC crossing a trigger decision is made in the TCU based on combinations of up to 16 bits received from the last DSM board in the decision tree. There are no detector busy conditions at A_NDY; the only busy condition arises if the TCU runs out of tokens indicating that the downstream trigger/DAQ resources are not available. We measured the token FIFO empty in two independent ways during run 11.

The TCU places its decision bits on the VME backplane where it is shipped to the TCD for distribution to each detector VME crate for distribution on the local backplane. Receipt of a trigger within each DSM board initiates copying the appropriate 8B of data for each channel from the indicated crossing address into a FIFO for readout. A TCU register is polled by the Level1 CPU and, when a trigger is detected, the L1 CPU initiates a data gather operation by having the STP broadcast the crossing number and an organizing token to each VME CPU. Each VME Crate has an STP PCMCIA card in the local crate-control CPU which is connected to an STP concentrator board. The Concentrator accepts data from the crates in a push architecture and ships it in packets up to 4kB in length to the level 2 Linux CPU. When L2 has received all of the token-tagged data from each crate it packages this and ships it over a Glink fiber to the DAQ computer for monitoring and storage. From local storage the data is asynchronously shipped to HPSS for archiving.

Cosmic ray triggers are used to test and tune the system using signals from ECal, HCal, and cosmic-ray scintillator paddles placed to form tracks within the various detector modules. LED triggers are taken at a rate of ∼1 Hz to provide gain monitoring of all PS, ECal and HCal detectors. In run 13 A_NDY will operate with a small number of simultaneously active triggers to accept MB, HT, Esum, and cluster pair triggers.

The DAQ system is operated from a web-based interface using unix-command controls. It is responsible for starting and stopping the TCU. The TCU operates continuously at the RHIC crossing frequency of 9.4 MHz. The DAQ system communicates with the RCC board to issue run and stop commands. Expanding the system for run 13 will involve rebuilding a number of configuration files but will not entail architectural or significant code changes to the DAQ system.

10.1 Acronyms

- DSM: Data Storage and Manipulation: accepts 128 bits of input, passes the bits through an FPGA for logic decisions, and outputs up to 32 bits
- FPGA: Field Programmable Gate Array: the logic engine on each board
- TCU: Trigger Control Unit: accepts 16 "physics" input bits and up to 16 detector busy bits (not used in A_NDY) to make a trigger decision for each RHIC crossing
- TCD: Trigger-Clock Distribution: a 9U VME board connected to the output of the TCU to distribute token and crossing address to each of the detector VME Crates
- TAC: Time-to-Amplitude-Converters: These are 16 channel boards converting time from a leading edge discriminator to the next RHIC Strobe into a current signal for digitization.
- QT: 32 channel 9U VME charge and time digitizing boards
- STP: STAR Trigger Pusher : this is a latency-free high-speed local network hardware and software protocol
- PCMCIA: a hardware standard for plug-in boards into a VME CPU
- GLink: Giga-link: a 2 Gb/s transmitter/receiver board for fiber-based communication
- RCC: RHIC Clock and Control: a 9U VME board which provide the experiment clock and distributes this with the run/stop signal to all boards in the system

- HPSS: High Priority Storage System: The mass storage used at the RHIC Computer Facility where the data is analyzed.
- RS : RHIC Strobe: the 9.4 MHz RHIC clock, the rate at which beam bunches collide at the IP
- IP : Interaction Point: the point at which the Blue and Yellow beams collide. This is really a diamond of length $\sigma \sim 30\ cm$.

11 Simulations

12 A$_N$DY Computing

The computing needs for run-11 were met by employing a rack excessed by the Atlas collaboration in their recent computing upgrade. The excessed rack was moved to 1002D and the nodes were configured with Scientific Linux 5.5 after increasing the memory for each computer to 4 gigabytes. Condor was installed and provides 116 slots for batch processing. One node had its internal disk NFS mounted across the cluster to provide 240 gigabytes of shared space. Inexpensive, commercial USB drives provided 8 terabytes of data storage. Standard analysis and simulation programs are in routine operation on this cluster. Database daemons, a local web server and online monitoring and analysis codes were routinely operated on this cluster during RHIC run 11. To date, offline analysis has been conducted on this computing cluster. Although extremely powerful for the run-11 test, the computing cluster has limitations in processing, disk storage and vulnerability to heat, especially during the summer months. Computing is a requirement for the A$_N$DY project, as discussed below.

Analysis of the A$_N$DY data is the responsibility of individual members of the collaboration. Detector mapping and calibration files are shared among those doing the analysis. Physics results from A$_N$DY will require documentation of the analysis and archiving of all coding used for the analysis. Multiple frameworks are available for analysis packages and we have employed essentially all options in prior work. Analysis of raw data or existing simulations are expected to represent only 15% of the total computing requirements for A$_N$DY. Instead, GEANT simulations are expected to be the most CPU intensive work. Analysis of the run-11 implementation of A$_N$DY was developed

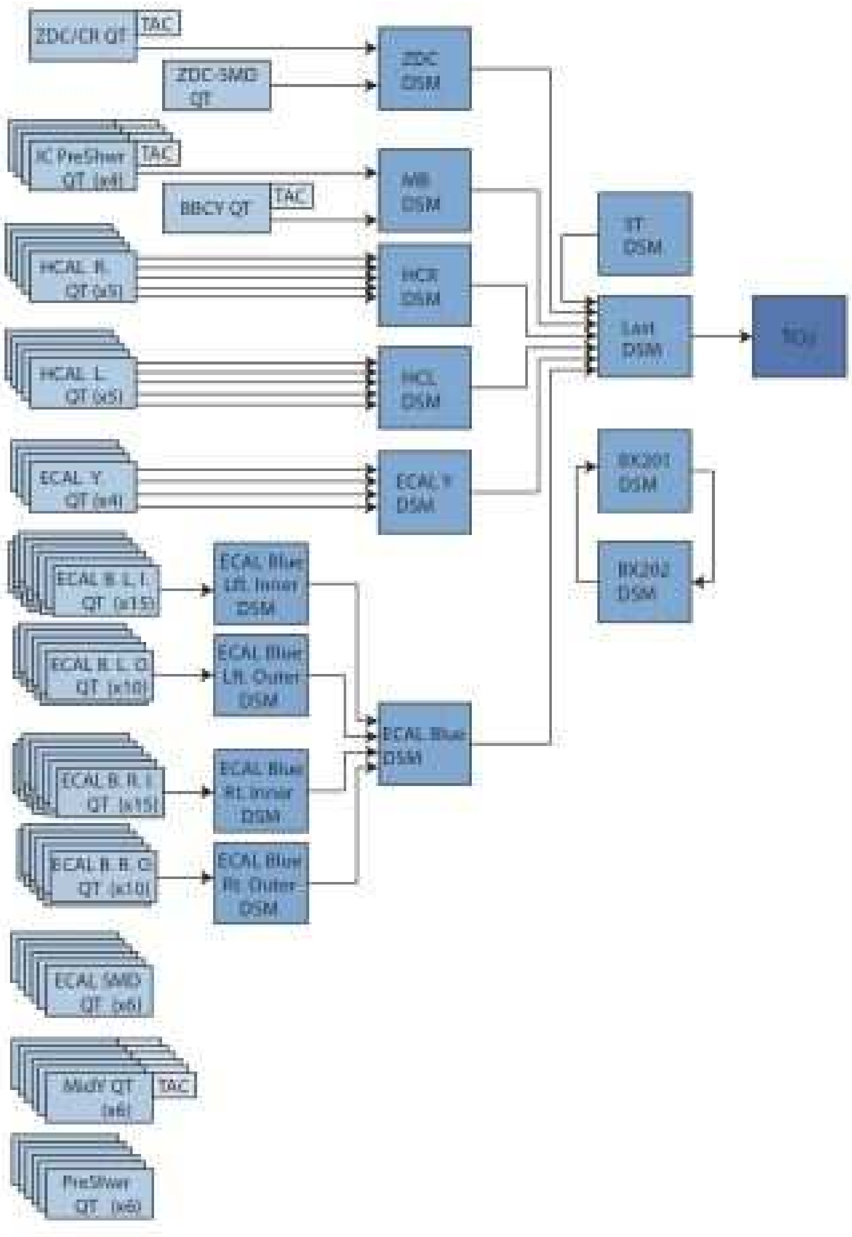

Figure 47: AnDY trigger decision tree for run13.

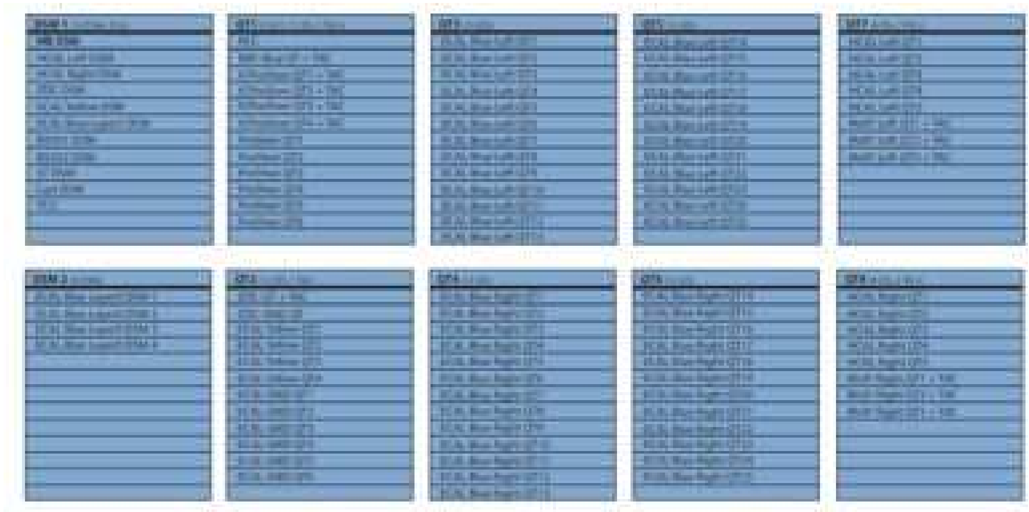

Figure 48: VME Crates for run13

on a 40M non-elastic, non-diffractive event sample, corresponding to $\sim 1nb^{-1}$ of data. This sample took 1 week of dedicated time on the 116-slot A_NDY cluster to generate through a GEANT model that accounts for all scintillating fibers within the run-11 HCal and requires 190 gigabytes of storage. At least two other event samples of comparable statistics await computing resources. They will employ filters on PYTHIA events (e.g., a jet filter and a large pair mass filter). The computing requirements for the run-13 A_NDY configuration are expected to be at least two orders of magnitude larger. A plan of how to meet the requirements awaits decisions at the RHIC/Atlas computing facility.

12.1 Near term computing needs

Immediate computing needs are cpu cycles for the analysis of the Run 11 data along with simulations incorporating the "as run" geometry required for the analysis, and space in HPSS for archiving the Run 11 data. Presumably the quickest way to obtain compute cycles with minimal impact on the resources of PHENIX and STAR is to reactivate some fraction of the 9 racks of PHENIX and STAR computers recently decommissioned. A new subnet can be obtained to isolate these machines from the PHENIX and STAR systems, and the standard operating system image can be reinstalled on the machines. There are clearly many factors which go into the decision as to what fraction of the decommissioned machines to reactivate, but, based on jobs run on recycled RCF machines in the A_NDY counting house, a minimum of two racks of machines with 4 GB of RAM is desired. If more machines can be made available, then the analysis can proceed faster.

Disk space is likely to be an issue in the short term. If sufficient centralized storage cannot be obtained to aid in the analysis and simulation of the Run 11 data, then the local disk on the reactivated compute nodes can be used both for local user file storage and for the Hadoop Distributed File System (HDFS). The latter will allow for efficient use of the distributed disk space on the farm nodes without requiring RACF manpower for the configuration or maintenance of the file system.

On the order of 4 Terabytes of HPSS storage is required for archiving the raw Run 11 data. The data is presently stored on consumer USB attached storage and a copy of the data should be made in HPSS as soon as possible to minimize the chance of losing the data. Analysis and simulation output should also get written into HPSS for archival purposes. The size of each of these outputs is expected to be comparable to the raw data set, so a total of 12 Terabytes of HPSS space is expected to be needed up to run 13. It is expected that new HPSS classes of service will be created for the raw and analyzed data.

12.2 Needs for run 13

Since data to be taken during run 13 will be written directly to HPSS, the optical fiber previously used by the BRAHMS experiments needs to be reactivated between the 1002D counting house and the RCF. Data will be transferred from the data acquisition system to HPSS at an estimated rate of 30 MB/s. An appropriately sized HPSS disk cache and sufficient tape drive resources need to be configured for the A_NDY classes of service to accommodate the data rate. The total raw data volume expected for run 13 is on the order of ∼200 Terabytes.

12.3 Long term needs

It is assumed that the A_NDY experiment will take data through run 14 and then continue to analyze data for another two years after run 14. It is further assumed that A_NDY will receive some fraction of the RCF allocation during these years and that current generation computers will be purchased for A_NDY so that the short term, reactivated compute nodes can be again retired. In addition, some amount of centralized storage needs to ramp up to facilitate the continued analysis of the data. NFS mounted central storage is probably sufficient for the needs of the experiment. The size of the centralized storage will depend on the allocation fraction for A_NDY.

As to the distributed disk on the compute nodes, it is not clear at this time if HDFS will continue to satisfy the needs of the experiment or if the need will arise to transition to an RCF managed distributed file system. The ultimate decision on the type of distributed file system, as with all of the computing infrastructure decisions for the experiment, will be made through active dialog with the computing facility staff.

13 Budget breakdown and resource-loaded timeline

Costs for staging A_NDY are driven primarily by electronics and cables for the various detectors and by installation of the magnet, although magnet costs need not be incurred prior to early 2014. There is at least 2 months of float in the schedule for preparing for run13 assuming that our funding is in place by 15 April 2012 and more than 4 months for run14. The resource-loaded timeline including cost and schedule are shown in Fig.49.

There are 7 detector systems in A_NDY in addition to the Zero Degree Calorimeters provided by CAD: the FPDY, BBCY, Midη, TRK, PS, ECal, and HCAL detectors. The FPDY is a Yellow-beam-facing π^0 detector consisting of 98 PbGl cells as used in the run11 tests. It must be moved to the other side of the IP but incurs no costs. It is essential because it incorprates a Shower Maximum Detector that allows us to cleanly measure the π^0 anisotropy for the $\sqrt{(s)} = 500GeV$ beams. The BBCY is already in place from run11 and needs no further work. The change in expected luminosity forced an acceptance-increasing redesign that leads to elimination of the Blue-facing BBC that was used in run 11. This places a requirement on the central portion of the PreShower detector to provide timing signals used in minimum bias triggers. The Midη detector is a scintillator hodoscope consisting of parts used in run11 augmented by TAC boards. The TRK is a set

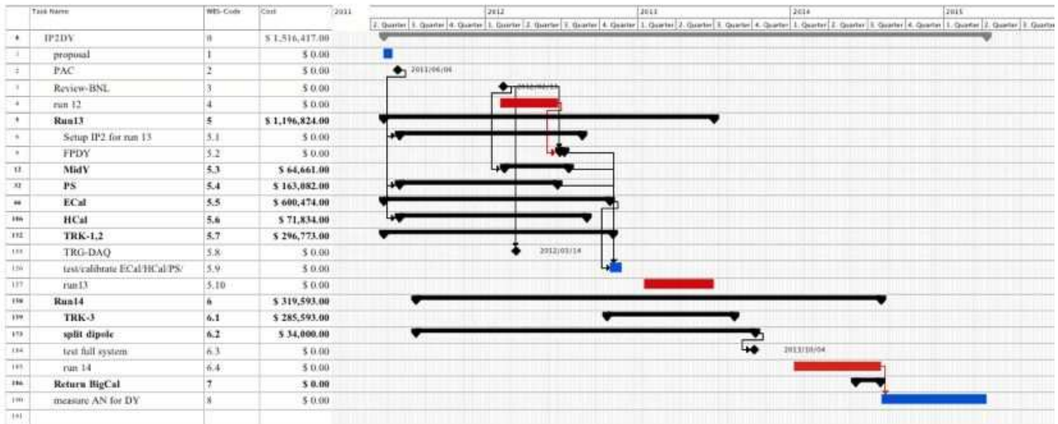

Figure 49: Resource loaded timeline.

of 3 new GEM arrays called stations 1, 2 and 3 to provide charged particle tracking useful for photon elimination, electron identification, and detector calibration. The PS is a new scintillator slat detector whose fabrication includes all electronics for the readout. This is essential for both photon and hadron suppression. The ECal consists of 1596 lead-glass (PbGl) cells borrowed from JLab and needs a high voltage (HV) system and readout electronics. The HCal is taken from AGS-E864 and needs an HV control system to allow remote setting of HV values and additional channels over what we used in run11 to better match the full ECal detector adcceptance.

The readout electronics for all of these detectors except TRK consists of QT boards (Fig.44) designed for STAR PMT readout. Fabrication of additional channels for A_NDY amounts to production of 70 additional boards and purchase of $\sim$ 300 Positronix 8-channel connectors with long pigtails. The QT fabrication is a standard production run, with organization taken care of by John Wolf and Jo Ann Bell at Berkeley. Total time from initial order to tested product delivery to BNL is 4 months, with most of that time taken in the actual production at the fabrication and loading firms. Cost and schedule are based on recent experience. We have over 100 of these boards in use at RHIC and have already informed our suppliers and fabricators of our intentions. Cost and delivery for the cables are based on quotes.

The Midη detector consists of two modules of two planes of scintillator slats each. The scintillator, PMTs, and electronics were used in our run11 test: the scintillator slats are simply rearranged for this application. This detector is used to determine z-vertex and mid-rapidity cluster multiplicity in coincidence with DY pairs. One module is placed on either side of the beam line to measure the z-vertex location for individual events. Each slat is 90cm $\times$ 2.5cm $\times$ 1cm viewed at both ends by an H5010 PMT with standard resistive bases fed from existing LeCroy High Voltage units. The module placement and plane separation are determined by diamond size. New mounting hardware and cabling must be provided for run 13. New TAC boards are needed to allow using time difference between PMTs on a single slat to give the plane 2-dimensional capability. This detector will be the responsibility of Xuan Li from Shandong University.

The TRK system consists of two stations of 6 GEM modules each and a third station consisting of 12 GEM modules. TRK1 and TRK2 provide tracks of the initial trajectories, while TRK3 sits just in front of PS to identify tracks entering ECal. Each module is $40x50$ cm^2 in area. The parts for the detector are purchased in large orders through BNL with assembly done at UVa. The electronics is purchased from CERN with the final readout stage provided by linux PCs.

The pre-shower detector consists of 228 scintillator slats of 3 different sizes as shown in Figure 34. The BC-408 equivalent scintillator is provided by Saint-Gobain cut and polished and ready for PMT mounting. The slats are similar to those used in run 11. Their cost is based on quotation from Saint-Gobain, with delivery specified as 6 weeks ARO. The slats will be viewed by XP2972 PMTs with Nunnemaker Cockroft-Walton bases that have been borrowed from Yale, originally used in AGS-E864. The PS detector will consist of 3 planes, two before a Pb converter and one following it. Each plane will be constructed in quadrants to facilitate mounting. The three planes will mount inside a preshower enclosure to simplify light-tight operation. This also minimizes material inhmogeneity thereby facilitating more accurate simulation of the A_NDY detector. The HV consists of a distribution system originally designed for Phenix with a new computer-control for the distribution designed by UCB/SSL for A_NDY. Fabrication of the PS detector slats and mounting will be taken care of by Gunar Schnell and Charles Folz. The HV distribution boards will be fabricated through BNL by Akio Ogawa. The control system will be designed by Mike Ng and fabricated through UCB/SSL.

The ECal detector consists of PbGl cells viewed by FEU-84 PMTs. The system as borrowed from JLab consists of FEU-84 PMTs with two different kinds of bases: 596 cells (Yerevan) have standard resistive bases, and 1000 cells (Protvino) have resistive bases with booster power applied to the last four dynodes. We intend to replace this hybrid HV system with CW bases for each PMT. This CW solution makes a simpler system which would then be used at JLab when the detector is returned. The CW design has been prototyped and tested. The bases will be fabricated in commercial firms with costs based on quotations and recent experience. The HV system will be taken care of by Jack Engelage and Michael Ng at UCB/SSL.

The ECal detector enclosure will be designed by Charles Folz and fabricated through BNL CAD. It will consist of two separate modules each mounted on Thompson bearings to allow them to move perpendicular to the beam line to facilitate access and enable operation close in the z direction to the HCal. It will include outer walls that are essentially covered with patch-panels for signals and for control. The QT readout electronics will mount very near this platform to allow Positronix connectors to go directly from the patch panels to the QT readout boards, thereby minimizing cable costs.

The HCal detector for A_NDY consists of two modules of 108 cells as used in run11 supplemented by 80 cells borrowed from Phenix to increase the acceptance and better match the ECal layout. The new cells will fill in the gap between the current 108-cell modules over and under the beam line, and will increase the vertical extent of the modules. Design and fabrication of the HCal housing and mechanical supports will be done by Charles Folz and CAD. Stacking the $\sim$200 lb cells in their new arrangement will be accomplished by CAD personnel.

The data acquisition (DAQ) system will be a simple extension of the existing DAQ used for run11. This consists of first-generation electronics originally developed for STAR supplemented by QT boards. Addition of 5 VME crates does not alter the architecture and is a simple change in operating parameters. The DAQ system is the responsibility of Chris Perkins and UCB/SSL. It is expected to take less than 1 month of effort.

The costs shown include all overheads and burdens as well as contingency. The contingency for mechanical components being provided by CAD are 40%. The contingencies for items for which we have new quotes is 5%. Other items carry 20% - 30% contingency depending on their basis of estimate. Standard overheads and other burdens are shown in Table 1.

Resources enter many points in the Gannt chart and the cost tables. The basis for cost of each item is shown in Fig.50

Project milestones are shown in Table 2.

type	overhead multiplier	notes
BNL machine shop	1.349	for enclosures, mounts
BNL Purchase $\leq \$25k$	1.525	
BNL Purchases $\geq \$25k$	1.093	
BNL University contracts	1.175	to UVa. and UCB/SSL
UVa labor	1.52	GEM assembly
UCB/SSL	1.17	first \$25k : 0 after

Table 1: Institutional cost burdens

14 Management plan

The A_NDY management structure is based on the expectation that all collaborators will be involved in all aspects of the experiment, from design and implementation of hardware through operation of the detector and analysis of the data. Individual subsystems will typically have a lead individual with different aspects of the subsystem taken by different individuals. Analysis software is based on shared calibration and mapping routines with analysis code developed by individuals and groups for specific goals. Multiple approaches to analysis lead to more robust results and greatly aid in understanding subtleties as well as in uncovering errors. For organizing details, the lead persons for different aspects of the project are show first below:

- Spokesman: Les Bland
- Project Manager: Hank Crawford and Elke Aschenauer
- IP2 Infrastructure: C. Folz, BNL
- Computing and Networks: T. Throwe, BNL; A. Ogawa, BNL; J. Engelage, UCB/SSL
- Trigger/DAQ: Chris Perkins, UCB/SSL
- Electronics: J. Engelage, UCB/SSL; E. Judd, UCB/SSL
- ZDCs: Angelika Drees, BNL
- Preshower: Gunar Schnell, U. Basque; G. Simatovic, Zagreb; G. Igo, UCLA

	Subsystem	item	milestone date	description
1	ECal	detector at BNL	20110728	all BigCal cells are brought to BNL from JLab
2	ECal	CW Base prototype	20120109	test of Cockroft-Walton base for FUE84 PMTs
3	PS	HV control prototype	20120209	test remote HV control for Nunnemaker base
4	DAQ	ready	20120314	daq ready for all tests and data
5	TRK	GEM module test	20120508	test 40x50 cm GEM at BNL
6	Midy	complete	20120702	detector for z-vertex ready
7	HCal	cells at IP2	20120723	move cells from Phenix to IP2
8	ECal-Y	complete	20120726	detector for π^0 w/ SMD ready
9	PS	complete	20120808	finish test of PS
10	HCal	complete	20120827	finish tests of HCal
11	ECal	complete	20120905	finish tests of ECal
12	MAG	split-dipole to IP2	20121002	magnet positioned at IP2
13	TRK	stations 1 and 2 complete	20121023	finish installation of stations 1 and 2
14	All	run13 system test	20121104	test of complete apparatus
15	MAG	complete	20120826	magnet installed and tested
14	TRK	station 3 complete	20130812	finish installation of station 3
15	All	run 14 system test	20131004	test of all systems
16	ECal	return to JLab	20120731	all cells, PMTs, bases to JLab

Table 2: AnDY project milestones

resource	base rate	overhead	local cost	contingency	Univ.contract	cost	BOE/notes
cable-control-CW	1.00	1.53	1.53	1.05	1.00	1.61	14-conductor cable, $50/100ft, IDC connectors, 50 cents in quantity.
cable-control-N	15.00	1.53	22.95	1.05	1.00	24.10	
cable-RG58-bnc-bnc	18.00	1.53	27.54	1.05	1.00	28.92	KC quote
cable-positronix	75.00	1.53	114.75	1.05	1.00	120.49	KC quote
cable-positronix-k	147.00	1.53	224.91	1.05	1.00	236.16	KC quote
cable-patch-panel	950.00	1.53	1453.50	1.05	1.00	1526.18	digikey parts $5.63 ea; 128/panel; 2 hr. BNL shop w/ burden @173/hr
cable-patch-panel-k-bnc	2115.00	1.53	3235.95	1.05	1.00	3397.75	digikey part $25; 80/panel; (80*25*1.53+2*173)*1.05=3400
CW-control	500.00	1.17	585.00	1.30	1.17	889.79	recent build; each controls 128 bases
CW_bds	4.00	1.17	4.68	1.20	1.17	6.57	prototype build
CW-proto	5000.00	1.17	5850.00	1.20	1.17	8213.40	prototype cost - engineering
CW_parts	30.00	1.17	35.10	1.30	1.17	53.39	prototype cost
CW-Base	65.00	1.17	76.05	1.20	1.17	106.77	prototype cost
CW_ld	25.00	1.17	29.25	1.20	1.17	41.07	prototype costs
GEMreadoutbds	2200.00	1.09	2398.00	1.05	1.00	2517.90	CERN quote; large purchase thru BNL
GEM-FEE	3.00	1.09	3.27	1.05	1.00	3.43	Uva recent fab; large purchase whtu BNL
GEMfoils	1200.00	1.09	1308.00	1.05	1.00	1373.40	Uva recent fab; large purchase thru BNL
GEMframes	2600.00	1.09	2834.00	1.05	1.00	2975.70	Uva recent fab; large purchase thru BNL
GEMsupplies	1000.00	1.00	1000.00	1.05	1.17	1228.50	Uva recent fab
GEMsupport	2500.00	1.00	2500.00	1.05	1.17	3071.25	Uva recent fab
GEMassy	2000.00	1.53	3060.00	1.05	1.17	3759.21	Uva grad student, recent fab
GEMassy2	4000.00	1.53	6120.00	1.05	1.17	7518.42	Uva tech, recent fab
GEMgas	5000.00	1.00	5000.00	1.05	1.17	6142.50	Uva recent fab
GEMevtblders	1000.00	1.53	1530.00	1.05	1.00	1606.50	recent purchase
flashers	50.00	1.17	58.50	1.05	1.17	71.87	recent fab
mech	1000.00	1.00	1000.00	1.00	1.00	1000.00	generic unit
Pb	1000.00	1.53	1530.00	1.05	1.00	1606.50	recent purchase
PMT-XP2972	0.00		0.00			0.00	borrowed from Yale
PMT-H5010	0.00		0.00			0.00	from AGS E896
Base-N	0.00		0.00			0.00	from Yale
HV-N-Control	100.00	1.17	117.00	1.20	1.17	164.27	estimate from similar fab
HV-N-proto	3000.00	1.17	3510.00	1.20	1.17	4928.04	estimate from similar fab
HV-N-Dist	347.00	1.17	405.99	1.05	1.17	498.76	recent fab
QT32-ld	100.00	1.17	117.00	1.05	1.17	143.73	recent fab
QT32-bd	182.00	1.17	212.94	1.05	1.17	261.60	recent fab
QT32-pts	400.00	1.17	468.00	1.05	1.17	574.94	recent fab
QT8-bd	55.00	1.17	64.35	1.05	1.17	79.05	recent fab
QT8-pts	585.00	1.17	684.45	1.05	1.17	840.85	recent fab
QT8-ld	100.00	1.17	117.00	1.05	1.17	143.73	recent fab
QTBOC	264.00	1.17	308.88	1.05	1.17	379.46	recent fab
QTTAC-adapter	528.00	1.17	617.76	1.05	1.17	758.92	recent fab
scint	14524.00	1.53	22221.72	1.05	1.00	23332.81	St. Gobain quote
STP	667.00	1.17	780.39	1.05	1.17	958.71	recent fab
tac-bd	1957.00	1.17	2289.69	1.05	1.17	2812.88	recent fab
VME-QT	700.00	1.17	819.00	1.05	1.17	1006.14	recent backplane purchase

Figure 50: Resource rates including BOE.

- ECal: C. Perdrisat, College of William and Mary; E. Brash, TJNAF
- HCal: A. Ogawa, BNL
- Midη: X. Li, Shandong
- FPD: L. Nogach, Protvino; N. Minaev, Protvino
- GEMs: N.Lyanage, K.Gnonvo, UVa.
- Magnet: W.Meng, C.Folz, BNL

Regarding memoranda of understanding (MOUs), we would seek to establish such documents as needed to aid our collaborators in their negotiations with their home institutions.

The lead institution for each detector is shown in Table 3.

Institutional responsibilities cover different aspects of each detector as shown in Table 4.

The FTE level of commitment for each member of A$_N$DY is shown in Table 5.

detector	institution	note
BBC	BNL	existing
Midη	BNL/SU	existing scints and PMTs
FPDY	IHEP	existing
PS	Ikerbasque	all new
ECal	CWM/BNL	existing cels and PMTs
HCal	BNL	existing cells and PMTs
TRK	UVa	new GEM system

Table 3: Lead Institutions for Detectors

14.1 Key Performance Parameters (KPP)

We identify the following performance requirements for successful completion of the Drell-Yan A_N measurement:

1. ECal energy resolution: Calibration and resolution of each cell must be measured. Current cells provide $\sigma E/E \leq 15\%/\sqrt{E}$; mass resolution and signal/noise depend critically on knowing these.

2. ECal Cockroft-Walton base operation: The bases must provide remotely settable High Voltage between $1300 - 1700$ V with 12-bit accuracy. This is to allow gain matching of ECal FEU84 PMTs.

3. HCal and PS Nunnemaker base HV control: The HV-N controllers must provide remotely settable High Voltage between $1300 - 1700$ V with 12-bit accuracy. This is to allow gain matching for the XP2972 PMTs on Hcal and PS which have Nunnemaker bases.

4. PS resolution: Each preshower slat must have charge resolution sufficient to resolve individual minimum ionizing particles (MIP) for 1, 2, 3 or more hits. This is essential to resolve single particles from early showers.

5. PS efficiency: Each slat must have efficiency $\geq 98\%$ for single MIPs. This is essential for photon rejection.

mechanical			
	HCal	cells	BNL
		enclosure	BNL
	ECal	cells	UWM
		enclosure	BNL
	PS	cells	Ikerbasque
		enclosure	BNL
	TRK	GEM modules	UVa
		enclosures	BNL
	Midη	cells and mount	BNL
	FPDY	mount	BNL
Electronics			
	HCal	HV, QT, RO	UCB/SSL
	ECal	HV, QT, RO	UCB/SSL
	PS	HV, QT, RO	UCB/SSL
	TRK	HV	UVa
		FEE, RO	BNL
	BBC	HV	BNL
		QT, RO	UCB/SSL
	FPDY	HV	BNL
		QT, RO	UCB/SSL
	TRG/DAQ	DSM, TCU	UCB/SSL
Integration			
	installation	all	BNL
	operation	all	BNL, UCB/SSL
Software			
	data storage		BNL
	simulation		BNL, UCB/SSL
	Online		UCB/SSL
	Offline		BNL
	Analysis	TRK	UVa, BNL
		Calibration	IHEP, BNL, UVa
		J/Ψ, Υ	UCB/SSL, SUNYSB
		open charm	
		Λ_c	

Table 4: Institutional responsibilities

Support	Institution	Person	FY12	FY13	FY14	FY15
DOE	BNL	Aschenauer				
DOE	BNL	Bazilevsky				
DOE	BNL	Bland	0.95	0.95	0.95	0.95
DOE	BNL	Drees	0.15	0.15	0.15	0.15
DOE	BNL	Eyser	0.25	0.25	0.25	0.25
DOE	BNL	Folz	0.25	0.25	0.25	0.25
DOE	BNL	Makdisi	0.2	0.2	0.2	0.2
DOE	BNL	Ogawa	0.9	0.9	0.9	0.7
DOE	BNL	Pile	0.15	0.15	0.15	0.15
DOE	BNL	Throwe	0.2	0.2	0.2	0.2
DOE	BNL/SHandong	Li	0.5			
	IHEP	Minaev	0.2	0.2	0.2	0.2
	IHEP	Nogach	0.5	0.5	0.5	0.5
EHU	Ikerbasque	Schnell	0.4	0.4	0.4	0.4
EHU	Ikerbasque	Van Hulse	0.25	0.25	0.25	0.25
	IU	Vossen				
DOE	LANL	Liu	0.1	0.1	0.1	0.1
NSF	NCU	Brash	0.1	0.1	0.1	0.1
NSF	NCU	Martin	0.5	0.5	0.5	0.5
NSF	NSU	Punjabi	0.1	0.1	0.1	0.1
	TJNF	Avakian				
DOE	UCB/SSL	Crawford	0.5	0.5	0.5	0.5
DOE	UCB/SSL	Engelage	0.25	0.25	0.25	0.25
DOE	UCB/SSL	Judd	0.1	0.1	0.1	0.1
DOE	UCB/SSL	Perkins	0.25	0.25	0.25	0.25
	UCLA	Igo				
DOE	UVa	Lyanage	0.1	0.1	0.1	0.1
DOE	UVa	Gnonvo	0.1	0.1	0.1	0.1
NSF	W&M	Perdrisat	0.1	0.1	0.1	0.1
	Yerevan	Abrahamyan				
	Yerevan	Shahinyan				
	Zagreb	Planinic	0.2	0.2	0.2	0.2
	Zagreb	Simatovic	0.5	0.5	0.5	0.5

Table 5: Individual FTE commitments to AnDY

6. GEM charge resolution: Single Mips must be distinguishable in individual GEM modules. This is essential for distinguishing single particles from photon-conversion pairs.

7. GEM position resolution: Each GEM module must have single particle position resolution of $\leq 500\mu$. This is essential for tracking individual electrons into the ECal cells.

8. GEM efficiency: Each GEM module must provide $\geq 90\%$ efficiency for detecting a MIP. This is essential so that pairs of modules provide $\geq 99\%$ rejection power for photons.

9. FPDY resolution FPDY must resolve π^0 up to $x_F \sim 0.4$. Need to cover the kinematics of DY and of our prior π^0 measurements.

10. DAQ rates: The A_NDY data acquisition system must select, collect and store data at rates $\geq 2kHz$. Our signal rate is $\sim 0.005Hz$. We know from run11 that we must reject $\sim 10^5$ high-tower ECal triggers for each e^+e^- reconstructed: these occur a an average rate $\sim 500Hz$. We need higher daq rates to provide the minimum bias events needed for calibration and to allow flexibility in threshold selection for the high-tower or energy sum triggers.

11. Dead time $\leq 10\%$ We need to sample full delivered luminosity. Thus our dead-time must be small.

12. Magnet stablity: The field must be stable to $\leq 2\%$ Bdl fluctuations over the course of the run. We measure charge sign by deflection at TRK-3, and a 2% change in Bdl will lead to an $\sim 0.3mm$ shift at TRK-3, while the deflections of typical DY electrons is $\sim mm$ at TRK-3.

13. MidY Interaction z vertex: measured to $\leq 5cm$. The uncertainty in reconstructed mass scales directly with the uncertainty in vertex location - $dM \sim dz/z$.

14. Diamond size: Small diamond is best. The mass resolution depends on knowing the vertex location, and our ability to measure deflection depends directly on diamond size.

15. RHIC backgrounds: Beams must be tuned to have $\leq 10kHz$ of single beam backgrounds at IP2.

16. RHIC Luminosity and Polarization: Average $\geq 10pb^{-1}/week$ with $\geq 50\%$ polarization delivered to IP2. Our goal is to measure A_N to better than 2% accuracy, implying a signal of $\geq 10^4$ reconstructed pairs, approximately half at each transverse polarity, which requires $100pb^{-1}$ delivered with polarization $\geq 50\%$.

15 Safety

A workplan has been established for the run-11 A$_N$DY effort (appendix 2). It is a requirement that work to be done is understood and planned before it is actually completed, to assure that it is completed safely. All components of the proposed implementation at IP2 will be reviewed by the RHIC safety committee. Action items from these reviews will be promptly resolved. It is anticipated that the actual implementation will be subject to unannounced inspections. Safety awareness is the primary consideration in prior work done for forward calorimeter projects. This awareness is continually renewed during weekly and daily planning meetings. The weekly meetings set broad goals. The daily meetings are specific to the task at hand and assure communication between those who will do the work.

References

[1] J. C. Collins, Phys. Lett. B**536** (2002) 43.

[2] *Feasibility Test of Large Rapidity Drell Yan Production at RHIC*, E. C. Aschenauer *et al.*, Letter of Intent to 2010 BNL Program Advisory Committee.

[3] A. Airapetian *et al.* (HERMES), Phys. Rev. Lett. **103** (2009) 152002.

[4] F. Bradamante (for COMPASS), invited talk at *3rd International Workshop on Transverse Polarization Phenomena in Hard Scattering* (2011) [arXiv:1111.0869].

[5] J. Adams *et al.* (STAR), Phys. Rev. Lett. **92** (2004) 171801.

[6] B. I. Abelev *et al.* (STAR), Phys. Rev. Lett. **101** (2008) 222001.

[7] J. Adams *et al.* (STAR), Phys. Rev. Lett. **97** (2006) 152302.

[8] S. J. Brodsky, D. S. Hwang and I. Schmidt, Phys. Lett. B**530** (2002) 99.

[9] Zhong-Bo Kang, Jian-Wei Qiu, W. Vogelsang, F. Yuan, Phys. Rev. D**83** (2011) 094001.

[10] J. Qiu, G. Sterman, Phys. Rev. D**59** (1998) 014004.

[11] D. Boer, Phys. Lett. B**702** (2011) 242.

[12] A. Prokudin and Z. B. Kang, contribution to *Worskhop on Opportunities for Drell-Yan Production at RHIC* (BNL, 2011).

[13] T. A. Armstrong *et al.*, Nucl. Inst. Meth. A **406** (1998) 227.

[14] A. J. R. Puckett *et al.*, Phys. Rev. Lett. **104** (2010) 242301.

[15] R. Bindel, E. Garcia, A. C. Mignerey, L. P. Remsberg, Nucl. Inst. Meth. A **474** (2001) 38.

[16] W. Fischer *et al.*, *RHIC Collider Projections (FY 2012 - FY 2016)* (2011).

[17] M. Adamczky *et al.* (BRHAMS), Nucl. Inst. Meth. A **499** (2003) 437.

[18] F. S. Bieser *et al.*, Nucl. Inst. Meth. A **499** (2003) 766.

[19] Xuan Li (for STAR), BAPS.

[20] W. Fischer, presentation to 2011 BNL Program Advisory Committee.

[21] Y. Fukao *et al.*, Phys. Lett. B **650** (2007) 325.

[22] Y. Wang, *Measurement of inclusive forward neutral pion production at $\sqrt{s}$=200 GeV in polarized proton-proton collisions at RHIC*. PhD dissertation, U. Texas (Austin) (2004); D. Morozov, PhD dissertation, IHEP, Protvino (2006); N. Poljak, PhD dissertation, University of Zagreb (2010); E. Braidot, *Two-particle azimuthal correlations at forward rapidity in STAR*, PhD dissertation, Utrecht University (2011).

[23] L. .C. Bland *et al.* Instr. Exper. Tech. **51** (2008) 342.

[24] L. .V. Nogach *et al.*, contribution to the XIV Workshop on High Energy Spin Physics, Dubna (2011) [arXiv:1112.1812].

[25] G. Aad *et al.* (ATLAS) Phys. Lett. B**705** (2011) 9.

[26] A. Brunner *et al.* Nucl. Instr. Meth. A **414** (1998) 317.

[27] B. B. Back *et al.* Nucl. Instr. Meth. A **499** (2003) 603.